CHAPTER V

Understanding the Response to a Sudden Increase in the Solar Wind Density

Chapter IV explored the mechanisms for the two-phase response when the MI system reacts to a sudden increase in the solar wind density, by means of numerical simulations. This chapter will utilize both insitu measurements and numerical simuations to further understand the two-phase response.

5.1   Introduction

The effects of solar wind pressure enhancements on the dynamics of the Earth's magnetosphere-ionosphere system have been observed for many years, primarily utilizing two observational techniques (ground-based magnetometer observations and SuperDARN observations):

1. Ground-based magnetometer observations indicate a two-phase response after a sudden pressure enhancement (e.g., *Friis-Christensen et al.* (1988), *Farrugia et al.* (1989), *Russell and Ginskey* (1995), *Moretto et al.* (2000), *Sibeck et al.* (2003)). The response is observed over a large range of latitudes. At higher latitudes (polar cap latitudes) on the morning side, the first response shows a negative pulse in the H component of the magnetic perturbation and the second

response indicates a positive deflection. At lower latitudes, the H component shows a positive pulse in the first response and a negative deflection in the second. On the afternoon side, this bipolar change of the magnetic perturbation behaves in the opposite manner.

2. SuperDARN measurements (and other techniques revealing the ionospheric potential) show that a pair of convection vortices appears in the dayside ionosphere after a sudden pressure enhancement encounters the magnetosphere, and a second pair of vortices follows (e.g., *Engebretson et al.* (1999), *Boudouridis et al.* (2008)). The first pair of vortices rotates clockwise on the morning side and counter clockwise on the afternoon side. The second pair behaves in an opposite manner. The plasma convection flows in a direction opposite to the ionospheric Hall current, which is the major contributor to the ground-based magnetic perturbation at high latitudes. The convection has a consistent behavior with the previously mentioned bipolar signature observed in the magnetic perturbations.

Both types of observations (i.e., ground based magnetometer and SuperDARN) indicate that a sudden solar wind pressure increase that impacts on the magnetosphere results in responses that occur in two phases in the ionosphere. These responses have been reproduced by a wide variety of simulation studies (e.g., *Lysak and Lee* (1992), *Slinker et al.* (1999), *Fujita et al.* (2003a), *Fujita et al.* (2003b), *Keller et al.* (2002), *Yu and Ridley* (2009) (Chapter IV).

A significant amount of work has focused on understanding the generation mechanism of the two-phase responses, and many of these studies have found that the dynamics of field-aligned currents (FACs) are responsible for the two-phase responses. FACs flow into and out of the ionosphere, producing convection vortices there. Consequently, among past studies, the main argument is on how FACs are generated after the sudden solar wind pressure increase encounters the magnetosphere and how they subsequently influence the ionospheric response. *Kivelson and Southwood* (1991)

91

proposed a model suggesting that FACs are directly generated by the shear Alfvén perturbations at the low latitude boundary layer (LLBL). *Tamao* (1964a), *Tamao* (1964b) and *Southwood and Kivelson* (1990) suggested that the development of vortical flows in the ionosphere results from the conversion of compressional waves to transverse waves, which carry FACs into the ionosphere. However, these studies did not consider the two responses separately.

In contrast, individual treatment of the two responses were reported by many researchers, such as *Araki* (1994), *Engebretson et al.* (1999), *Moretto et al.* (2000), *Keller et al.* (2002), *Fujita et al.* (2003a), *Fujita et al.* (2003b), *Stauning and Troshichev* (2008), *Yu and Ridley* (2009) (Chapter IV), and *Samsonov et al.* (2010). *Araki* (1994) proposed a physical model in which the first response results from the dusk-to-dawn inductive electric field caused by the compressional fast mode wave, and the second response is a result of enhanced convection electric fields in the new compressed configuration. *Keller et al.* (2002) suggested that the first response is due to the current generated by Alfvén waves that are driven by pressure perturbations near the magnetopause and that the second response is due to shear Alfvén waves. *Fujita et al.* (2003a,b) conducted an MHD simulation with a sudden density increase in the solar wind. The authors concluded that the current system associated with the first response is initially generated at the magnetopause and subsequently is converted to FACs through a mode wave conversion between the compressional fast mode wave and the Alfvén wave. The authors also concluded that the current system, which is responsible for the second response, is driven by a dynamo in the tailward area of the cusp region. *Stauning and Troshichev* (2008) suggested that the first pair of FACs is associated with excessive magnetopause boundary currents, which may be diverted along cusp field lines to close at the ionospheric foot points, while the second pair of FACs is related to temporarily increased Region-1 FACs. A recent study by *Samsonov et al.* (2010) explored the sources in the magnetosphere for the two pairs of

ionospheric currents using a global MHD simulation under northward IMF conditions. They found that the first transient response is connected to energy dynamo from the shock-intensified lobe reconnection, while the second transient response is related to the dynamo near the equatorial plane at the flanks which is associated with the reflected fast shock inside the magnetosphere. Chapter IV (*Yu and Ridley* (2009)) numerically studied the two responses with different interplanetary magnetic field (IMF) orientations. The authors found that the first response is likely caused by the same generation mechanism under both northward and southward IMF conditions. The sudden compression of the magnetosphere results in fast mode wave propagation through the dayside magnetosphere, inducing a dusk-to-dawn electric field. Subsequently, the dusk-to-dawn inductive currents turn into FACs at high latitude near the dayside cusp region. The FACs flow into the ionosphere on the afternoon side and out of the ionosphere on the morning side. With regard to the second response, they proposed that FACs are generated differently under different IMF conditions: In a northward IMF situation, FACs are generated from magnetospheric vortices that are caused by thermal pressure gradients inside the magnetosphere after the high solar wind pressure impacts on the magnetosphere. Whereas in the southward IMF case, no thermal pressure gradient is observed inside the magnetosphere; however plasma shear flow in the dayside magnetopause rebuilds up convection vortices and thus FACs.

In order to have a clear reference to the first and second responses, they will be referred to as "Ey-response" and "Vortex-response" respectively in the rest of this chapter, following the work in Chapter IV. These names are directly related to their generation mechanisms and hence self-described.

With a large number of simulations and observation reports available on the responses of the geospace system to a discontinuity in the solar wind density, few studies have investigated the two individual responses statistically. In this chapter, density

increase events from 1996-2002 are studied. The selection of the events follows the criterion: $\frac{dN}{N} > 2$ within 3 minutes, where dN is the change of solar wind number density (N) across the discontinuity. The responses observed from the AMIE (Assimilative Modeling of Ionospheric Electrodynamics, *Richmond and Kamide* (1988)) technique, geosynchronous satellites, and ground-based magnetometers are examined. It is found that not all the events respond in the "typical" two-phase manner to the sudden density increase. To further understand the categories sorted out from the observations, statistical analysis on various external solar wind characteristics as well as simulations are conducted. Section 5.2 describes the observational study of the sudden pressure enhancement and the corresponding phenomena observed by various measurement methods; Section 5.3 presents simulation results, investigating the influence of the solar wind Alfvén Mach number on the responses and its implications; and Section 5.4 focuses on the wave propagation after the sudden compression of the magnetosphere and its influence on the ionospheric responses.

5.2   Observations

As shown by the simulation in Chapter IV, it is possible to use the cross polar cap potential (CPCP) index as a reference in determining whether two-phase responses are observed after a sudden pressure enhancement encounters the magnetosphere. AMIE provides 1-minute resolution data, from which the CPCP index can easily be obtained (*Ridley and Kihn* (2004)). However, as the CPCP index obtained from AMIE is the difference between the maximum and minimum electric potentials in the ionosphere, the development of the CPCP might not thoroughly reflect the ionospheric vortices that appear locally. Therefore, other selection criteria such as ground-based magnetic perturbations from dayside magnetometer stations, potential patterns driven by AMIE over the global region, and polar cap north (PCN) index measured by one northern hemisphere high-latitude magnetometer are used to fur-

ther identify the occurrence of the two-phase responses. As mentioned earlier, for a typical two-phase response, the ground-based observation of perturbations should show bipolar variations, and the AMIE potential patterns should display two pairs of potential cells (convection vortices). Furthermore, the PC index should first indicate a negative pulse for the Ey-response and then a positive increase for the Vortex-response (*Lukianova* (2003)). These criteria help to categorize the interested events into two groups as discussed below.

When very little response to an event is observed within the database, that event is excluded. Such events are actually not very many. The lack of response could be due to the solar wind feature missing the magnetosphere, or some other reason; it is outside the scope of this research study. For all events in which a clear response was observed, we classify the density increase events into two basic groups. Those events with responses in two phases are categorized into "two-phase response," (i.e., the responses throughout the geospace system are represented by bipolar ground-based magnetic field perturbations, two successive pairs of potential cells in opposite polarities, and bipolar pulses in the PCN index), while those with a single phase response (either acting as the Vortex-response or the other) are classified into "single-phase response" (i.e., the responses do not show bipolar but unipolar variations). Figures 5.1-5.6 illustrate two examples that demonstrate the "two-phase" group (Figures 5.1-5.3) and the "single-phase" group (Figures 5.4-5.6).

5.2.1 Two observational examples

The first example in Figures 5.1-5.3, shows responses observed from the ionosphere and the ground. At 14:01 UT on Jan 04, 2001 (denoted by the dashed line), the OMNI data (Figure 5.1) indicates a sudden solar wind density increase encountering the magnetopause under northward IMF condition. After that, the PC index (the fifth line plot) shows a negative pulse before the index increases significantly, and the

CPCP index (the last line plot) obtained from AMIE depicts two successive peaks within 10 minutes. The magnetometer observations (panel a in Figure 5.2), which are obtained from ground magnetometer stations located above 50° magnetic latitude on the morning side, display bipolar perturbations. Potential patterns (Figure 5.3) from AMIE also show two responses: the first pair of potential cells appears at 14:02 UT around 70° magnetic latitude on the dayside ionosphere, and the second pair with opposite polarity appears after about 2 minutes.
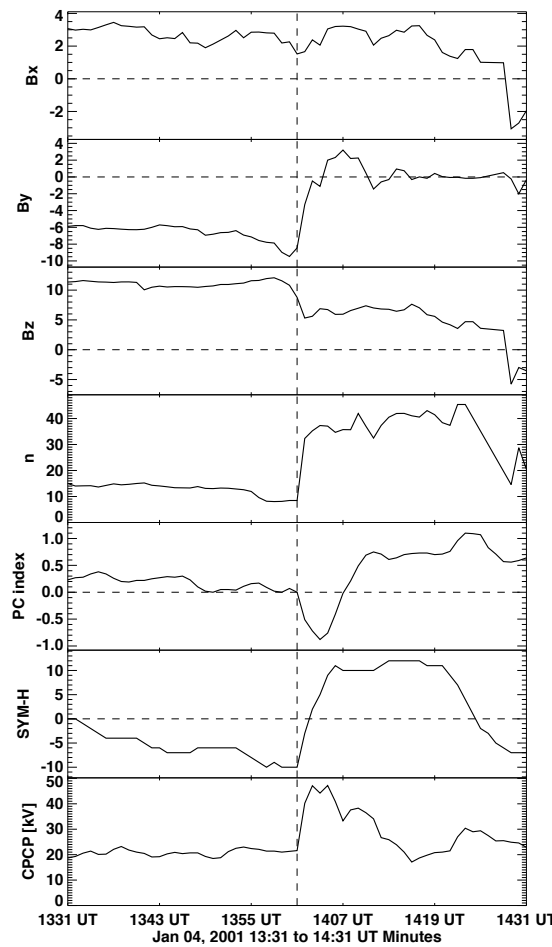

Figure 5.1: One example from the "two-phase" group of the responses observed from the ground, the ionosphere and the magnetosphere due to the sudden solar wind density increase at Jan 04, 2001. The figure lists the solar wind B_x, B_y, B_z and solar wind density, PC index from ground observations, SYM-H index, and the cross polar cap potential from AMIE. The dashed line indicates the time the solar wind density increases.

96
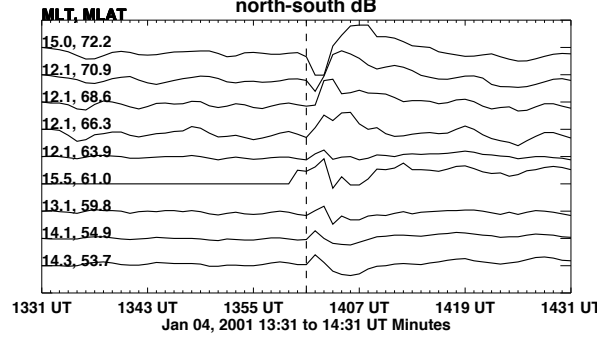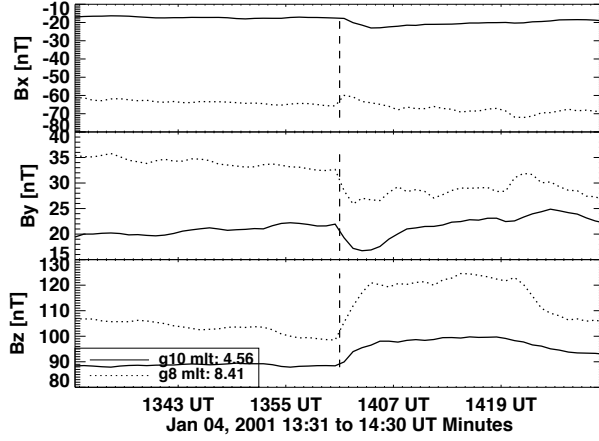
(a) Ground-based data

(b) GOES data

Figure 5.2: Panel (a) shows ground-based observation about magnetic perturbations in the morning side above 50° of magnetic latitude, and the lines are in a order according to the latitudes. The first column of the numbers indicate the magnetic local time, and the second column indicates the magnetic latitude of each station. Panel b shows the magnetospheric disturbance observed from the GOES satellite.

In addition to above ionospheric and ground responses, the magnetospheric responses are also examined. The magnetic fields observed by GOES 8 and 10 (panel b in Figure 5.2) on the dawn side show that the Bz component clearly increases after a sudden compression of the magnetosphere. In conclusion, all the above observations indicate that the sudden solar wind density increase impacting on the magnetosphere causes a wide range of perturbations throughout the geospace system.

However, some events that evolve with sudden solar wind density enhancements do not show definitive two-phase responses. One such "single-phase" example is shown in Figures 5.4-5.6, which utilizes the same database as in Figures 5.1-5.3.

97
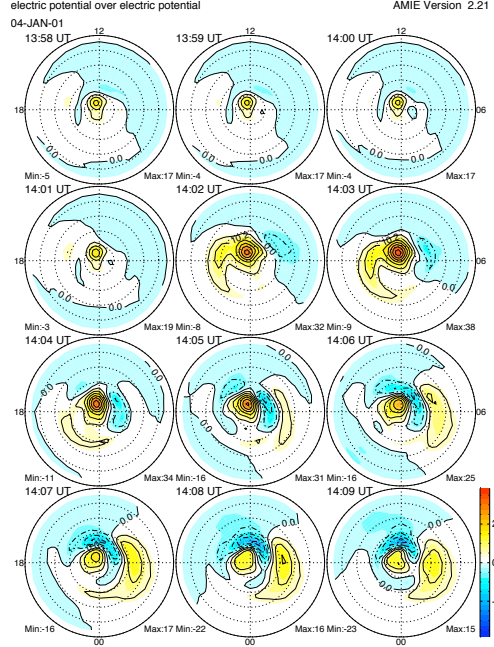
Figure 5.3: The ionospheric response in the AMIE electric potential pattern. Yellow indicates positive potential and blue means negative potential.

From the OMNI 1-minute data, an increase of solar wind is observed at 16:46 UT on May 11, 2002 when the IMF Bz was southward. However, the ground-based perturbations in the post-noon sector do not display clear two-phase responses from high latitudes to low latitudes, and AMIE output of the residual potential pattern do not show two successive pairs of potential cells emerging from the dayside ionosphere, although a disturbance in the geosynchronous orbit is observed. The disturbance in the ionosphere appears to be more like the second phase (or Vortex-response) of the typical two-phase responses, but the first phase (or Ey-response) is not observed in this event. As the D_{st} index indicates a highly disturbed system, and substorm activity (by checking AL index) indeed occurred preceded this example event, the nightside in the ionospheric potential pattern shows significant disturbances.
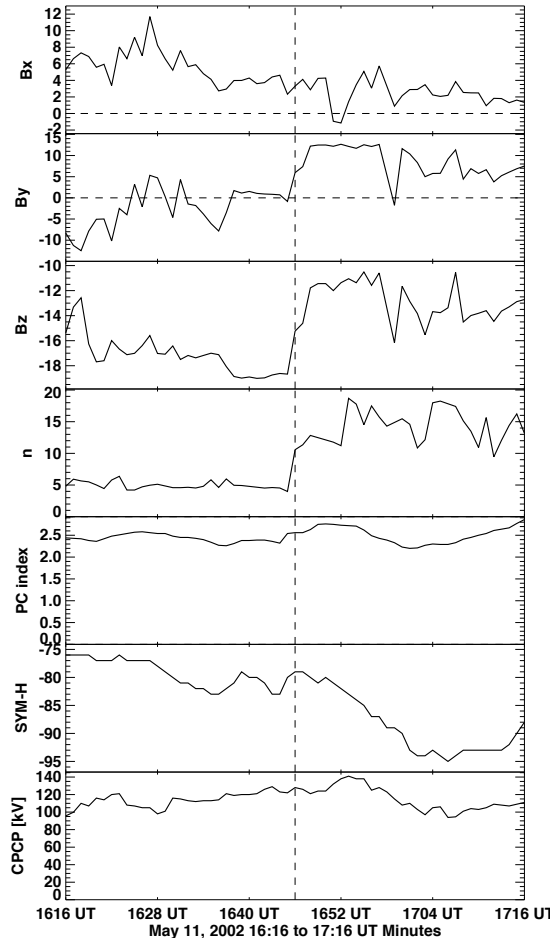
Figure 5.4: One example from "single-phase" group of disturbances observed from the ground, the ionosphere and the magnetosphere due to the sudden solar wind density increase at 16:46 May 11, 2002. The figure is in the same format as Figure 5.1.

5.2.2 Statistical view

The CPCP index obtained from simulation results in Chapter IV shows different behavior for different IMF orientations. Under northward IMF conditions, there are two peaks in the CPCP profile. While under the southward IMF conditions, the index decreases first before increasing to a peak. To find the same phenomena from the observational point of view, OMNI data and AMIE data are utilized. Twenty-three events of a solar wind density increase, mostly with continuously northward IMF for at least 30 minutes, and forty-one events, mostly with continuously southward
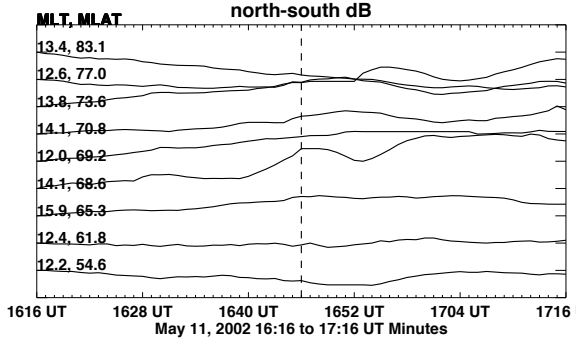
(a) Ground-based data
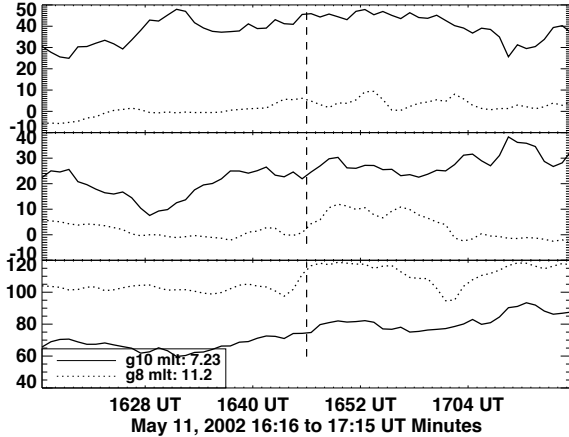
(b) GOES data

Figure 5.5: Panel (a) shows the ground-based magnetic perturbations in the post-noon side, and Panel (b) shows magnetic field data from GOES.

IMF for at least 30 minutes, are found and selected to make epoch plots, which are shown in Figure 5.7. The epoch time $t = 0$ is the time when the ionosphere starts to react to the sudden increase of the solar wind density. Two peaks are observed in the AMIE CPCP profile after the epoch time in the northward case; while in the southward situation, the CPCP slightly decreases and is followed by an increase. These behaviors are consistent with the simulation results in Chapter IV (*Yu and Ridley* (2009)), although they are more subtle in the epoch plots. The subtleness in the plots could be a result of slight different response times in different events and
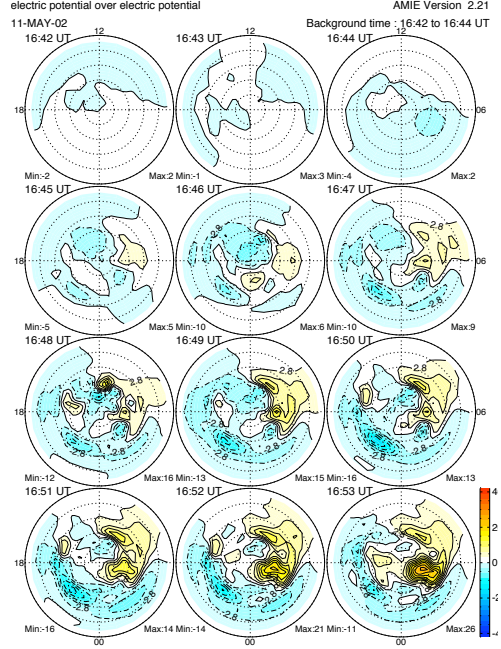
Figure 5.6: The residual electric potential obtained by subtracting the base potential pattern, an average of potential patterns from 16:42 to 16:44, from the other patterns.

the fact that the time-scale of the features are a few minutes, while the temporal resolution of the AMIE CPCP is one minute. This means that there are only a few measurements across each event, so it is easy to miss the main maxima and minima. Further, the AMIE technique utilizes a non-uniform distribution of data, such that, for each event, the magnetometers may not be in the optimum positions to measure the global distribution, and therefore the CPCP may have errors. Nevertheless, the features are subtle, but visible.

While these events show typical two-phase responses ("two-phase" group), there are events that only show a single phase ("single-phase" group), as previously illustrated from the second example in Figures 5.4-5.6. One attempt to explain the difference was first described by *Lukianova* (2003), who studied the first response by using the PCN index and suggested that during magnetic storms, the events tend not to have the first response.
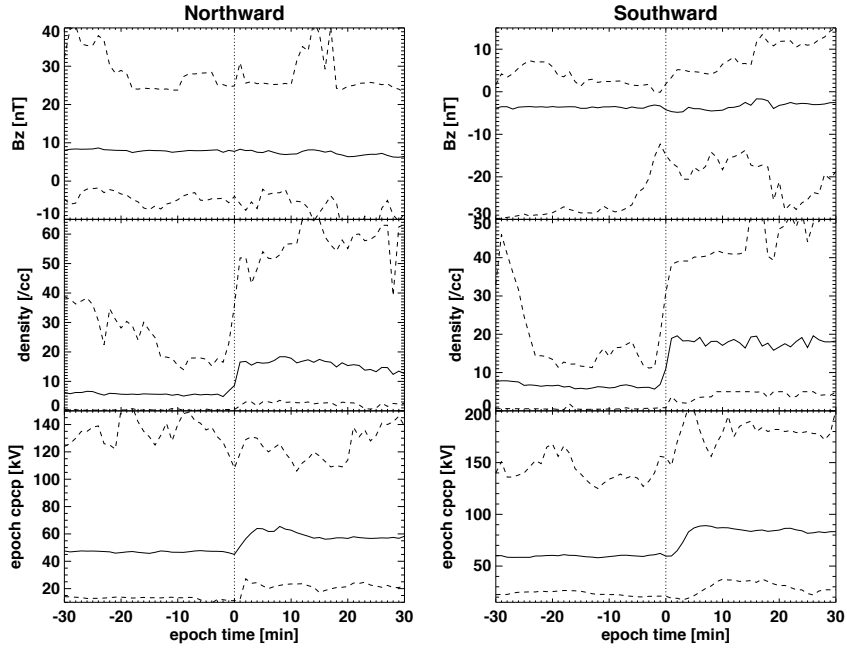
Figure 5.7: Superposed epoch plots of "two-phase" group for northward (left) and southward (right) IMF cases. The two dashed lines in each panel represent the upper and lower quartiles, and the dashed vertical line indicates the zero epoch time.

This study, however, could not strongly support or negate the conclusion from *Lukianova* (2003). Attempts by using D_{st} index to understand the two-phase response have also been carried out here. Figure 5.8 (panel a, top) shows a histogram of the "two-phase" group with respect to D_{st}. Note that most of the events concentrate around small values of the D_{st} index, but during storm times, some events with a large D_{st} index can also have two responses. Furthermore, a histogram for the "single-phase" group in the lower plot of panel (a) shows that the D_{st} index for the "single-phase" group is not limited to the large values (or storm time), but there are many fewer events in this category and the distribution of these events is very sporadic. Therefore, we can not conclude that with a higher storm activity level the events tend to have single-phase responses, as suggested by *Lukianova* (2003). However, the possibility of the above relationship remains, as will be discussed in below.

Several other attempts are described in order to determine the controlling factor(s)
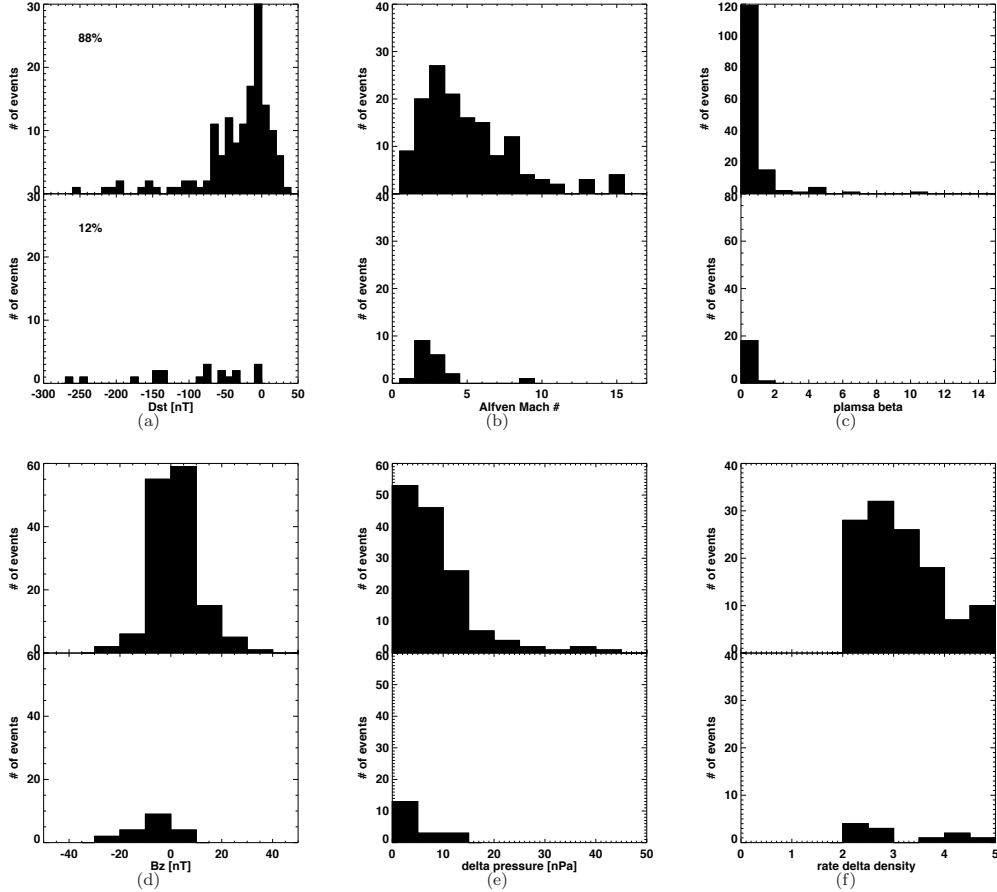
Figure 5.8: Histogram of events that show two-phase responses and single-phase response to the sudden solar wind density increase as a function of different factors: (a) Dst index, (b) Mach number, (c) solar wind β, (d) IMF B_z, (e) net dynamic pressure change and (f) change rate solar wind number density. In each panel, the upper figure refers to "two-phase" group, while the lower figure refers to "single-phase" group. The percentage numbers shown in (a) are the percentage of total number of the events for both groups.

that make(s) a difference in the way geospace responds to a sudden solar wind density increase. In other words, which factor(s) control(s) whether or not geospace reacts with two-phase responses? The factors that are examined include (1) the net increase of dynamic pressure, (2) the solar wind Alfvén Mach number, (3) the plasma β for protons in the solar wind, (4) the rate of solar wind density increase, and (5) the orientation of the IMF. These parameters, representing the external solar wind driving, are chosen from the time just before the high-density discontinuity in the solar wind encounters the bow shock. Figure 5.8 (panel (b) to panel (f)) shows histograms of the two groups corresponding to these parameters. It is found that there is no clear separation between the two categories in these parameters. In other words, a pattern such that the two categories prefer to occur in two different ranges of any of the parameters is not observed here, implying that none of these parameters seem to distinctively control the manner the system responds. It is possible that a combination of some of the above external solar wind characteristics controls the way the geospace responds. It is also possible that the geospace system itself, rather than the external drivers, determines the nature of the responses. But, these possibilities still require further investigation.

However, some possible tendencies still exist. For example, for the Bz orientation (Figure 5.8 (d)), a larger portion of the second category prefer to occur under a southward IMF condition; For the Alfvén Mach number (Figure 5.8 (b)), the second category events mostly concentrate on the range of a small Alfvén Mach number; such trend is also observed in (Figure 5.8 (e)). Nevertheless, many events from the first category also occur in these ranges, leading to a dilemma that no definitive conclusion could be drawn. One could conclude that with a southward IMF or a more disturbed time period the system is more likely to have a single-phase response, only if there were many fewer two-phase events than one-phase events in the same IMF or Dst range. Apparently, this is not the case here.

One possible explanation for this uncertainty is that the identification of the two-phase response becomes difficult when the system is highly disturbed. As Chapter IV have shown that under both southward and northward IMF conditions, the net changes caused by the increase in the solar wind density are the same, but the background electric potential/FACs in the southward IMF case needs to be subtracted in order to identify the net changes due to its opposite polarity to the background electric potential/FACs. The situation may be the same in these observations. Because of the significant background, the changes caused by the solar wind variation can be partly submerged, leading to an integrated responses that are not clear enough to be distinguished, even though the two-phase response is indeed generated.

One of the difficulties with utilizing observational data is that there are often too few events to have the statistics needed in order to adequately explore the various combinations of drivers that may cause one type of reaction or another. Note that the number of events is highly dependent on the criteria used in the selection. *Zhang et al.* (2010) utilized a criteria of $\frac{dN}{N} > 0.5$ to select the pressure increase events, instead of using $\frac{dN}{N} > 2$ as in this study, therefore a lot more events were presented in their work. The reason for using a larger increase in the solar wind density in this study is that we intend to observe clear and strong response in the MI system more easily. Furthermore, the study here needs to sort out the events that clearly show two-phase responses, which further reduces the number of events for the statistical study. We therefore turn to simulations, in an attempt to determine the role of the solar wind Alfvén Mach number in the geospace system response. The Mach number is chosen because in the histograms (Figure 5.8, panel b) of the two categories, the events in the second category tend to cluster around the low Mach numbers. The simulation results lead us to believe that the Mach number does indeed play a significant role in the manifestation of the two responses. The results also imply that the typical two-phase responses always exist, regardless of the magnitude of the Mach number;

however, in low Mach number situations, the typical two-phase response, in the form of the CPCP index or the ground magnetic perturbations, are not so distinct as that in high Mach number situations, which is the reason that led us to classify these events into the "single-phase" group.

5.3 Simulations with different Alfvén Mach numbers

While many parameters could possibly control the response properties in the geospace system, as described above, only one parameter, the solar wind Alfvén Mach number, has been investigated here so far since the Mach number histogram indicates a direct possibility: a low Mach number may influence the responses to a sudden solar wind density increase. Examination of the effect of other parameters on the system will be conducted in the future. The global MHD model Block-Adaptive Tree Solar-wind Roe Upwind Scheme (BATS-R-US) coupled with an ionospheric electrodynamics model is used for this investigation (Chapter II). The inner boundary is designed to have fixed density of 28 cm^{-3}, floating pressure, and reflective velocity (i.e., no flow through the boundary). Simulations are driven by upstream solar wind with different Mach numbers, which vary by changing the IMF B_z component, while keeping the density the same. Other simulations with Mach numbers that are varied through changing the solar wind density, as opposed to the IMF B_z, will also be performed and described later. Since the CPCP index and the ground magnetic perturbations are generally utilized to determine whether or not the system undergoes a two-phase response, the following section will study the influence of the Mach number by primarily focusing on these two parameters. Also, as the two-phase response is phenomenologically similar under both southward and northward IMF conditions as found in Chapter IV (*Yu and Ridley* (2009)) (i.e., after the sudden increase in the solar wind density, the net changes in the ionospheric potential/FAC pattern are the same), the following simulations only consider the northward IMF cases.

5.3.1 Effect of the Mach number (I) (different IMF B_z)

Eleven simulations with different Alfvén Mach numbers have been carried out. The solar wind and IMF conditions are initially modeled with constant IMF $B_x = B_y = 0$, n = 5 cm^{-3}, $V_x = 400$ km/s and T = 100,000 K, but with different values of northward B_z varying from 30 to 2.875 nT in these eleven simulations. Therefore, the Alfvén Mach number varies from 1.3 to 14. The Earth's magnetic dipole axis is forced to be aligned with the rotation axis, so that the simulations are symmetric across the equatorial plane. The simulation start time is arbitrarily chosen at 16:45 UT, March 2010. A contact discontinuity is then introduced at the upstream boundary at 17:15 UT, where the density and temperature abruptly change from 5 cm^{-3} to 20 cm^{-3} and from 100,000K to 25,000K respectively, in order to conserve the thermal pressure for the contact discontinuity. The other parameters remain unchanged. Furthermore, the axis of the magnetic dipole is aligned with the rotation axis and the Z axis. Therefore, the simulations are idealized.

The influence of the Mach number on the geospace system can be observed through the ionospheric cross polar cap potentials (CPCP). The CPCP in the simulation is the difference between the maximum and minimum of the electric potential over the ionospheric northern hemisphere. The CPCP for 11 different Alfvén Mach numbers are illustrated in Figure 5.9. Initially, the CPCP is steady before the high solar wind pressure encounters the bow shock. The varying levels of the CPCP for the different runs are due to the fact that the IMF is becoming stronger as the Mach number is decreasing. This serves to increase the CPCP (e.g., *Weimer* (1996)). After the sudden compression of the magnetosphere, the CPCP index with lower Mach numbers starts to increase earlier and shows three subtle peaks throughout the simulation time, while the CPCP index with higher Mach numbers displays a two-peak behavior, which is consistent with the typical two-phase responses in the ionosphere from early studies.

In the low Mach number simulations, the early response in the ionospheric CPCP
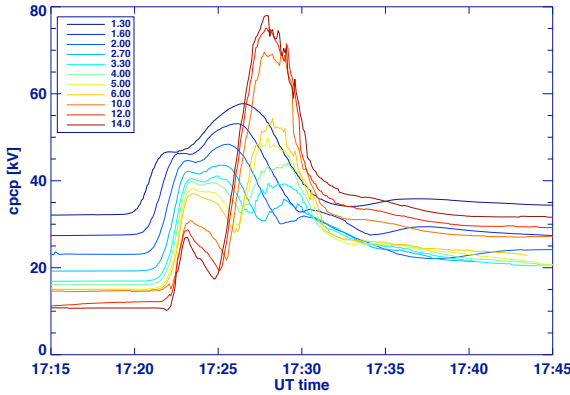
Figure 5.9: From idealized simulations, the cross polar cap potential reacts to the same solar wind density change from $N = 5cm^{-3}$ to $N = 20cm^{-3}$ with different solar wind Alfvén Mach number.

can be interpreted as follows: A lower Mach number in the solar wind corresponds to a thicker magnetosheath, so the high-density discontinuity from the upstream boundary at 32 R_e encounters the bow shock earlier. Once the bow shock is compressed suddenly, a fast mode wave is triggered insde the magnetosheath ahead of the transmitted discontinuity and carries disturbances towards the magnetopause. The disturbances propagate inside the magnetosheath at a speed equal to the sum of the magnetosheath plasma speed ($\approx 100 - 200km/s$) and the fast mode wave speed ($\approx 300 - 400km/s$). However, in the high Mach number cases, the high-density discontinuity, still in the solar wind, has not yet encountered the bow shock and is propagating approximately at a solar wind speed, which is smaller than the above combined speed in the low Mach cases. For example, for a low Mach number of 2, the disturbances propagate inside the magnetosheath at about 500 km/s because (a) the magnetosheath flow speed is not reduced significantly due to the weakness of the shock, and (b) the fast mode wave speed is large within the magnetosheath due to large magnetic fields. The discontinuity in a high Mach number of 12, however is still propagating in the undisturbed solar wind with a speed of 400 km/s in the solar wind. Therefore, the magnetopause is disturbed earlier in the low Mach number simulations, producing

earlier disturbances in the ionosphere, as observed in the CPCP index. Meanwhile, it should be noted that, for a given event, the transmitted disturbance inside the magnetosheath may propagate at a speed smaller than that when it was in the solar wind (e.g., *Zhang et al.* (2009); *Koval et al.* (2006); *Pallocchia et al.* (2010)). As contrasted with these references that studied the speed history in one given event, the discussion above is comparing different speeds between a low Mach number case and a high Mach number case.

Also in the low Mach number simulations, the three peaks in the CPCP profile seem controversial, as a two-peak profile is typical and consistent with the two-phase responses. However, careful inspection of the ionospheric response indicates that the second peak in the CPCP profile is not from the Vortex-response (i.e. the second phase response); rather, it is still associated with the Ey-response (i.e. the first phase response). In other words, only the third peak is really caused by the Vortex-response. Take the simulation with Mach number 2.0 for example. After 17:28 UT, the Vortex-response takes over the entire ionospheric electrodynamics, but before this time, the electrodynamics in the ionosphere looks quite complicated. Figure 5.10 shows the residual field-aligned currents (FACs) and electric potentials. The first pair of FACs associated with the "Ey-response" (positive J around 9 MLT and negative J around 15 MLT) appears at 17:21:00 UT, and the second pair of FACs associated with the "Vortex-response" (positive J around 15 MLT and negative J around 9 MLT) emerges at 17:22:00 UT, while the first pair, together with the NBZ current system is still growing. Subsequently, the positive electric potential cell on the duskside decreases a little bit (17:23:00-17:24:00) due to the appearance of the second pair of FACs (or the appearance of the Vortex-response) and increases again due to the continuous growth of the first FAC pair (or the growth of the Ey-response), but the negative potential cell on the dawnside seems to continue increasing throughout the interval. The overall effect of these two different potential variations is that a subtle trough

in the CPCP profile is produced, resulting in two peaks during the "Ey-response" period.

Since the CPCP index in these simulations is calculated as the difference between the maximum and minimum electric potential throughout the hemisphere, the decoupling of the CPCP profile could illustrate the above phenomena better. Figure 5.11 (top) shows the extrema (maximum and absolute value of the minimum) of the electric potential over the hemisphere. Similar to what is seen from the FAC and potential plots in Figure 5.10, during the early stage (17:21 - 17:28 UT, before the Vortex-response dominates the ionospheric electrodynamics), the positive potential profile, representing the potential in the dusk cell, has two peaks, while the negative potential profile, representing the potential in the dawn cell in this stage, keeps growing until the Ey-response starts to fade. The reason for the double-peak in the positive potential is because the Ey-response is still in the growth mode, while the appearance of the Vortex-response, which has an opposite polarity and is initially much weaker than the Ey-response, can not overwhelm the Ey-response, but only reduce its magnitude. Therefore, the two-peak profile is a result of the competition between the Ey-response and the initial Vortex-response. The increase of the negative potential without a secondary maxima indicates that the appearance of the Vortex-response on the dawn side does not influence the Ey-response as significantly as on the dusk side. Besides the different temporal evolution in the early stage of the dusk and dawn potential extremes, the reaction starting times from the two extremes also differs. The dusk (positive maximum) potential responds earlier than the dawn (negative minimum) potential.

Given the idealized setup of the solar wind driving and the coordinates, these differences (in reaction time and potential variation) between the positive and negative potentials likely result from the conductance asymmetry between the dusk and dawn sides. To confirm this speculation, we repeated the simulation with Mach number

110

(a) Residual Jr   (b) Potential
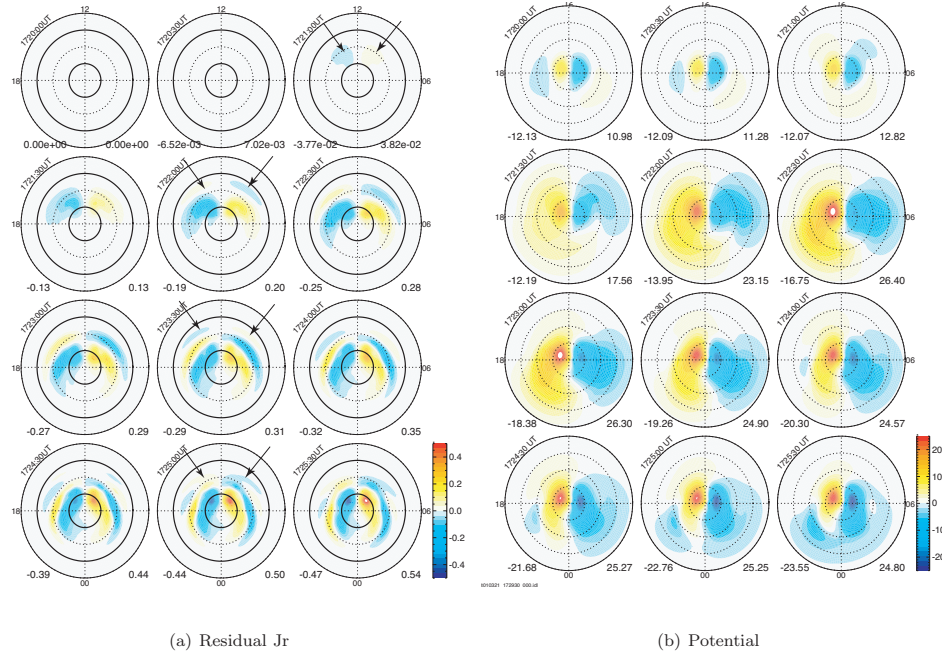
Figure 5.10: The left panel (12 cirlces) shows the residual field-aligned current on the northern ionosphere after the sudden solar wind density enhancement encounters the bow shock. The base FAC pattern that is used to be subtracted from is at 17:20 UT. The time is labeled on the upper left of each circle. The time cadence is 30 seconds. The right panel (12 circles) shows the potential pattern at the same time sequences. The black arrows mark the newly emerging pairs of FACs. The two ionospheric patterns are from the simulation with the Alfvén Mach number equal to 2.
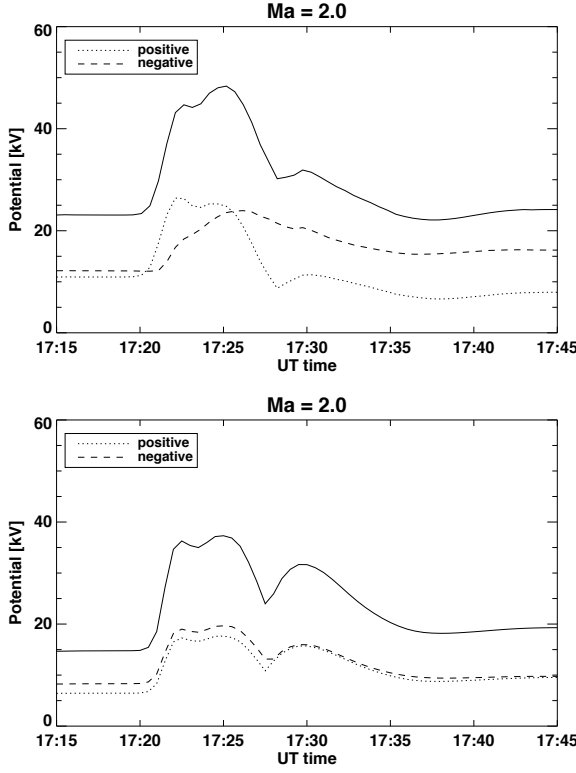
Figure 5.11: The CPCP index (solid), the maximum positive potential (dotted), and the absolute value of the minimum negative potential (dashed) in two simulations. The top simulation uses relatively realistic conductance, including the auroral oval and daylight; the bottom one usese uniform conductance, with the Hall and Pedersen conductance being 0 and 5 mho respectively.

2.0 with a uniform conductance applied in the ionosphere, instead of a more realistic conductance pattern that considers both the auroral oval and daylight. The Hall and Pedersen conductances here are replaced by constants 0 and 5 *mho*, respectively. The resultant CPCP index from this simulation is shown in Figure 5.11 (bottom), indicating that both negative and positive potential extrema react in the same manner to the sudden increase in the solar wind density: both respond at the same time and possess 3 peaks, with the subtle trough between the first two peaks resulting from the competition between the Ey-response and the Vortex-response, as discussed above. Such symmetric reactions in the positive/negative extreme potentials develop because of the uniform ionospheric conductivity. Therefore, the distribution of the

112

ionospheric conductivity is believed to play an important role in determining the asymmetry between the positive (dusk) or negative (dawn) potential after a sudden increase in the solar wind density arrives at the magnetosphere.

Returning to Figure 5.9, in these low Mach number cases, the first two peaks are associated with the Ey-response that lasts longer than in the high Mach number cases, providing early reaction time of the Ey-response and its late overtaking by the Vortex-response (after 17:26 UT in the high Mach number cases, and as late as 17:30 UT in the Mach number of 2.0 case). The third peak indicates the maximum strength of the Vortex-response, which is much weaker compared to those with high Mach numbers. This weaker Vortex-response in the low Mach number conditions is possibly due to the lack of energy input to the ionosphere. *Kivelson and Ridley* (2008) suggested that with a low Mach number and strong solar wind driving (high magnetic field), the efficiency of wave reflection in the ionosphere increases, leading to a reduced energy input into the geospace system. This suggestion was used to explain the saturation of the ionospheric CPCP and is more applicable for the relatively steady state, but not for the transient response as studied in this chapter. Considering the response is associated with the FAC flowing into/out of the ionosphere, the strength of the response has to be relevant to the dynamo ($\mathbf{J}\cdot\mathbf{E} < 0$) in the equatorial magnetosphere at this stage, which supplies the electromagnetic energy to the ionosphere via FACs. The dynamo is driven by the plasma flow from the pressure gradient (*Motoba et al.* (2007)) and is found to be significantly smaller than those with high Mach numbers (not shown). The smaller dynamo, or the smaller pressure gradient after the sudden compression of the magnetosphere, implies that with a lower solar wind Alfvén Mach number, the energy through the magnetopause is reduced more significantly.

Besides the above phenomena observed in the ionosphere, mainly from the CPCP index, the temporal variation of the ground magnetic perturbations also shows a strong dependence on the Alfvén Mach number. Figure 5.12 shows the northward

113

magnetic perturbations at 15 MLT for Mach = 2.0 (top) and Mach = 14 (bottom) at various magnetic latitudes. The perturbations are computed by Biot-Savart integral from Hall currents above 50° in the ionosphere. As the interesting disturbances appear at high latitudes, the Hall current alone is sufficient to represent the ground-based perturbations (*Yu et al.* (2010)). The bipolar disturbances in both the Ey-response (i.e., positive disturbance at higher latitudes and negative at lower latitudes) and Vortex-response (i.e., negative disturbance in higher latitudes and positive in lower latitudes) are clearly predicted in the high Mach number cases. But those with the low Mach number evolve in a similar complicated form as seen in the CPCP: the Ey-response experiences two successive disturbances (most clear at 70° and 75°), but the Vortex-response can be barely distinguished due to its weak strength.
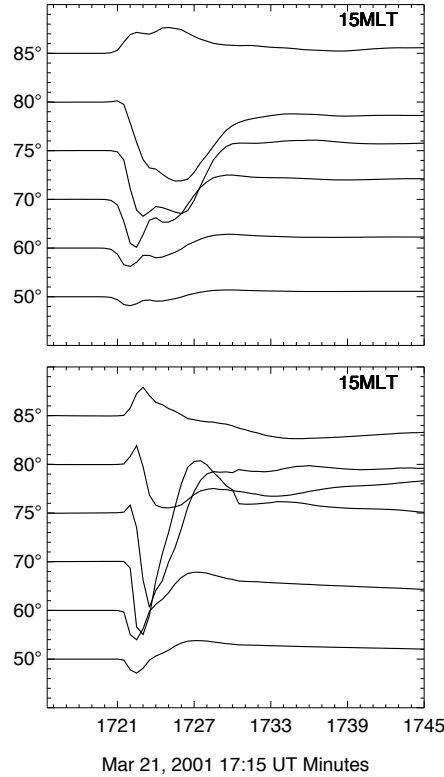

Figure 5.12: The northward magnetic perturbations at various latitudes along the 15 MLT longitude from two simulations: Alfvén Mach number = 2.0 (top) and Alfvén Mach number = 14.0 (bottom).

5.3.2 Effect of the Mach number (II) (different densities)

In order to test the effect of the initial solar wind density on the magnetospheric response, the simulation suite was repeated but the conditions were altered. Instead of varying the IMF Bz component to obtain the different Alfvén Mach numbers, the solar wind density was changed while keeping the IMF $B_z = 5$ nT. The initial solar wind density differs from one simulation to another (varying from 0.16 to 10 cm^{-3}, which corresponds to Mach numbers from 1.5 to 11.2), but the sudden density discontinuity is introduced in the same way in all the simulations: the density is increased by a factor of four. The CPCP index from these simulations is shown in Figure 5.13. The CPCP index with a lower Mach number again displays a three-peak form, but is significantly flatter than earlier simulations; while with a higher Mach number, the typical two-phase response is again clear. This is consistent with the previous Mach number simulations and demonstrates that the solar wind Alfvén Mach number, either as a function of the density or IMF B_z, plays an important role in determining the temporal response in the system.
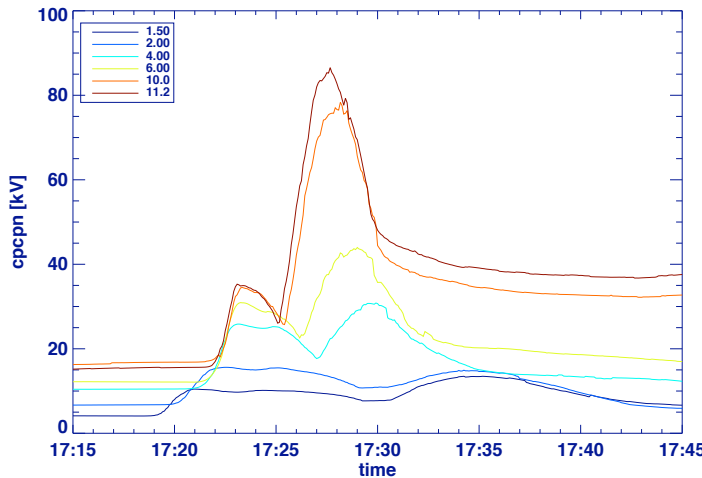

Figure 5.13: The CPCP from simulations with the same IMF Bz but different solar wind densities. The sudden density discontinuity for these simulation undergoes the same jump ratio: by a factor of 4.

Note that the Ey-response shown here is smaller for lower Mach numbers, which is

contrary to what is shown in Figure 5.9 that the Ey-response in lower Mach number cases actually exceeds those in higher Mach number cases (i.e., the net increase of the Ey-response from the initial CPCP state is larger in lower number cases). This can be interpreted as follows. According to the earlier study by Chapter IV (*Yu and Ridley* (2009)), the Ey-response in the ionosphere is related to FACs that are converted from the dusk-to-dawn inductive currents near the high-latitude magnetopause and are connected with the magnetopause currents, so the electric field near and at the magnetopause is an essential factor for the intensity of Ey-response. In Figure 5.9, larger Ey-response for lower Mach numbers is due to the larger B_z in the solar wind and magnetosheath, which leads to larger electric fields near the magnetopause. In Figure 5.13, electric fields in the solar wind are the same due to the same IMF and solar wind velocity, but dissipation inside a thicker magnetosheath for a lower Mach number results in weaker electric fields at the magnetopause, thereby a less intense Ey-response in the ionosphere.

5.3.3 Discussion

As shown in the observation section, the responses of the ionosphere-magnetosphere system to a sudden solar wind density increase can be categorized into two groups: "two-phase" and "single-phase". Within the "two-phase" response, the two phases are the Ey-response and Vortex-response. The "single-phase" group refer to the events that only show a single response, either with the Ey-response missing or the Vortex-response missing. The statistical search for the causes of these two different classes was not conclusive due to the lack of statistics in the "single-phase" category. Additionally, the "two-phase" category does not indicate an explicit preference in any of the tested external solar wind parameters or the internal parameter D_{st}.

After performing simulations with various solar wind Alfvén Mach numbers in an

MHD model and inspecting the responses in the ionosphere (e.g., FAC and potential), we have been convinced that the two responses (Ey-response and Vortex-response) always appear after a sudden solar wind density increase. It is found that the characteristics of the responses, including the duration, the strength, and especially the temporal variation of the response, highly depend on the Alfvén Mach number. But it is the differences in the response between the lower Mach number cases and the higher ones that make the recognizability of the typical two-phase responses difficult in the data. Indeed, in the low Mach number cases, the energy penetration into the system is significantly weakened, causing the lack of signal in the geosynchronous measurement (such as the GOES observations). Furthermore, the weak Vortex-response and the long Ey-response as seen in the CPCP may also lead researchers to interpret that those events do not have the typical two-phase response. Indeed, as shown in the histogram for the Alfvén Mach number (Figure 5.8), almost all of the events (except one) selected for the "single-phase" category involve relatively low Mach numbers. But as explored in the simulations after investigating the essential cause – the FACs, the two-phase response does exist; it is simply very weak and subtle. Hence, we propose that the two categories mentioned above actually belong to the same category. In other words, the second category ("single-phase") is the continuum of the first category ("two-phase").

5.4 Wave propagation

Of the eleven simulations with varying IMF B_z, the one with a nominal Alfvén Mach number of 8 is chosen to examine the propagation of the compressional wave signal. In this case, the IMF B_z is constant at 5 nT. After the abrupt increase of density in the solar wind is introduced into the simulation domain at 32 R_e, it subsequently encounters the bow shock and magnetopause, launching a compressional wave due to the sudden compression of the magnetosphere. The propagation of this

wave signal can be traced by examining the temporal variation of the magnetic field inside and just outside of the magnetosphere after the sudden compression. Figure 5.14 (upper left) shows the contour of dB_z/dt from 3 R_e to 15 R_e on the Sun-Earth line. Yellow means an increase of Bz, and blue means a decrease of B_z. The roughly horizontal orange line over-plotted on the contour is the position of the magnetopause, obtained by selecting the peak of the magnetopause current. The curves between the magnetopause and 3 R_e sketch the front of a compressional fast mode wave. Seen from this figure, an increased B_z (i.e., positive dB_z/dt) appears near the magnetopause at 17:20:00 UT and propagates towards the Earth at a fast mode wave speed, as the disturbance contour aligns with the curve of fast mode wave. When the fast mode wave reaches close to the inner boundary of the simulation domain (3 R_e), the wave is reflected back toward the magnetopause, where the wave is bounced back again toward the Earth at 17:23:00 UT. In other words, the compressional wave signal carried by the disturbance of Bz is reflected repetitively between the dayside magnetopause boundary and the inner boundary. Such bounces within the dayside magnetosphere cavity continues until the energy is dissipated. A similar behavior was reported in *Samsonov et al.* (2007) who also utilized a 3D global MHD model and demonstrated the wave propagations inside the magnetosheath as well as inside the magnetosphere.

In addition to the bouncing feature of the compressional wave signal propagation, another interesting phenomenon observed from the magnetopause profile is that the location of the magnetopause is well correlated with the above wave propagation. The magnetopause initially moves inwards at a roughly constant rate until the reflected fast mode wave signal returns to the magnetopause (approximately at 17:23 UT). The inward motion then slows significantly as the wave is reflected back towards the inner magnetosphere. When this wave returns (approximately at 17:25 UT), the motion of the magnetopause actually reverses such that it moves away from the Earth (i.e., the magnetosphere expands). A few minutes later, the magnetopause motion ceases.

Such motion of the magnetopause has also been studied by *Samsonov et al.* (2007). Without numerical diffusion in the MHD code, this ringing of the magnetopause motion and bouncing of waves may have occurred for much longer.
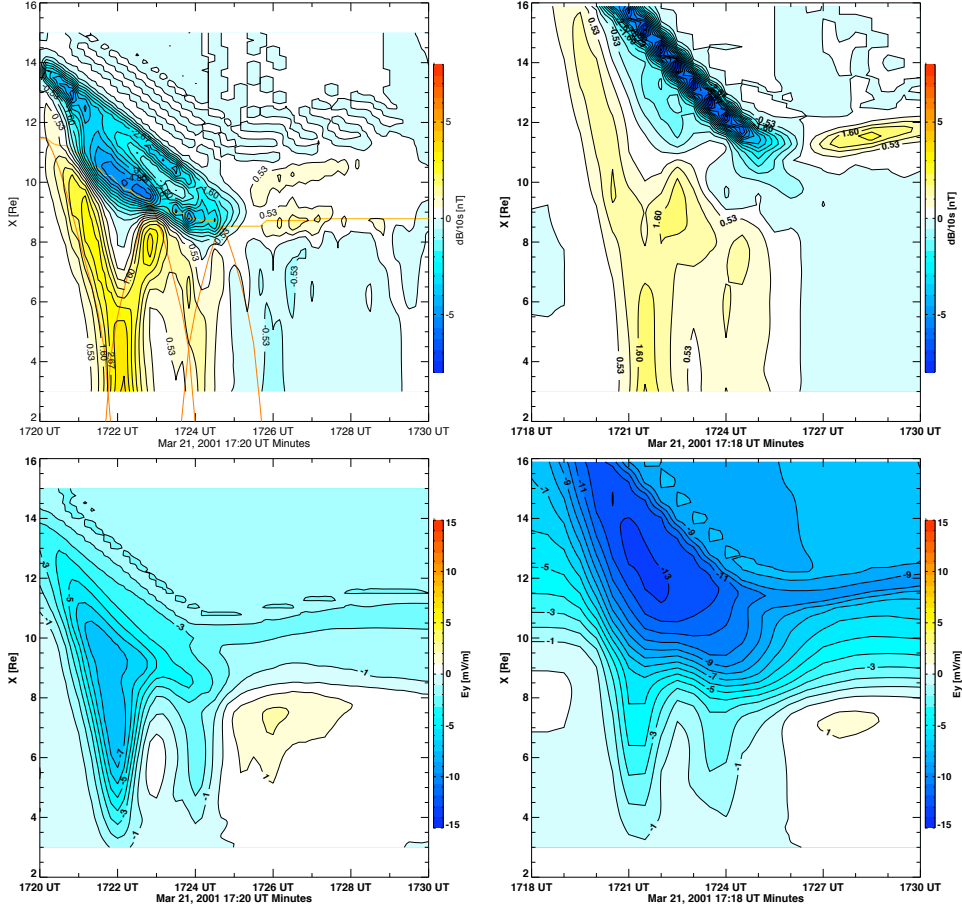
Figure 5.14: Results from two idealized simulations (Mach number = 8.0 and 2.0): top row shows the contour of dB_z/dt as a function of time on the Sun-Earth line from 3 R_e to 16 R_e, with left panel having a Mach number of 8.0 and the right one of 2.0. Bottom row is in the same format but the color represents the duskward inductive electric field on the Sun-Earth line.

The above two features (i.e., the bouncing of the fast mode wave and the expansion of the magnetosphere subsequent to the sudden compression) are confirmed by the variation of the inductive electric field after the sudden compression. Figure 5.14 (lower left) is the duskward inductive electric field E_y on the Sun-Earth line from 3 R_e to 15 R_e, after the sudden compression. Two waves of the large dusk-to-dawn electric

field propagate towards the Earth, consistent with the two earthward propagation of the fast mode waves from the magnetopause. Furthermore, a positive (dawn-to-dusk) electric field after 17:25:00 UT indicates a sunward motion of the plasma, which is associated with the expansion of the magnetosphere subsequent to the anti-sunward compression.

The dB_z/dt and the inductive electric field E_y contours from a lower Mach number case (Ma = 2.0) are also illustrated in the right column of Figure 5.14. Because of the difficulty in finding the magnetopause position based on the magnetopause current maximum in this case, the orange curves are not overplotted here. With a strong positive B_z in the solar wind, there is little dB_z across the magnetopause, and hence small current. An earlier start time is shown in the time axis, as the system reacts earlier than in the high Mach number case, but the vertical axis that represents the X position on the Sun-Earth line is the same, truncating portion of the thick magnetosheath during the early time period. Fortunately, the focus here is inside the magnetosphere. The wave reflection and the expansion of the magnetopause afterwards are also clearly produced. The differences in this case lie in the strength, the duration, and the depth into the magnetosphere of the wave penetration. It is observed that this low Mach number case is associated with weaker penetrations of E_y, which however lasts longer, into the inner magnetosphere (Figure 5.14, lower right), even though the electric fields in the solar wind and the magnetosheath are much stronger. Note that despite the weaker penetration of E_y into the inner magnetosphere, the E_y near the magnetopause, which is connected to the Ey-response in the ionosphere, has large magnitude because of large Bz in the magnetosheath. This verifies that the Ey-response in the CPCP profile shown in Figure 5.9 is stronger for lower Mach numbers, as discussed in section 5.3.

Figure 5.15 illustrates the dusk-to-dawn inductive electric field at 7 R_e on the Sun-Earth line within the dayside magnetosphere, as a function of time for different Mach
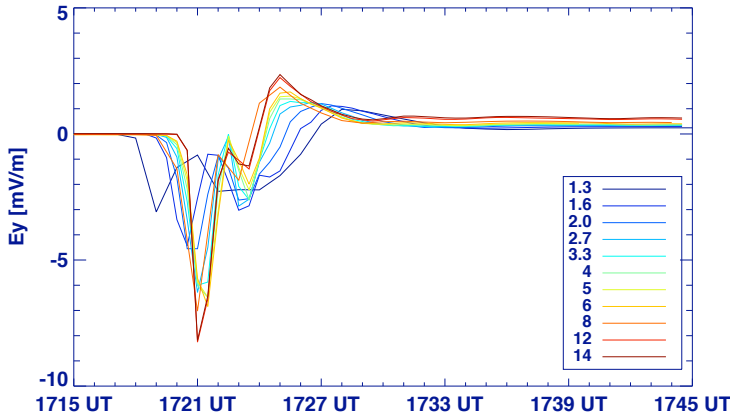
Figure 5.15: The duskward inductive electric fields at 7 R_e on the Sun-Earth line as a function of time, for different Mach number simulations.

numbers. The dusk-to-dawn electric fields (i.e., negative E_y) are significantly enhanced twice, seen in all of the simulations, indicating that the propagation-reflection of the fast mode wave exists in all of these cases, no matter how small the Mach number. The positive (duskward) peak, after the two strong increases of the dawnward electric fields, implies the expansion of the magnetosphere or the returning flow from the tail to the dayside. These are all consistent with the electric field contour plot in Figure 5.14. The final steady state in these cases is associated with positive (duskward) E_y, or sunward plasma flow, which is larger than the initial condition (žero E_y). This implies that the impact from the sudden compression not only changes the magnetospheric convection configuration, but also the convection strength. The initial configuration is mostly dominated by the co-rotation convection, but after the transient response, the two-cell convection is stronger. This is consistent with *Boudouridis et al.* (2008), who reported from case studies of sudden increases in the solar wind density that the ionospheric convection is enhanced, compared to the initial state, after the transient increase subsides.

Of the above two features, the bouncing feature of the wave propagation has been partly verified by GOES satellite observations. *Andréeová and Přech* (2007) and *Russell et al.* (1999) have both showed two-step response in the magnetic fields measured

by GOES satellites orbiting inside the dayside magnetosphere when it was suddenly compressed by an interplanetary shock. The two-step response in the magnetic fields consists of an abrupt increase and a subsequent gradual increase. *Samsonov et al.* (2007) attributed this feature to the wave reflection as explored in their paper: the sharp increase in the magnetic field is due to the first earthward fast mode wave and the gradual increase is caused by the reflected sunward moving fast mode wave. While these GOES observations and corresponding interpretations provide evidences of the primary earthward propagation of the fast mode wave and its reflection near the Earth boundary, the second earthward propagation of the wave reflected from the magnetopause lacks observational verification yet. *Samsonov et al.* (2007) also predicted the multiple bounces of the fast wave in global MHD simulations, but no observational evidence for these waves other than the primary one has been reported in the literature. It should be noted that the bouncing feature is also alternatively interpreted by the cavity mode waves inside the magnetosphere cavity (e.g., *Kivelson and Southwood* (1985), *Claudepierre et al.* (2009), *Waters et al.* (2002), *Takahashi and McPherron* (1982)). As the compressional fast mode wave has wave length in orders of the size of the magnetosphere cavity, it is possible that the waves are standing waves with the boundaries at the magnetopause and the Earth. But in this study, the cavity mode wave is not our concern.

Measurements from the electric field instrument (EFI) on board the THEMIS spacecraft (*Bonnell et al.* (2008)) are used to examine the dusk-to-dawn electric fields accompanied by the earthward propagation of fast mode waves. The THEMIS C spacecraft was located around (5.5, 0.5, -1) R_e in GSM coordinates when a solar wind density increase (rapidly from 5 to 10 cm^{-3}, and continuously up to 20 cm^{-3} within 10 minutes) arrived at the bow shock around 06:18 UT, June 2, 2007, as shown in Figure 5.16 which is obtained from OMNI2 data base. The measured dusk-to-dawn electric field is shown in Figure 5.17. Two enhancements of the dawnward
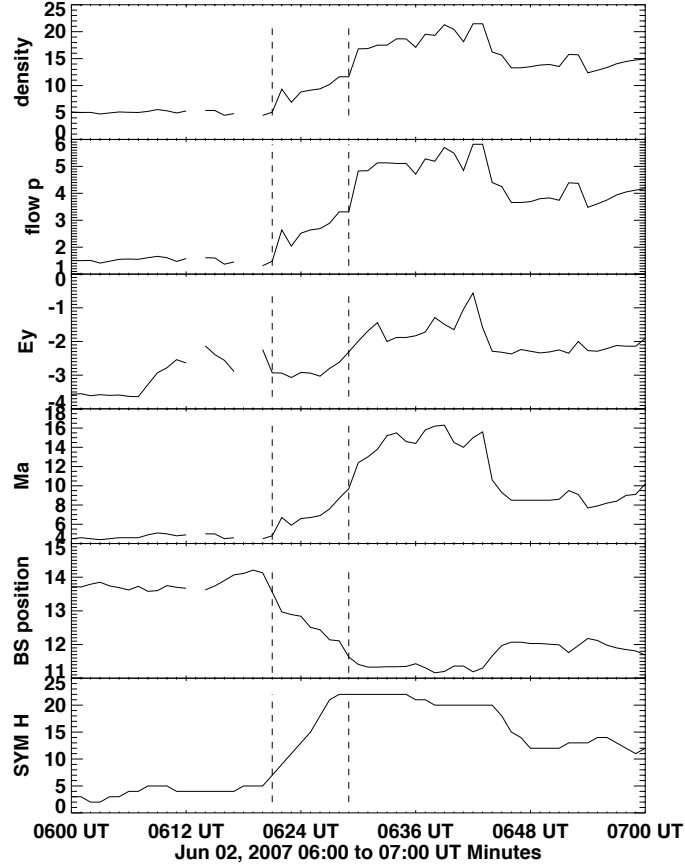
Figure 5.16: The solar wind density, dynamic pressure, electric field (y component), Alfvén Mach number, Bow shock position, and the SYM-H index for the June 02, 2007 event. The first dashed line at 06:21 UT the abrupt increase in the solar wind density that creates the earthward wave progation and the subsequent reflections.

electric field were observed at 06:19 UT and 06:24 UT respectively, which is consistent with the simulation results that the wave propagates towards the Earth twice. Note that the first enhancement of electric field occurred earlier than the arrival of high-density solar wind. This is most likely due to errors in the OMNI2 data calibration in propagating the data from their observation location to the bow shock. There are some discrepancies between this observation and our simulation result. First, the observed dawnward electric fields display a roughly consistent magnitude (1-2 mW/m) with the simulation results (2-3 mW/m). However, there exist a 5 minute gap between the two dawnward electric field enhancements, while in the simulations, the secondary

123
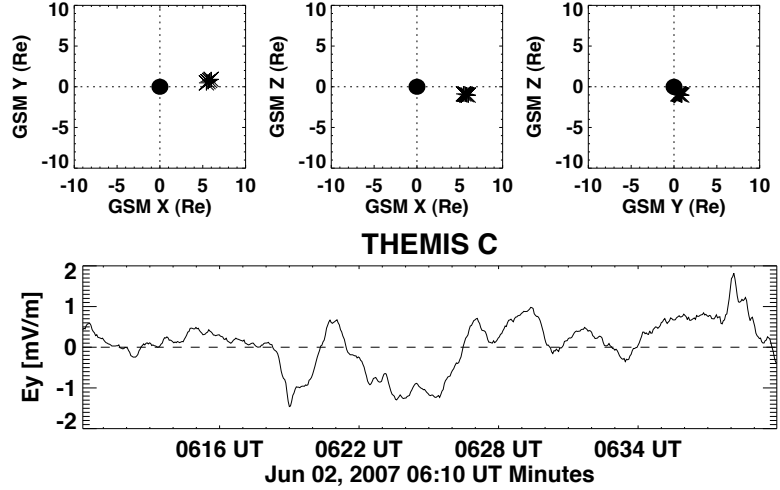
Figure 5.17: The duskward electric field observed by electric field instrument on board the THEMIS C spacecraft on June 2, 2007 when the spacecraft was orbiting within the dayside magnetosphere. The top three panels show the location of the spacecraft when a sudden solar wind density increase encountered the bow shock around 06:18 UT.

wave returns in just 2-3 minutes. This can be probably ascribed to the compression factor again. A factor of 4, as in our simulations, results in a larger earthward motion of the magnetopause and thereby a closer magnetopause boundary to reflect the wave towards the Earth. But with a factor of 2, as in the observation, the magnetopause moves less, so that it takes longer for the wave to reach this boundary and be reflected. Despite these differences between the observations and our simulations, the THEMIS electric field observations in the dayside magnetosphere indeed supply evidence for the multiple earthward traveling waves.

It should be noted that for the same event, the WIND spacecraft observed two density increases within a few minutes which could possibly produce two enhancements in the dawnward electric field within the dayside magnetosphere cavity. However, it is difficult to determine whether these enhancements of the electric field observed by THEMIS spacecraft are a result of wave reflections or of the external multiple increases in the solar wind density. One important uncertainty lies in the propagation of the solar wind discontinuity, as seen from the differences between the WIND ob-

124

servations and the OMNI2 data. The latter, which provides solar wind conditions at the bow shock after propagating solar wind conditions from WIND/ACE locations, however, only illustrates a single density increase in the solar wind. To be sure of the cause of the electric field enhancements, further investigations are needed, such as performing simulations of the real event and analyzing the propagation of the density discontinuity in the solar wind, which will be conducted in the future.

5.4.1 Consequence of these two enhancements of E_y

Since the Ey-response in the ionosphere is related with the dayside magneto-spheric dusk-to-dawn electric field E_y induced from the sudden compression, the two enhancements of the dusk-to-dawn electric field should correspondingly cause the ionosphere to experience the Ey-response twice. In Figure 5.10, which illustrates the residual FACs in the ionosphere, the first Ey-response (upward or yellow FAC around 10 MLT, and downward or blue FAC around 14 MLT at 70°) is seen at 17:21:00 UT while the second Ey-response of the same polarity appears at 17:23:30 UT, but at a lower latitude 64° and with an elongated shape. The second FAC pair appears at lower latitudes because of the closer position of the magnetopause as it moves towards the Earth after the sudden compression. This low-latitude FAC pair propagates poleward as well as towards the nightside while fading away quickly, and it is found to have little influence on the potentials or the ground magnetic perturbations. No ionospheric observations have yet reported on this second Ey-response since it is so subtle, but it is predicted by our simulations and is indirectly supported by the THEMIS/EFI observation. In that case, the response of the geospace system to the rapid increase of the solar wind density is no more two-phase, but at least three-phase: "Ey-response"-"Vortex-response"-"Ey-response". The third response, however, is too weak to actually have effects on the ionospheric electrodynamics. It could be that ground magnetometers with high resolution at proper latitude and lon-

gitude positions in a clear-cut event may detect such a weak and fast variation on the ionosphere. Note that a fourth pair of FACs emerges at 17:25:00 UT, resembling the Vortex-response, but, once again, has little influence on the system. This second Vortex-response indicates that the pair response (i.e., "Ey-response"- "Vortex-response") may have to always be a pair. Therefore, our simulations predicts at least two pairs of such groups, leading to a four-phase response in the system: "Ey-response"-"Vortex-response"-"Ey-response"-"Vortex-response". It is unclear whether there are more such two-phase responses subsequent to those. In our simulation so far, the wave amplitude at the dayside magnetosphere decreases significantly after two reflections, and hence two Ey-responses and two Vortex-responses are observed. Probably a stronger compression, which introduces a wave possessing stronger energy may allow the wave to reflect more times between the dayside magnetopause and the near-Earth boundary, could therefore produce more phases of the response. It should be noted that the ground-based observation (e.g., the magnetic field perturbation) or global activity index (e.g., CPCP) are not be able to reveal the second Ey-response or Vortex-response, given the fact that these responses are weak and more importantly appear at the time when the first Vortex-response is growing.

5.5   Conclusion

This chapter has studied the response of the geospace system to a sudden increase of the solar wind density by examining the observational data statistically and performing numerical simulations with different solar wind Alfvén Mach numbers. We have reached the following conclusions:

1. While the ground-based observation suggests that the response to a sudden increase of the solar wind density can be generally categorized into two groups: "two-phase response" and "single-phase response" based on whether or not both

an Ey-response and a Vortex-response turn up after the sudden compression of the magnetosphere, it is likely that the response may be a continuum.

2. The solar wind Alfvén Mach number plays an important role in determining the temporal variation, the strength, and the duration of the response to the pressure increase. The Alfvén Mach number alters the thickness of the magnetosheath and therefore the propagation characteristics of the discontinuity through the sheath. This leads the magnetosphere to react differently to similar density changes in the solar wind. In the lower Alfvén Mach number case, the Ey-response starts earlier and lasts longer than in the higher Alfvén Mach number case, and is then followed by a weaker Vortex-response.

3. In response to a sudden magnetospheric compression, a fast mode wave is launched. It propagates towards the Earth and is reflected back towards the magnetopause, where the wave is once more reflected back towards the Earth. The bouncing waves result in two enhancements of the dawnward inductive electric field in the dayside magnetosphere, a result that is supported by THEMIS/EFI measurements. The propagation-reflection of the wave in the dayside magnetosphere appear to be related to the inward and outward motion of the magnetopause.

4. Because the fast-mode wave is reflected back and forth between the magnetopause and the inner boundary, a train of ionospheric responses are observed. The two-phase response is actually a four-phase response, where the second group are most likely caused by the reflected waves from the magnetopause, and may be too subtle to be observed in the ionosphere.

CHAPTER VI

Exploring the Impact of Ionospheric Outflow on Magnetospheric Dynamics

The previous Chapters (III, IV, V) have investigated the impact of external driving (i.e., the solar wind or IMF discontinuities) on the magnetosphere-ionosphere system. This chapter will go a step further to explore the internal feedback taking place within the magnetosphere-ionosphere system: the ionospheric outflow into the magnetosphere.

6.1 Introduction

The ionospheric-origin plasma within the magnetosphere increases dramatically during storm times and potentially has a large feedback on the magnetospheric dynamics. The cause of the significant enhancement in the heavy ions inside the magnetosphere has been extensively investigated recently. For example, *Ashour-Abdalla et al.* (2009) observed ionospheric O^+ flowing into the magnetosphere from Cluster located 5 R_e above the auroral ionosphere 2 hours before a substorm and a large flux of ionospheric energetic ions after the substorm at THEMIS located in the near-Earth tail. They conducted an MHD simulation of this event and concluded that the acceleration of the ionospheric O^+ occurs near the plasmasheet boundary of the near-Earth

tail by non-adiabatic motions. *Nosé et al.* (2005) attributed the extreme increase in the O^+/H^+ energy density ratio during a storm to the mass-dependent acceleration of ions by storm-time substorms which leads to an additional supply of O^+ from the ionosphere. This mechanism is further verified by *Nosé et al.* (2009b) through coordinated observations. *Zong et al.* (2008) observed O^+ dominated bursty bulk flows (BBFs) during a strong magnetic storm, implying that the O^+ could be carried into the ring current region by bursty flows. *Nosé et al.* (2010) analyzed the magnetic fluctuations during dipolarizations in the inner magnetosphere and proposed that the O^+-rich ring current is generated from local and non-adiabatic acceleration of the pre-existing thermal O^+ in the outer plasmasphere through magnetic fluctuations.

As the ionospheric heavy ions can flow out of various regions (e.g., dayside cusp region, polar cap, aurora oval, etc.) in the ionosphere, a number of researchers have studied the ionospheric outflow from different source regions. For instance, *Moore et al.* (2005) used collisionless test particles in magnetic and electric fields obtained from MHD simulations to trace polar wind H^+ and auroral wind O^+ from the ionosphere to the ring current. They found that under active conditions, the auroral wind dominantly contributes to the ring current. *Peroomian et al.* (2006) followed the dayside cleft ion fountain during a magnetic storm by large-scale kinetic particle tracing technique using time-dependent electric and magnetic fields from a magnetosphere MHD model. They showed that both the O^+ number and energy densities in the plasma sheet increase significantly after a storm sudden commencement. Utilizing single particle trajectories in multi-fluid MHD simulations, *Winglee* (2003) found a strong local time dependence for ionospheric outflow acceleration. Cusp heavy ions could reach the neutral sheet and experience acceleration but the major contributors to the ring current were heavy ions from the dawnside auroral oval that can dominate the symmetric ring current. *Delcourt et al.* (1989) systematically studied different ionospheric outflows (auroral, polar cap, cusp, and polar wind) using

a three-dimensional particle trajectory tracing technique in empirical electric and magnetic fields and found that during highly disturbed times, the plasma sheet is dominated by ionospheric O^+ ions that mainly originate from the cleft ion fountain. *Harnett et al.* (2008) simulated the 29 October 2003 Halloween storm and showed that a southward IMF drove an initial ionospheric outflow in the cusp region that supplied mass to the magnetosphere, which experienced prompt acceleration. The nightside auroral O^+ outflow was subsequently driven to resupply the mass loading of the magnetosphere. *Wiltberger et al.* (2010) simulated cusp outflow into the magnetosphere and discovered that the outflow drives a more unstable magnetotail than when there is no outflow. *Garcia et al.* (2010) systematically investigated the role of O^+ intensity out of the nightside aurora in determining the plasma sheet density and pressure and their relationship with the cross polar cap potential (CPCP) index, tail geometry, and magnetospheric convection. *Brambles et al.* (2010) compared one simulation with only hot cusp outflow with another simulation with a global cold ionospheric outflow, using the LFM MHD code. They found that the tail X-line is farther tailward in the latter case and that the outflow reduces the CPCP index, which is consistent with other studies such as those of *Glocer et al.* (2009a), *Winglee et al.* (2002), and *Wiltberger et al.* (2010). To summarize the above studies, the changes within the magnetosphere-ionosphere system due to the ionospheric outflow are notably dependent on the source location and the outflow intensity.

The ionospheric mass source is critically important in influencing magnetospheric dynamics, including the dayside reconnection rate, tail dynamics, and ring current energization. This chapter explores the effect of outflow origin on the dayside reconnection rate and tail dynamics and will elucidate the role of heavy ions in determining tail stability and thereby substorm occurrence. In addition, this chapter will investigate the influence of the ionospheric outflow intensity on magnetospheric dynamics. These goals require different model configurations, not only in grid resolution but also

in the inner boundary conditions. The detailed configurations are described below.

6.2 Ionospheric outflow from different source regions

The study in this chapter again uses the near-Earth models from the SWMF, as described in Chapter II. Different from the simulations performed in previous chapters, simulations carried out here solve the multi-fluid MHD code that includes both $H+$ and O^+ fluids.

6.2.1 Methodology

For the purpose of studying the reconnection rate at the dayside magnetopause, a high grid resolution and high resistivity are required (*Borovsky et al.* (2008)). This facilitates physical reconnection instead of numerical reconnection in which numerical resistivity drives magnetic field reconnection. Anomalous resistivity is implemented in order for the MHD code to capture a reasonable reconnection rate, according to *Birn et al.* (2005), who compared MHD simulations with kinetic, hybrid, and particle simulations and concluded that MHD simulations with a high enough anomalous resistivity is capable of achieving the necessary fast reconnection rate.

The adaptive mesh refinement technique in the BATS-R-US code enables a high resolution of 1/16 R_e in the limited but interesting region (i.e., magnetopause in this study) from X: [6, 16], Y: [-12, 12], Z: [-12, 12] R_e . This region covers the possible area where reconnection occurs on the dayside magnetopause boundary. Additionally, a 1/8 R_e grid resolution is applied around the planet body. The global resolution structure for the magnetosphere is shown in Figure 6.1. Furthermore, a current-dependent anomalous resistivity η is adopted in the global domain:

$$\eta = \eta_0 + min(\eta_{max}, max(0.0, \eta_{a0}(\frac{|J|}{J_C} - 1)))$$
(6.1)

where constants η_0, η_{max}, η_{a0}, and J_c are chosen to be 1.0×10^9 m^2/s, 2.0×10^{10} m^2/s, 2.0×10^9 m^2/s, and 1.0×10^{-9} A/m^2, respectively. From Equation 6.1, the anomalous resistivity η is large in areas where the current density exceeds the certain threshold J_c, while it is small in the rest of the simulation domain. Note that this formula can not exclude regions such as near-Earth boundary at polar caps where the field-aligned current could be large.
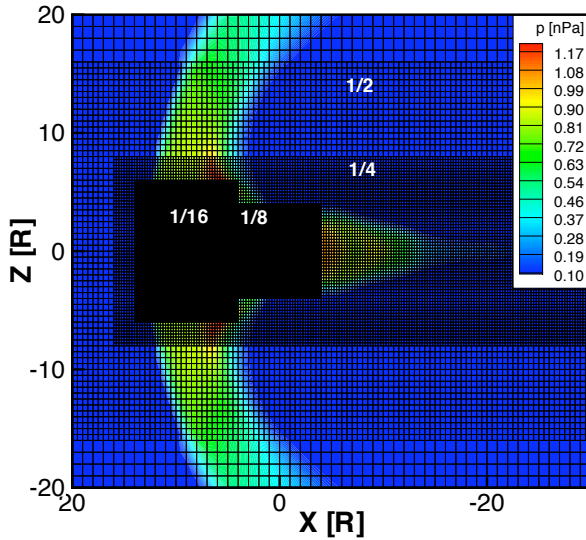

Figure 6.1: The grid setup in the outflow simulations A and B, viewed from the noon-midnight meridian plane. The Sun is to the left. The dayside magnetopause and near-body are resolved by 1/16 and 1/8 R_e cells respectively. The 1/4 R_e resolution covers region from 16 R_E on the dayside to -32 R_e in the tail. The color shows the thermal pressure in nT. The whole simulation domain covers from 32 R_e on the dayside to 228 R_e on the nightside, and 128 R_e in the dawn-dusk and north-south directions.

To simulate the ionospheric outflow, artificial boundary conditions are imposed at the inner boundary of the MHD model. Note that a variety of configurations in MHD simulations have been used initialize to the ionospheric outflow. Recently, a popular method in studying the ionospheric mass outflow in MHD simulations is to apply an empirically driven formula, serving as an inner boundary condition of the global magnetosphere MHD model (e.g., *Gagne* (2005); *Brambles et al.* (2010); *Moore et al.* (2010)). In these studies, the Strangeway formula (*Strangeway et al.* (2005)) is applied

132

to specify the O^+ ion number flux at the inner boundary of a global magnetospheric MHD code. The Strangeway formula (or so-called "scaling law") was derived from a large number of FAST observations when the satellite flew over the cusp region at 4000 km altitude; therefore, after scaling and mapping up to the inner boundary at 3 R_e (a typical radius of the inner boundary of a global magnetosphere model), the application of the formula into the entire polar cap region would probably over-estimate the total outflow rate. Furthermore, the multi-fluid MHD code requires number density, velocity, and temperature of individual ions (such as O^+ and H^+ ions) in order to initialize the boundary conditions, but the Strangeway formula only provides the information of O^+ number flux.

A different method of incorporating the ionospheric outflow into a MHD model is to couple with a self-consistent ionospheric outflow model. *Glocer et al.* (2009b) implemented a first principle polar wind outflow model (PWOM) into the Space Weather Modeling Framework (SWMF) (*Tóth et al.* (2005)), which self-consistently represents the physics in the driving mechanisms of the upwelling and outflow as well as in the feedback from the global magnetosphere. However, this PWOM, a real-time and 3D global model, mixes ionospheric plasma originating from different source regions and hence is incapable of achieving the goal of investigating the outflow origin dependence of the magnetospheric dynamics.

Different from above observation-regulated outflow or self-consistent outflow, *Garcia et al.* (2010) used constant outflow conditions over a night side auroral region to intentionally examine the single effect of the night side outflow intensity. In this study, we will also specify a simple constant area-confined outflow at the inner boundary of the global magnetosphere MHD model to understand the perplexing interactions inside the non-linear MI system.

Two simulations are carried out to examine the outflow origin dependence of magnetospheric dynamics. For the simulation that investigates cusp outflow (Simulation
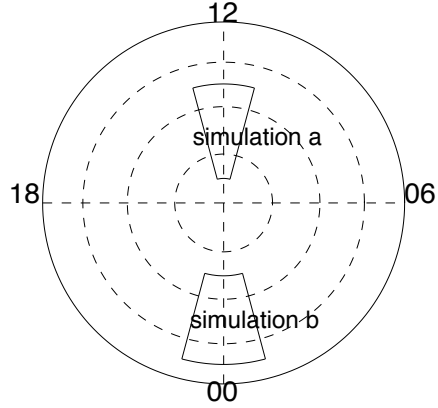
Figure 6.2: The artificial ionospheric outflow specified at the inner boundary of the MHD model BATS-R-US for two simulations. Simulation A enforces an outflow in the dayside cusp region from 65 to 85° magnetic latitude and from 11 to 13 magnetic local time. Simulation B specifies the outflow in the night side auroral region from 55 to 75° magnetic latitude and from 23 to 01 magnetic local time across the midnight.

A), the ionospheric plasma flows out from a wedge-shape region at the inner boundary from 65° to 85° (i.e., 75.8° to 87.1° at the ionosphere boundary if mapped down along dipole magnetic field lines) magnetic latitude and from 11 to 13 magnetic local time (MLT), while the simulation with night side auroral outflow (simulation B) uses the similar wedge-shape region but on the nightside from 23 MLT to 01 MLT across the midnight and from 55° to 75° (i.e., 75.8° to 87.1° at the ionosphere boundary) magnetic latitudes. Both source regions are illustrated in Figure 6.2. The boundary parameters (density, velocity, temperature for both ion components) in both simulations are constant: $N_{O+} = 20\ cm^{-3}$, $V_{O+||} = 20\ km/s$, $T_{O+} = 1000,000K$, $N_{H+} = 10$ cm^{-3}, $V_{H+||} = 0\ km/s$, and $T_{H+} = 100,000\ K$. The rest of the sphere boundary is specified by: $N_{O+} = 0.01\ cm^{-3}$, $V_{O+||} = 0\ km/s$, $T_{O+} = 25,000\ K$, $N_{H+} = 28\ cm^{-3}$, $V_{O+||} = 0\ km/s$, and $T_{H+} = 25,000\ K$. Here, "||" denotes the upward direction along the magnetic field line. The ionospheric plasma begins to flow out of these specified regions at the inner boundary of the MHD model after 3 hours when the system, driven by constant solar wind conditions ($N_{sw} = 5\ cm^{-3}$, IMF $B_z = -5\ nT$,

134

$B_x = B_y = 0$, and $V_x = 400\ km/s$) and zero ion outflow, reaches a roughly steady state. Note that these boundary conditions are only for experimental investigations. Different outflow density, velocity, or temperature could possibly lead to different simulation results, which will be noted later in the text.

6.2.2 Simulation results

As mentioned in Chapter I, pathways of the ionospheric O^+ ions from either the cleft or nightside auroral region have been identified through coordinated insitu measurements (e.g., *Elliott et al.* (2007)). Particle modeling has been able to trace the trajectory as well as the fate of the ionospheric O^+ ions (e.g., *Ebihara et al.* (2006)). Here, MHD simulation results also provide a thorough view of the ionospheric plasma transport inside the magnetosphere. The simulations not only observe the path from the source region to the plasma sheet as suggested by observational studies, but also further indicate a more complete circulation of the ions transport. After the O^+ arrives at the dayside magnetosphere and then the magnetopause after convecting around the Earth from the nightside, the O^+ ions are captured by dayside reconnection and ejected towards the cusp region, eventually precipitating down to the ionosphere. The new energy source into the ionosphere would further help heat up the ionospheric plasma and escape into the magnetosphere.

The pathway in the X-Z plane that the heavy ions take from the ionospheric cusp region to the plasma sheet is illustrated in Figure 6.3 (i.e., in Simulation A). Color represents the number density of O^+ ions on a log scale and lines represent the magnetic field lines. Originating from a restricted region in the ionosphere, the majority of the plasma out of the cusp region first travels upward along the magnetic field and then tailward across the high-altitude polar cap with the help of tailward streaming solar wind. Note that due to numerical diffusion across grid cells in the presence of a large pressure gradient, the designed 20° outflow band is broadened,

and a small portion of O^+ also diffuses across the magnetic field to lower latitudes and leaks into the dayside magnetosphere cavity. Nevertheless most of the outflow plasma streams into the lobe region and is captured by tail reconnection which ejects the plasma earthward. These heavy ions then travel preferentially along the magnetic field lines towards higher latitudes in both hemispheres, forming a bifurcate pattern along the plasmasheet boundary on the X-Z plane , and then diffuse into the inner magnetosphere.

Figure 6.4 shows the flow path of heavy ions out of the night side auroral region (i.e., in Simulation B). Most of the ionospheric ions flow directly into the inner magnetosphere along closed field lines without going through the tail reconnection site, while some ionospheric ions on open field lines stream down to the tail along the plasma sheet boundary and participate in the tail reconnection, but at a much smaller level than in Simulation A. Note that even though the primary outflow occurs on the nightside, the upwelling along the field lines is again accompanied by perpendicular numerical diffusion so that a small amount of outflow ions escape into the dayside magnetosphere.

6.2.2.1   On the tail dynamics, CPCP index, and magnetopause location

In this section, the influence from these two different outflow sources will be examined. Figure 6.5 illustrates the cross polar cap potential (CPCP) index, the tail X-line position on the Sun-Earth line, the earthward ejection speed in reference frame of reconnection site, and the D_{st} index for Simulations A (solid) and B (dashed). After the outflow occurs at 03:00, the cross polar cap potentials in both simulations (top plot) are reduced followed by a small recovery. The reduction in CPCP index caused by the mass outflow is consistent with earlier studies (e.g., *Brambles et al.* (2010); *Glocer et al.* (2009a); *Winglee et al.* (2002)), but it differs in the magnitude between these two simulations. The CPCP index in Simulation A decreases more,
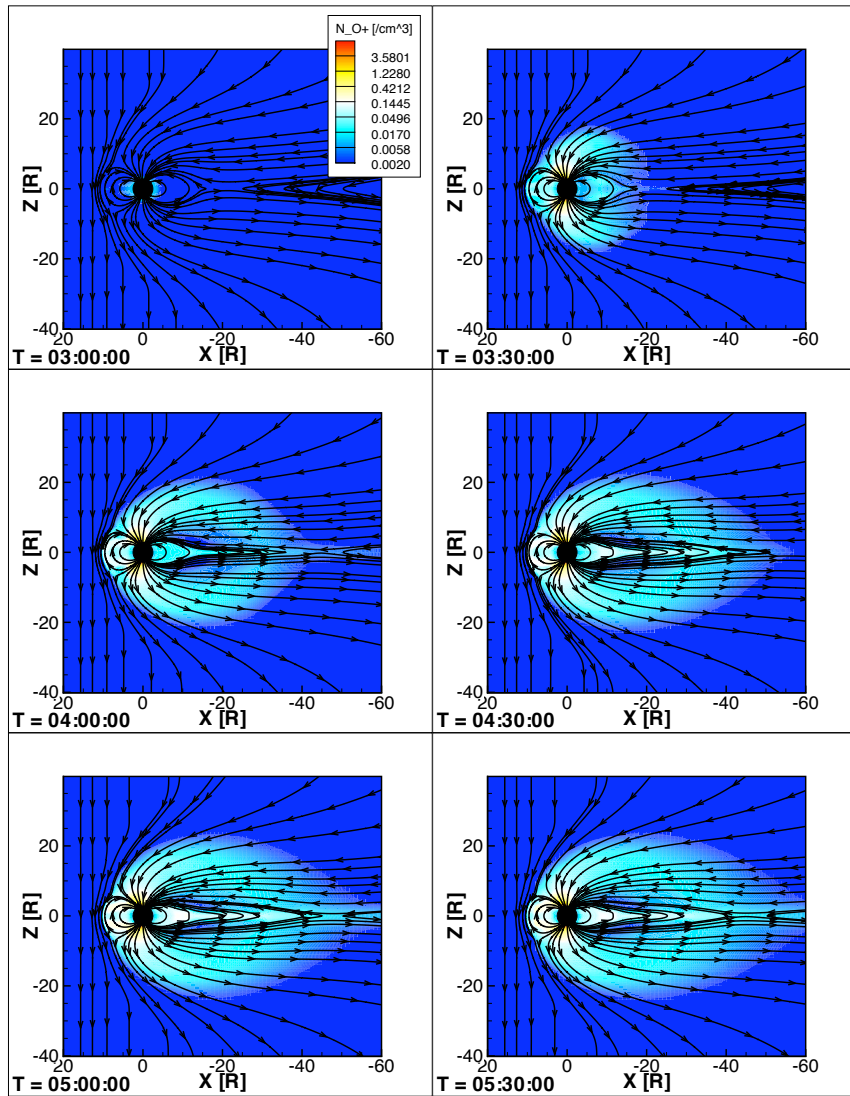
Figure 6.3: The evolution of ionospheric O^+ outflow from the dayside cusp region starting at 03:00. Color represents the number density of O^+ and the lines are the magnetic field lines.
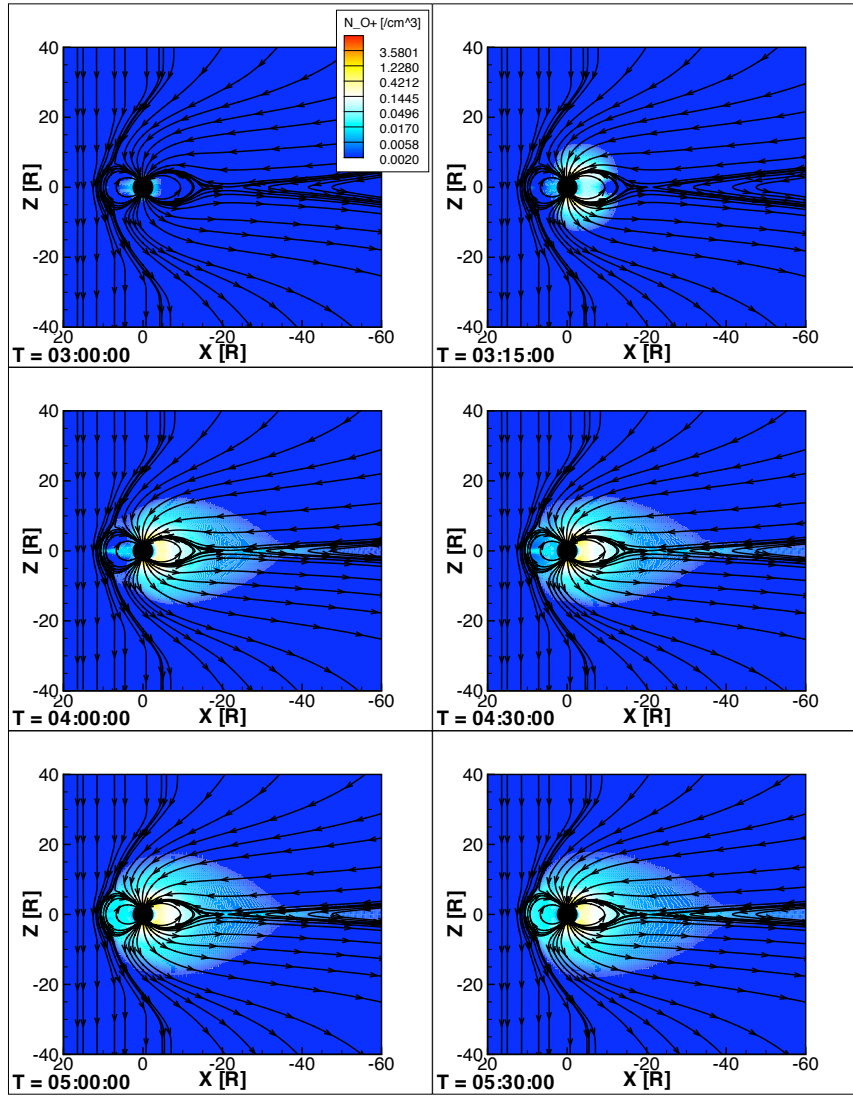
Figure 6.4: The evolution of ionospheric O^+ outflow from the nightside auroral region starting at 03:00. Color represents the number density of O^+ ions and the lines are the magnetic field lines.
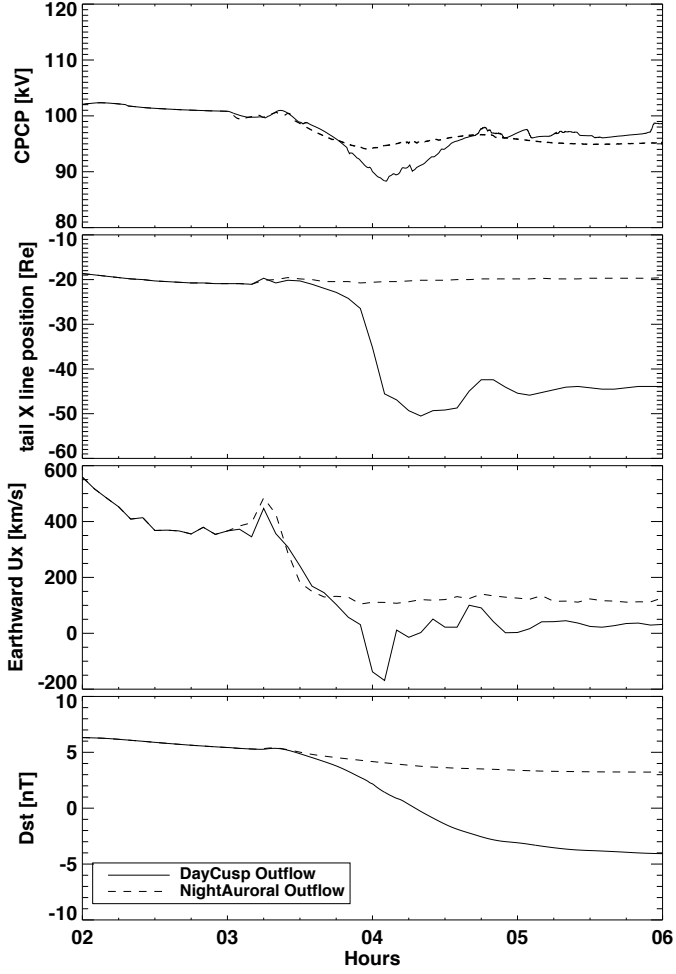
Figure 6.5: The CPCP index, tail X-line position, earthward ejection speed on the earthside of X-line, and the D_{st} index for Simulation A (solid) and B (dashed).

indicating that the influence of cusp O^+ outflow is more profound, although it has less outflow fluence due to a smaller outflow area. Furthermore, the CPCP recovers to a slightly higher level in Simulation A.

The tail dynamics (second plot) in these two outflow configurations demonstrates striking differences after the outflow. The magnetotail appears quiet and steady with the X-line staying around -20 R_e in Simulation B, while the tail in Simulation A experiences dramatic changes. In the latter case, the X-line location shifts from the original position to as far as -50 R_e down tail, followed by a earthward motion half an hour later before the tail finally relaxes to a relatively steady position at -44 R_e.

These dramatic changes are caused by the O^+ reaching the tail plasma sheet, where the increasing pressure and mass density eventually break up the far tail, ejecting plasma towards the Earth. The position of the tail X-line changes so fast that the earthward plasma motion away from the reconnection site appears to be tailward in the reference frame of reconnection (negative velocity in the third plot). After the X-line settles down, the earthward plasma convection out of the tail reconnection site is significantly smaller compared to when there is no outflow, which is a signature of reduced tail reconnection rate. This reconnection rate reduction is also observed in Simulation B, even though the tail stays steady: the earthward ejection speed drops by a factor of 4 after the outflow, however less so than that in Simulation A where the speed is reduced approximately by a factor of 8.

The D_{st} index, serving as a proxy of the strength of the ring current and the total amount of energy in the inner magnetosphere, shows a small magnitude in both simulations (bottom plot), because no inner magnetosphere model has been included in these simulations to realistically capture and represent the kinetic behavior of charged particles. The ring current is therefore not as intensified as it should be under the specified solar wind and IMF conditions. However, regardless of this weak manifestation of the ring current in the MHD model, the difference between these two simulations is still clearly demonstrated. In Simulation A, the index decreases rapidly about half an hour after the outflow and saturates in the last hour. In Simulation B, little change in observed. The change in Simulation A is associated with the formation of a weak ring current. As the plasma out of the cusp region (Simulation A) passes through the tail reconnection site, it is accelerated and adiabatically heated as it travels towards the Earth, providing the plasmasheet and ring current with hotter particles. Figure 6.6 illustrates the evolution of the ring current, which starts to build up after 04:00 when the reconnection site moves tailward. This indicates that the tail reconfiguration provides an energization mechanism to those particles from the tail
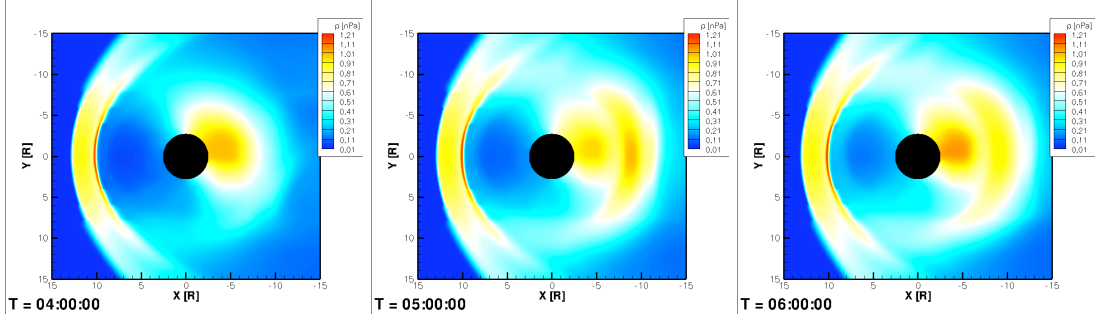
Figure 6.6: The evolution of the ring current (banana shape) in the equatorial plane after 04:00 in Simulation A where the ionospheric outflow is originated from the cusp region. The pressure bulge near the body results from inner boundary condition at low latitudes in the MHD code.

reconnection. With a larger tail, the plasma can undergo more adiabatic heating too.

As constracted with the ionospheric plasma from the night side auroral region (Simulation B) directly moves into the inner magnetosphere without going through the tail reconnection site. The heavy ions easily and quickly leak into the inner magnetosphere since a large portion of the outflow originates on closed field-lines and supplies cold particles to the near-Earth plasmasheet. Therefore a ring current is barely formed.

Note that the difference in the D_{st} index between these two simulations is as small as 9 nT, which would be very easily overlooked if an inner magnetosphere model were included and a strong ring current were to develop. In that case, the differences in the D_{st} index resulting from the outflow impact from different source regions would probably be negligible and an incorrect conclusion would be drawn regarding the impact of different outflow sources. The investigation here without utilizing the inner magnetosphere model on the other hand demonstrates remarkable differences in terms of the role in energizing the ring current played by different outflow sources.

The magnetopause motion following the ionospheric outflow is also of interest. *Brambles et al.* (2010) found both outward and inward motion of the magnetospause after the dayside magnetosphere cavity was populated with new heavy plasma from

different outflow regions with different thermal conditions. In this study, while simulation B barely shows any motion of the magnetopause, Simulation A indicates that after the initialization of outflow in the cusp region, the magnetopause travels towards the Earth as far as 0.45 R_e within two hours (Figure 6.7 (left panel)), approximately equal to a speed of 400 m/s, and then it moves outwards slightly. The inward motion of the magnetopause is likely associated with the decrease of the magnetic field magnitude just inside the magnetopause (this will be discussed below), since the magnetopause occurs where the solar wind ram pressure equals the magnetic pressure of the magnetospheric field just inside the magnetosphere and the solar wind conditions in this study remain constant.
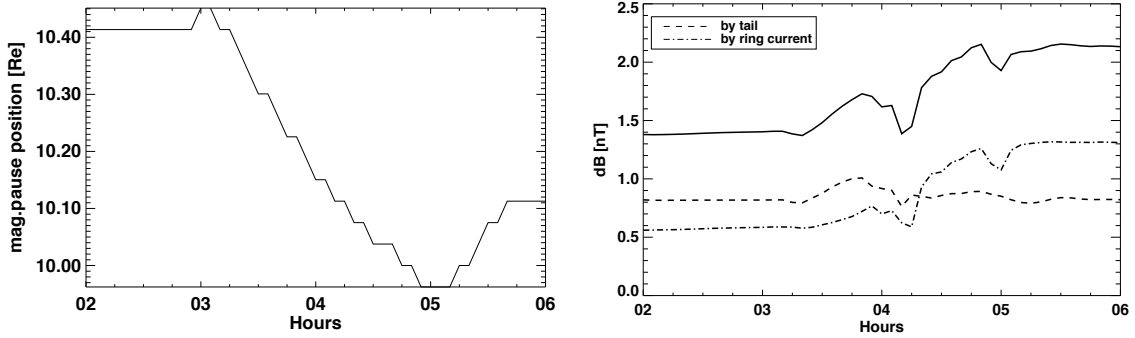
Figure 6.7: Left panel: The position of the subsolar dayside magnetopause as a function of time. Right panel: magnetic fields at 9 R_e on the dayside Sun-Earth line induced by ring current source (dash-dot) and tail current (dash) source in a box of (X:[-5,-10] R_e, Y:[-14,14] R_e, Z: [-2,2] R_e) and (X:[-14,-35] R_e, Y:[-14,14] R_e, Z: [-0.5,0.5] R_e) respectively.

The reason for a decreased magnetic field in the dayside magnetosphere is that two magnetospheric current systems are strengthened: (1) the tail current is strengthened due to the extended thinner magnetotail and (2) a ring current is formed in the night. These two current systems induce southward magnetic fields, partially counteracting the intrinsic northward geomagnetic field in the dayside magnetosphere cavity, causing the magnetosphere to shift inward. Figure 6.7 (right panel) shows the magnetic fields induced by the tail current (dash) and the ring current (dash-dot) at a subsolar point

at 9 R_e. The magnetic field is calculated by the Biot-Savart integral over 3D volumes of (X:[-14,-35] R_e, Y:[-14,14] R_e, Z: [-0.5,0.5] R_e) for the tail current and (X:[-5,-10] R_e, Y:[-14,14] R_e, Z: [-2,2] R_e) for the ring current. The induced magnetic field from the tail current is initially positive and shows small increase, but the contribution from the ring current begins to increase after tail reconfiguration and then contributes a significantly larger perturbation than the tail current. It should be noted that the real induced magnetic field may be larger than the above estimated value, as the integral volume chosen here does not comprehensively cover the ring current because of its partial ring-shape around the Earth rather than a rectangular box.

6.2.2.2   On the reconnection rate

The O^+ ion is known to play an important role in affecting the reconnection that occurs when the frozen-in theorem in the ideal MHD no longer holds. When both ions and electrons gyrate around a magnetic field line with no sharp gradient in it and move with it, no reconnection is possible. However, when the spatial scale of the magnetic field gradient approaches the ion gyroradius, the ion gyromotion around the field lines is no longer uniform and the ions become unmagnetized, so that the frozen-in condition for the ions is no longer valid. The participation of heavy ions such as O^+ increases the ion gyroradius and thus increases the possibility of reconnection when there are gradients in the magnetic field. The increased mass density will also decrease the Alfvén speed and hence the reconnection rate.

Two reconnection rates are studied here: the local reconnection rate and the global reconnection rate. The local reconnection rate is measured at the subsolar magnetopause using the Cassak-Shay (CS) formula (*Cassak and Shay* (2007); *Borovsky et al.* (2008)):

$$CS = 2(B_1 B_2)^{3/2}(\mu_0 \rho_1 B_2 + \mu_0 \rho_2 B_1)^{-1/2}(B_1 + B_2)^{-1/2} \qquad (6.2)$$

where B and ρ are magnetic field and mass density respectively; the indices "1" and

"2" denote the magnetosheath and magnetosphere sides respectively. μ_0 is vacuum permeability. This formula clearly indicates a density and magnetic field dependent reconnection rate, and has been confirmed by *Borovsky et al.* (2008) that this CS reconnection rate is consistent with the reconnection electric field represented by ηJ at the magnetopause with a modification factor of 0.1 (η is resistivity and J is current).

The local reconnection rates for simulations A and B are illustrated in Figure 6.8 (top) after choosing the magnetosheath and magnetospheric parameters (ρ, B) at positions where they start to steeply change towards the magnetopause. Both reconnection rates are reduced after the ionospheric O^+ ions enter the magnetosphere, but the differences between the two rates lie in the time when the rate reaches its minimum value as well as the magnitude of the depression. In Simulation A, there is a dip right after 03:00 which is followed by a quick rebound between 03:15 and 04:00, before a large depression. Although the flux rate of the ionospheric O^+ out of the cusp region (Simulation A) is smaller than in Simulation B due to its smaller outflow area, the reconnection rate is nevertheless depressed more (down to $7.7mV/m$ in Simulation A and $8.0mV/m$ in Simulation B). Furthermore, the depression lasts longer before the reconnection rate recovers.

To interpret these changes in the local reconnection rate, analyzing the ambient plasma information is requisite, as the reconnection rate is determined by the ambient plasma properties according to the Cassak-Shay formula (Equation 6.2). Figure 6.9 shows magnetic field (blue) and mass density (black) on the magnetospheric side of the subsolar magnetopause in Simulation A. The total mass density just inside the nose of the magnetopause is enhanced immediately after the outflow, consistent with the quick dip shown in the reconnection rate. Such an increase of mass density is associated with the mass diffusion away from the confined outflow region into the magnetosphere cavity, as observed earlier in Figure 6.3. However, the prominent
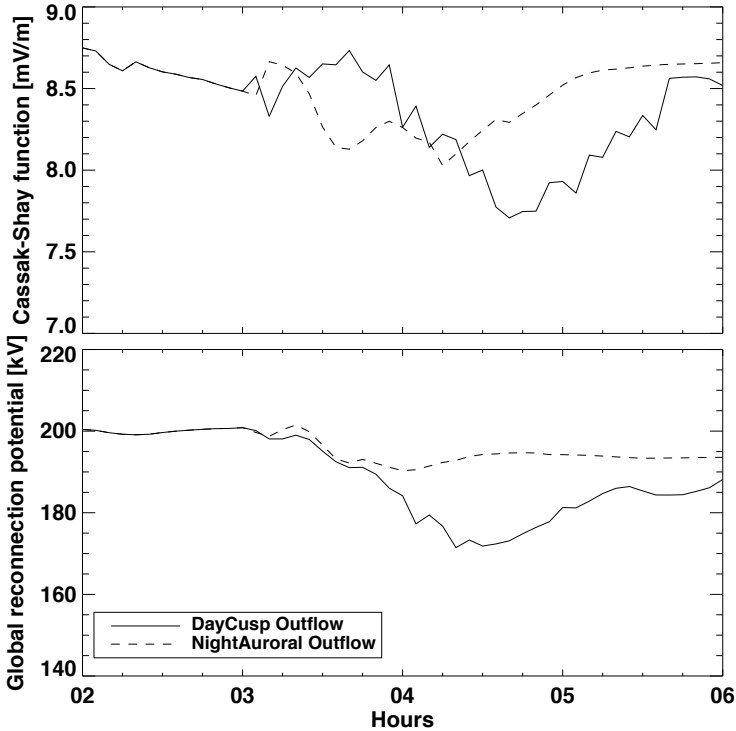
Figure 6.8: Local reconnection rate (top) and global reconnection rate (bottom) for Simulation a (solid) and b (dashed).

influence from the mass density occurs after 04:00 when the total mass density is enhanced, which significantly weakens the reconnection rate. Taking advantage of the multi-fluid MHD simulation, individual fluid properties can be traced; the densities for two individual fluids are shown separately. O^+ ions constitute a small percentage in the total mass density so that the increase in H^+ density plays the predominated role in decreasing the reconnection rate. However, the mass density change at the magnetopause is not the sole factor of the reduction in the reconnection rate. The magnetic field is gradually attenuated after 04:00 and reaches a relatively steady state after 05:00. Both the diminished magnetic field and the enhanced mass density near the subsolar magnetopause are responsible for the decreased subsolar reconnection rate.

Although the heavy O^+ ions have little direct effect on the reconnection rate due to their relatively small density at the dayside magnetopause, they play an indirect

145
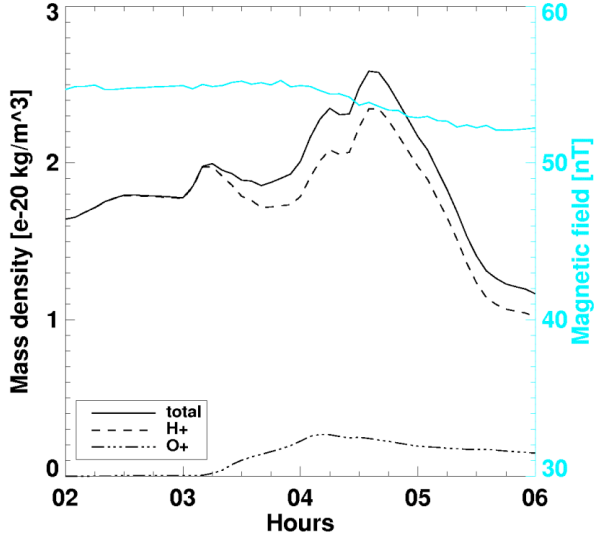
Figure 6.9: The mass density for total (solid), H^+ (dashed), O^+ (dash-dot) ions, and magnetic field (blue) in the magnetospheric side of the subsolar magnetopause in Simulation A.

role in changing the reconnection rate by influencing the global magnetospheric dynamics, which in turn directly changes the reconnection rate. For example, the O^+ outflow changes the H^+ dynamics inside the magnetosphere. Particularly, the O^+ outflow causes a plasma plume to shift across the nose of the magnetopause, which subsequently experiences changes in its ambient density. Figure 6.10 shows a high-density plume in the equatorial plane, which is primarily comprised of H^+ even after the arrival of O^+ heavy ions. The plume extends from the corotating ionosphere and connects with the subsolar magnetopause. Initially, the connecting bridge of the high-density plume with the magnetopause is slightly dawnward of the subsolar point, but after O^+ outflow, it starts to move dawnward, causing the subsolar magnetopause to experience the denser plume; the bridge further moves dawnward and later the plume detaches with the subsolar magnetopause as the magnetopause stops its inward mo-

146

tion. These movements of the plume and the narrow bridge with the magnetopause directly bring about the variation of H^+ mass density on the subsolar magnetopause. The dawnward shifting of the plume is a result of asymmetric convection between the dawn and dusk magnetosphere, which is probably associated with the tail reconfiguration from which the tail transfers more plasma momentum towards the dusk side. Another change inside the magnetosphere that is enabled by the O^+ outflow but has
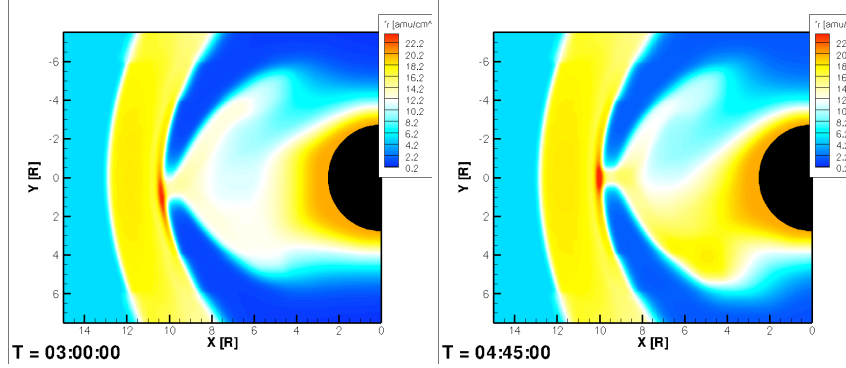
Figure 6.10: Plasma density in the dayside magnetosphere on the equatorial plane at two different times. Initially, the plume is connected to the dayside magnetopause slightly offsite the subsolar point. After the outflow, the bridge that connects the plume and the magnetopause shifts towards the dawn side. The plume is also intensified in the density.

a direct effect on the reconnection rate is the attenuation of the magnetic field inside the magnetopause. Such change in the magnetic field is ascribed to the O^+ outflow that places a large mass source to the tail plasma sheet, which elongates the tail, generates a large tail current, and forms a ring current. These current dynamics are especially clear in Simulation A, as discussed earlier.

In contrary to these dynamic changes in the magnetospheric plasma and field in Simulation A, the magnetospheric field near the subsolar point in Simulation B demonstrates little change. The mass density increases and declines, with the changes predominantly from H^+ ions, implying that the changes in the H^+ mass density is nearly the only factor that alters the reconnection rate in Simulation B.

The global reconnection rate is represented by the potential drop (i.e., the max-

imum potential minus minimum potential) along the merging line on the dayside magnetopause. For an idealized simulation with zero tilt angle of the magnetic dipole axis, the merging line can be easily determined by selecting the minimum magnetic field across the magnetopause on the equatorial plane. Using an ideal MHD code, *Hu et al.* (2009) studied the electric potential along the merging line under idealized solar wind conditions for various IMF B_z orientations and compared three different methods of calculating the electric potential at any point of the merging line, which were suggested to be consistent with each other. These three methods were: (1) tracing an IMF line moving in the solar wind and integrating the electric field from the undisturbed solar wind far away from the magnetopause to a point nearby the magnetopause; (2) integrating the radial electric field from the inner boundary of the MHD model (usually at $3R_e$) to the magnetopause and adding the potential at 3 L-shell, which is assumed to be equivalent to the ionospheric potential at the foot point of the magnetic field line at 3 L-shell; (3) integrating the parallel electric field along the outermost closed magnetic field from the equatorial plane to the foot of the field line in the ionosphere and adding the electric potential at the foot point. In this study, method (2) will be utilized to calculate the electric potential. Under purely southward IMF conditions, the potential along the merging line displays a sine-shape profile with the extrema approximately on the dawn and dusk magnetopause with an offset of 2° (*Hu et al.* (2009)). Therefore, calculating the electric potential along the entire merging line is not necessary, instead, knowing the electric potentials on the dawn and dusk magnetopause is sufficient to obtain the global reconnection rate (i.e., the difference between the two extrema), significantly simplifying the calculation due to the numerical effort that would be needed in searching the merging lines.

To obtain the electric potentials on the dawn/dusk magnetopause Φ_d, the electric field determined by $-\mathbf{V} \times \mathbf{B}$ is integrated radially from the inner boundary ($3R_e$) to

the dawn/dusk magnetopause boundary on the equatorial plane:

$$\Phi_d = \Phi_0 + \int_{3R_e}^{d.m.p.} \mathbf{E} \cdot \mathbf{dr} \tag{6.3}$$

where Φ_0 represents the potential at the foot point of the 3 L-shell magnetic field line on the dawn/dusk ionosphere, assuming the magnetic field line is a perfect conductor and there is no potential drop along this line. The ionospheric potential Φ_0 is generally small compared with the magnetopause potential due to the low-latitude location of the foot point of the 3 L-shell magnetic field line.

This electric potential drop along the merging line (or, the potential difference between the dusk and dawn potentials as simplified in this study) is almost equal to the rate of the change of the magnetic flux reconnected through the magnetopause boundary. The proof is as follows: Assuming the reconnection system has reaches a steady state or varies very slowly and the electric field is electrostatic, that is, $\mathbf{E} = -\Delta\Phi$, the potential drop along the merging line on the equatorial plane from dawn to dusk across the subsolar point) is then

$$\Delta\Phi = \int \mathbf{E} \cdot \mathbf{dl}. \tag{6.4}$$

After applying $\mathbf{E} = -\mathbf{v} \times \mathbf{B}$ (the resistivity term is negligible compared to the convection term according to *Hu et al.* (2009)) to Equation 6.4, it becomes

$$
\begin{aligned}
\Delta\Phi &= -\int (\mathbf{v} \times \mathbf{B}) \cdot \mathbf{dl} \\
&= \int \mathbf{B} \cdot (\mathbf{v} \times \mathbf{dl}) \\
&= \int \mathbf{B} \cdot (\mathbf{v}dt \times \mathbf{dl})/dt \\
&= \int \mathbf{B} \cdot \mathbf{dS}/dt \\
&\approx \frac{d\Phi_b}{dt}
\end{aligned}
\tag{6.5}
$$

where $\Phi_b = \int \mathbf{B} \cdot \mathbf{dS}$ is the magnetic flux flowing (reconnected) through boundary.

Figure 6.8 (bottom) shows the global reconnection rate for Simulation A (solid line) and B (dashed line). The global reconnection rate of Simulation A is significantly reduced after the outflow at 03:00, reaching a minimum value at 04:30, and recovering after two and a half hours, while the rate shows little change in Simulation B, although it is somewhat decreased. As proven above, the electric potential drop along the merging line (or global reconnection rate) is equivalent to the magnetic flux change rate (i.e., within unit time, the net magnetic flux reconnected and eliminated through the magnetopause boundary). Therefre, a smaller potential drop Φ_d (or global reconnection rate) means that in unit time less net magnetic flux is reconnected through the dayside magnetopause boundary, and that less magnetic energy is converted into plasma kinetic energy that transmits down into the ionosphere. This decreased amount of transmitted energy into the ionosphere has already been reflected in the decreased CPCP index earlier (see Figure 6.5 top panel).

For Simulation A, the smaller reconnected magnetic flux is associated with two factors, which have already been discussed: (a) the magnetic field inside the magnetopause is attenuated due to the growth of the ring current and tail current, and (b) the magnetosphere is smaller as the dayside magnetopause moves inwards while

the dawn/dusk magnetopause generally stays still, leading to a smaller reconnection area or separatrix line. After 4:30 when the magnetopause returns sunward, and the magnetic field inside the magnetopause remains at a nearly constant value, the reconnection rate starts to recover.

On the contrary, no evidence of motion of the magnetopause or decrease in the magnetic field are observed in simulation B, indicating that the total magnetic flux reconnected on the dayside magnetopause boundary should change little, i.e., the global reconnection rate should change little, which is exactly the situation shown in the Figure 6.8.

6.2.2.3 On the energization of heavy ions

One foundamental but important question associated with the energization of O^+ inside the magnetosphere is: Is the storm-enhanced O^+ energy density (1) a result of the direct ejection of enegetic plasma out of the ionosphere (*Sheldon et al.* (1998)) or (3) a result of capture of in-flight/in-transit O^+ in the lobe region (*Peterson et al.* (2009)) or (3) a result of localized energization of pre-existing O^+ in the plasma sheet (*Delcourt* (2002), *Nosé et al.* (2000a), *Fok et al.* (2006))? *Sheldon et al.* (1998) suggested that the acceleration process of the energetic oxygen beams inside the plasmasheet is associated with in-situ parallel electric fields along the magnetic field lines conneting to the ionosphere, from where the ionospheric heavy ions are injected out and into the inner magnetosphere. In contrast to this direct injection of new O^+ out of the ionosphere into the inner magnetosphere, other studies ascrib to a localized energization in the plasma sheet. *Fok et al.* (2006) simulated an idealized substorm by using LFM MHD model to study the cause of prompt enhancement of substorm-associated O^+ in the plasma sheet, and they concluded that the pressure peak is a result of nonadiabatic energization of the pre-existing O^+ in the plasma sheet while dipolarization takes place. *Delcourt* (2002) suggested that the O^+ orignating from

the ionosphere is accelerated by inductive electric field in the inner magnetosphere while being injected earthward. *Nosé et al.* (2000b) supported the scenaria through observations that the O^+ enhancement is caused by local magnetic field reconfiguration (local dipolarization) in the near-Earth plasma sheet region. A third proposal for the enhanced O^+ energy density is through the tail reconnection which captures the ions in the lobes and accelerates them. *Peterson et al.* (2009) analyzed the relative magnitude of the O^+ population in transit between the ionosphere and the ring current in quiet time before geomagnetic storms and suggested that the dynamics during the storm alters the O^+ pathways from the ionosphere to the ring current, and that the preexisting in-transit O^+ population is captured by the magnetic field into the ring current during the storm time. *Peroomian et al.* (2006) simulated dayside O^+ outflow with test particle tracing and found that the O^+ number density and energy density in the plasma sheet and ring current respond instantenously to an interplanetary shock. They suggested that the rapid enhancement is caused by the acceleration of the "in-flight" ions that were already in the lobes. *Kistler et al.* (2010) also suggested the enhanced earthward convection after substorm brings the heated plasma into the plasma sheet and ring current.

Fok et al. (2006) argued that the ionospheric cusp-origin ions with energy less than keV would take hours to arrive at the plasma sheet and to reach energy greater than keV, and thus could not explain the prompt increase in the energy density. Therefore, they disputed the idea that the new energetic plasma out of the ionosphere is responsible for the increased energy density in the plasma sheet, as suggested by *Sheldon et al.* (1998). In Simulation A, the specified outflow in an energy of 100 eV (0.1 keV), however, spends less than an hour to reach to the near-Earth plasma sheet, less than that claimed by *Fok et al.* (2006); In Simulation B, the ionospheric heavy ions leak into the inner magnetospere along the magnetic field lines in minutes. Even though a quick feed of ionospheric plasma is satisfied, there is still lack of evidence

that this quick feed to the plasma sheet is the reason of intensified energy density in the inner magnetosphere because the simulation results indicate that the direct outflow from the curoral one does not gain sufficient energy as needed.
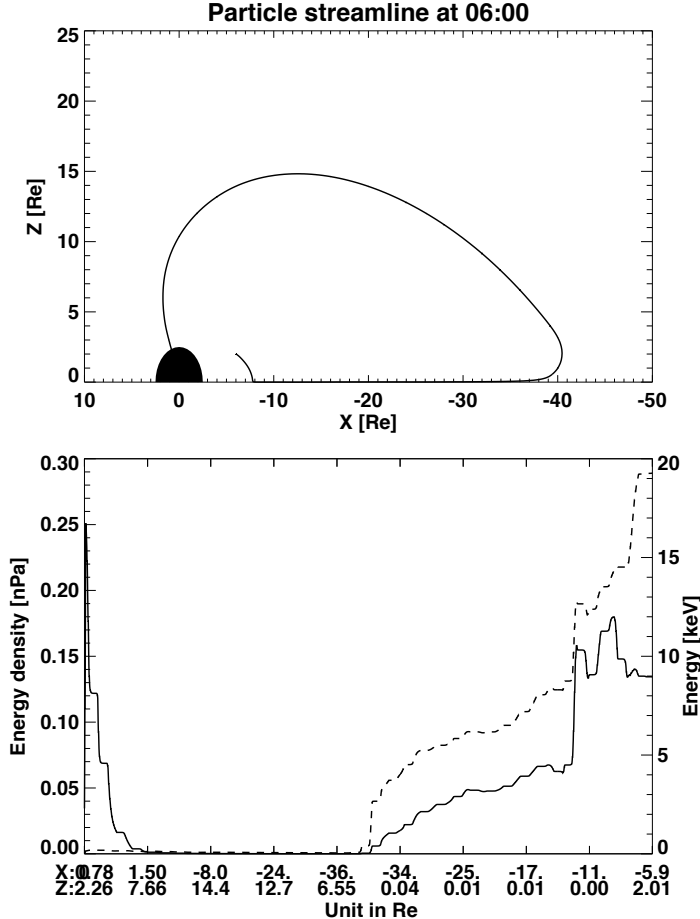
Figure 6.11: The energy density (solid, left label) and particle energy (dashed, right label) along a streamline (top panel) of ionospheric cusp heavy ions. The bottom labels indicate the position in the X-Z magnetosphere. The streamline is extracted at the end of Simulation A (at 06:00).

In contrast to Simulation B that demonstrates a quiet magnetotail even though the near-Earth plasma sheet is continuously fed by the ionospheric heavy ions, Simulation A shows a dynamic tail. The tail is dramatically disturbed about 1 hours after the outflow begins, adiabatically heating the particles ejected from the tail reconnection region and towards the Earth across the magnetic field lines. Figure 6.11 illustrates the energy density (solid) and particle energy (dashed) along a stream-
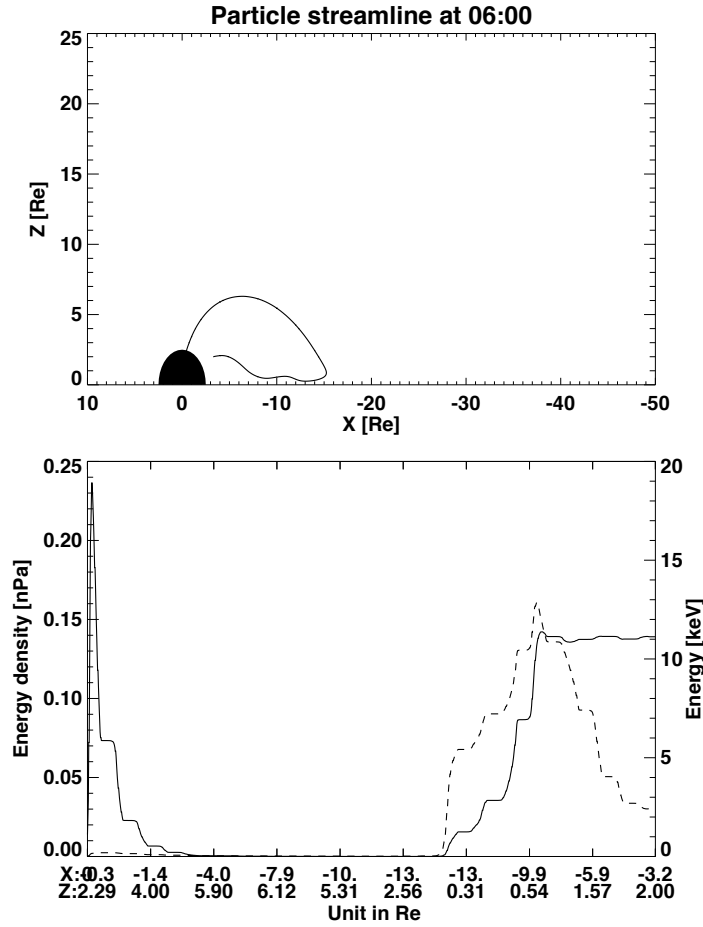
Figure 6.12: The same format as in Figure 6.11, but this is from Simulation B (night side auroral outflow).

line of heavy ions out of the ionospheric source location and back to the night side. This streamline only considers the O^+ convection in the X-Z plane, therefore the azimuthal transport of the ions is omitted. The energy density (solid) of heavy ions near the cusp region is high because of the high number density, but the particle energy (dashed) is small. During the flight in the magnetosphere from the high-altitude cusp magnetosphere through the lobes until captured by the tail reconnection, the energy is very small. The ions basically move with the solar wind convection and experience little energization. Following the tail reconnection, the adiabatic heating of the heavy ions is clearly seen tailward of (-34, 0.04) Re, when the particle energy and energy density ramp up after the heavy ions migrate through the tail reconnec-

tion site near the equatorial plane and are ejected towards the Earth. However, the adiabatic heating along the earthward convection does not fully account for the ring current energization, as the energy density is significantly enhanced by 130% near the outer boundary of the ring current (i.e., around -13 Re), partly due to the braking effect and hence the accumulation of large amount of particles near that boundary. As for a single particle, the energy also abruptly increases from 9 keV to 13 keV, and continuely grows while moving along the closed magnetic field to the inner magnetosphere. Compared to the above three major suggestions regarding the energization of the ionospheric heavy ions along their pathway from the source region to the inner magnetosphere plasma sheet, simulation results presented here favor both the second and third arguments, that is, in addition to the energization provided by the tail reconnection which captures ions in the lobes and produces hot ions adiabatically towards the Earth, localized nonadiabatic heating is also seen when the particles are braked near the outer boundary of the ring current, or the "wall" region called by *Ashour-Abdalla et al.* (2009).

As the ionospheric ions from the night side auroral region directly leak into the inner magnetosphere along magnetic field lines quickly, without experiencing the tail reconnection, there is no adibatic heating which occurs to the bursty flow from the tail. Figure 6.12 illustrates the energization along a flow line for Simulation B. The energization of the heavy ions mostly happens in the middle plasma sheet within 6-14 Re, reaching an energy as high as 13 keV near 10 Re, and the temperature cools down when the ions move closer to the Earth. The energy density is however constantly high because of large number density accumlated in the inner magnetosphere. This simulation suggests that the the heavy ions are energized locally.

6.2.2.4 On the role in the substorm initialization

One debate within the magnetospheric community regarding the role of the iono-spheric heavy ions in the magnetosphere involves substorm development. The role of heavy ions in substorms was first proposed by *Baker et al.* (1982) who suggested that the O^+ increases the growth rate of the linear ion tearing mode instability, thereby leading to a fast initialization of substorms. *Kistler et al.* (2006) could not find the expected role of O^+ in decreasing the threshold of substorm onset and suggested that a triggering mechanism other than the ion tearing mode instability at the reconnection site might be responsible for substorm onset. *Lennartsson et al.* (1993) suggested that O^+ ions do not have geomagnetic feedback in the magnetotail after they studied the correlations between the averaged O^+ abundance and geomagnetic indices. *Nosé et al.* (2009a) found negative correlation or no correlation between the long-term plasma sheet ion composition and substorm occurrence, so they suggested that the O^+ ions in the plasma sheet may prevent occurrence of substorms, in contrast with the O^+ triggering substorm model. While the last two studies both utilized long-time averaged quantities of O^+ observations to examine the geomagnetic feedback of O^+ ions, *Daglis and Sarris* (1998) disputed the feasibility of using averaged quantities by raising the question of temporal scale. They argued that as a substorm is triggered in a shorter time scale, the long-term averaged quantities could not reflect the transient participation of the heavy ions in the substorm so that the possible crucial roles of O^+ in the substorm should not be excluded.

Nosé et al. (2009a) concluded that the O^+ ions may prevent substorms from occurring by referring to an earlier study that showed a decreased magnetotail reconnection rate/downstream speed (*Shay and Swisdak* (2004)) with the presence of O^+ in the tail. Their statements implied that a smaller reconnection rate/downstream outflow speed is equivalent to a decreased possibility for substorms to occur. The problem is that these are two different, albeit relate, concepts: the reconnection rate indicates

how fast magnetic flux in the lobes is eroded, while the possibility of the occurrence is related to whether or not the substorm onset threshold is met. Both simulations in this study show reduced tail reconnection rate after the mass loading in the magneto-tail region by both applying the Cassak-Shay formula (Equation 6.2), and examining the downstream speed out of the reconnection site. The magnetotail in the two simulations, however, behave differently. A detailed examination of the magnetic field and mass density near the reconnection site reveals that the reduction of the reconnection rate is not simply related to increased mass density that slows down the downstream speed (or reconnection rate). Indeed, the magnetic field around the reconnection site is largely enhanced in Simulation B, meaning that more magnetic flux is actually reconnected through the X-line assuming the diffusion region does not change significantly. The enhancement in the magnetic field also appears in the first post-outflow 45 minutes in Simulation A before the drastic stretching of the tail. Such increase in the magnetic field shown in both simulations is evidently from the compression of the neutral sheet by the mass loading upon it.

During these time periods when magnetic energy is accumulated and stored in the tail (i.e., the growth phase if a substorm is going to occur), the tail responds dramatically differently in the two simulations. After outflow starts, Simulation B shows a constant steady tail with little to no change in the tail length throughout the entire simulation time, implying that the mass loading in the tail has little influence in initializing substorm onset, even though a growing amount of magnetic flux is advected into the reconnection region. In this sense, the ionospheric mass loading plays a negative role in magnetotail stability. In other words, the ionospheric O^+ ions in the tail operate as an obstacle to prevent or postpone the substorm onset as opposed to the increased incoming magnetic energy which is supposed to facilitate the substorm.

However, Simulation A shows a huge extension of the tail after a small stretching

of the tail during the first 45 minutes. After this time, the near-Earth reconnection site appears to abruptly disappear, with a new reconnection site appearing around 40 R_e down tail. A subsequent, smaller reconfiguration of the tail is also observed around 04:30, which is accompanied with enhancements in the ionospheric Joule heating and in both the energy density of O^+ ions and number density ratio of O^+/H^+ in the earthward plasma sheet. These responses indicate that the heavy ions loading in the tail helps trigger the reconfigurations by first loading the mass source on to the plasmasheet, compressing the neutral sheet, accumulating magnetic energy in the tail and then disrupting the tail followed by another disruption.

The different behavior of the tail in these two simulations strongly disagrees with previous assertions about the role of ionospheric heavy ions in the tail stability. The heavy ions appear not to play a definitive role in substorms occurrence by disrupting the tail or to play a definitive role in preventing the substorms. From the simulation study shown here, the influence of O^+ ions on the tail is actually bound up with the origin of the ions and their corresponding pathways. A cusp-origin ionospheric outflow lands near the tail reconnection region from the lobes outside the neutral sheet and disturbs the magnetotail dramatically, while the nightside aurora-origin outflow plasma populates the near-Earth plasma sheet, preventing the release of the accumulated magnetic energy and the development of the substorm. Therefore, verifying the origination of the heavy ions before confirming their role in the substorm development is necessary, rather than drawing an absolute conclusion. In actuality, it may not be the starting point only, but the starting point plus the ratio of the parallel and perpendicular velocities at the source, since this ratio determines where in the magnetosphere the O^+ will be deposited.

It should be noted that the above conclusion about the origin-dependent role on the tail stability could also be controlled by initial and boundary conditions specified for the simulations. For example, one highly possible parameter is the outflow veloc-

ity. A different outflow velocity near the Earth certainly results in different landing location with respect to the tail reconnection, feeding mass source to a different position of the tail. In this case, the tail dyanmics may demonstrate a different scenario than in current simualtions. In other words, whether the tail stability is indeed associated with the source region of ionospheric outflow requires future study, by variously altering the boundary conditions for the outflow.

6.3   Influence of outflow intensity

During storm times, the heavy ions have been found to be a significant plasma source of the plasma sheet and ring current, with the density and energy in the plasma sheet highly dependent on the source intensity from the ionosphere. Here, the influence of the outflow O^+ density on the energization of the inner magnetosphere as well as the feedback on the solar wind-magnetosphere interaction is examined. Study of the influence of other properties such as velocity or temperature of the upwelling O^+ will be carried out in the future.

6.3.1   Methodology

In order to investigate the influence of the ionospheric outflow intensity on the inner magnetospheric dynamics, an inner magnetospheric model (i.e., the Rice Convection Model or RCM) is utilized within the coupled framework, as introduced in Chapter II. A uniform ionospheric outflow is specified over both southern and northern polar caps (above $60°$ magnetic latitude) on the inner boundary of the MHD model. The parameters for the upwelling ions are constant: $V_{O^+||} = 20\ km/s$, $T_{O^+} = 1000,000$ K, $N_{H^+} = 20\ cm^{-3}$, $V_{H^+||} = 2\ km/s$, and $T_{H^+} = 100,000\ K$. Two simulations are performed with different O^+ densities: one models an ionospheric outflow event with $N_{O^+} = 20\ cm^{-3}$, and the other one has $N_{O^+} = 40\ cm^{-3}$. Both outflow rates are initialized at the beginning of the simulation.

6.3.2 Simulation results

6.3.2.1 Contribution to inner magnetosphere energization

In this section, the effect of the heavy ions on the inner magnetosphere is investigated. Using a multi-fluid MHD code, one can examine the behavior of individual fluids and their individual contributions within the global magnetosphere. The D_{st} index, a proxy of ring current intensity, is one of the important indices that are commonly used to analyze the energization within the magnetosphere. The D_{st} index (i.e., the magnetic field perturbation at the center of the Earth) from MHD simulations can be computed by taking the Biot-Savart integral over current sources throughout the global magnetosphere. While the current sources from the MHD model are an integrated result of all ions and electrons, incapable of distinguishing between different ion species, an alternative to study the contributions of ion components to the D_{st} index is the Dessler-Parker-Sckopke relation (DPS) (*Dessler and Parker* (1959); *Sckopke* (1966)), which linearly relates the D_{st} index with the energy content E_{RC} of the ring current:

$$\Delta B[nT] = -B_E \frac{2E_{RC}}{3U_E} = -3.98 \times 10^{-29} E_{RC}[keV] \qquad (6.6)$$

where, B_E is the equatorial surface magnetic field strength of the Earth's dipole and U_E is the magnetic energy of the dipole field beyond the Earth surface. This ΔB is often treated as equivalent to the Dst^* index, the Dst index with the effect from magnetopause current being eliminated.

The total energy content of the ring current is represented by the total particle energy within the closed field-line region determined by a ray tracing technique (*DeZeeuw et al.* (2004)) in the MHD code. The region excludes the near-Earth region by excluding dipole latitude below 50°, which corresponds to an L-shell of 2.4. As the energy content for an individual ion component can be resolved in the MHD code, the

Dst^* index thereby can be distributed between O^+ and H^+ ions and be referred to as $Dst^*(O^+)$ and $Dst^*(H^+)$ respectively (Figure 6.13). In the simulation with $20cm^{-3}$ O^+ outflow density (left panel), the O^+ energy contribution to the ring current keeps increasing while $Dst^*(H^+)$ starts to decrease two hours after the outflow. Consequently, the increase of the ring current is slow even though the $Dst^*(O^+)$ continues to intensify up to -9 nT at the end of the simulation (at 4:00). In the simulation with $40\ cm^{-3}$ outflow density (right panel), the $Dst^*(O^+)$ shows a faster energization, resulting in a stronger ring current. Note that the H^+ source in the ring current continues to intensify, but at a smaller growth rate than that of the O^+ ions. These differences in the two simulations imply that a larger outflow fluence of heavy ions out of the ionosphere provides more energy to the ring current. The larger energization rate of the H^+ and the total ring current in the second simulation may result from more stretching of the magnetotail that adiabatically heats up the plasma towards the Earth more intensely.

(a) $20\ cm^{-3}$ (b) $40\ cm^{-3}$
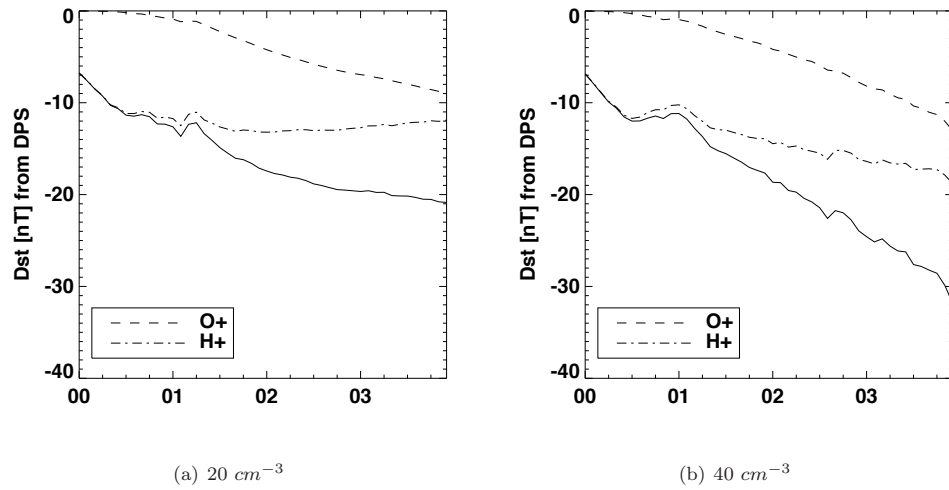
Figure 6.13: Dst^* index (solid) calculated from the DPS relation (Equation 6.6. Individual contributions to the Dst^* index from H^+ and O^+ ions within the closed field-line region are shown by dash-dot and dashed lines respectively for simulations with an outflow density of $20\ cm^{-3}$ (left panel) and $40\ cm^{-3}$ (right panel).

6.3.2.2 On the Kelvin-Helmholtz Instability

The outflow with 40 cm^{-3} O^+ density provides significant feedback to the solar wind-magnetosphere interaction by significantly disturbing the magnetosphere, whereas the simulation with a smaller outflow density produces a quiet and steady magnetosphere. This section will explore the details in the simulation with an outflow density of 40 cm^{-3}.
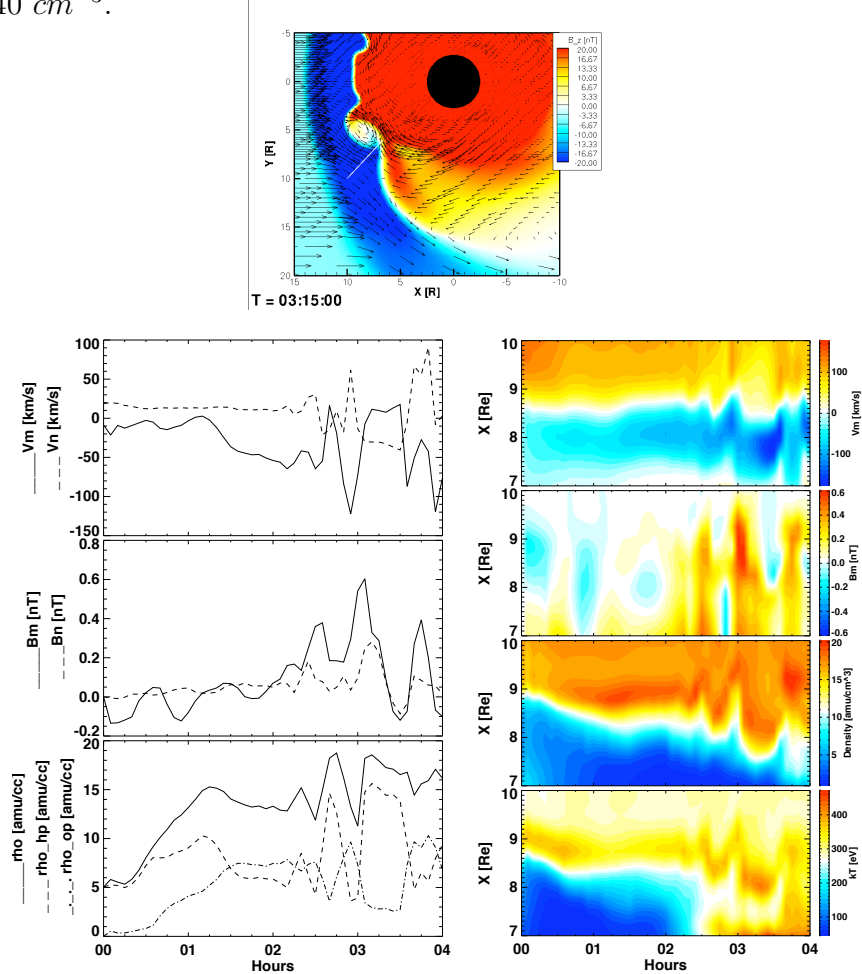
Figure 6.14: Top panel: the Z component magnetic field in the equation plane for the dusk side at time 03:15UT. Bottom left panel: The velocity (top) and magnetic field (middle) in their M and N directions with respect to the magnetopause on the magnetospheric side at $(8.5, 8, 0)$ R_e. The bottom plot shows H^+, O^+ and total mass densities at the same location. Bottom right panel: Contour plots of shear velocity, magnetic field, total mass density, and energy density along a path (white line on the top panel) across the magnetopause on the equatorial plane as a function of time.

Figure 6.14 (top) shows color contours of the magnetic field Z component in the

equatorial plane of the dusk magnetosphere at time 03:15UT. The dayside magnetopause is disturbed as a vortex propagates along the magnetopause, mixing two plasma sources from the magnetosheath and magnetosphere. The lower left panel illustrates the temporal evolution of the velocity, magnetic field, and density at (8.5, 8, 0) R_e near the magnetopause, resembling measurements from a stationary satellite. The velocity and magnetic field vectors are in a local LMN coordinate system, where **N** points in the normal direction of the magnetopause on the equatorial plane, **M** directs to the dawn along the magnetopause surface, and **L** completes the third axis in orthogonal system (i.e., the **Z** direction out of the equatorial plane towards the north). The plasma velocity is mainly in the M direction, i.e., along the magnetopause; the magnetic field in both **M** and **N** directions are small since the dominant component is in **Z** direction; the total mass density contains H^+ and O^+ and is significantly enhanced after the arrival of the O^+ convected from the night side. About two hours after the outflow occurs, the virtual stationary satellite observes periodic variations in all these parameters, implying that the magnetopause is oscillating around where the virtual satellite is located.

A clearer demonstration of these variations is shown in Figure 6.14 (bottom right panel), which shows 2D contour plots of plasma shear velocity, parallel magnetic field, density and energy along a line cut from (7,6,0) to (10,10,0) R_e across the dusk equatorial magnetopause as a function of time. The magnetosheath is on top of the magnetosphere in each of the plots. During the simulation, the magnetosheath plasma with smaller magnetic field, larger density, and hotter particles intrudes into the magnetosphere at least four times with an approximate period of 0.5 hours. The penetration of plasma into the other side is as large as 2 R_e, mixing the plasma from the two domains.

This mixing of the magnetosheath and magnetosphere plasma stems from the Kelvin-Helmholtz instability (KHI), which appears with the presence of large relative

shear velocities and is often observed on the flank magnetopause where the solar wind speed on the magnetosheath side is sufficiently different from the convection inside the magnetosphere. The KHI is an important magnetospheric physical process because it plays a role in transporting solar wind mass and energy into the magnetosphere by mixing the plasma from two different regions. This interaction is therefore considered as the second most important solar wind-magnetosphere coupling process other than magnetic reconnection. Theoretically, the KHI grows when the shear flow is larger than a certain threshold according to a linear inequality (*Hasegawa* (1975); *Gratton et al.* (2004)):

$$(\mathbf{V} \cdot \mathbf{k})^2 \geq \frac{\rho_1 + \rho_2}{\mu_0 \rho_1 \rho_2}[(\mathbf{B}_1 \cdot \mathbf{k})^2 + (\mathbf{B}_2 \cdot \mathbf{k})^2] \tag{6.7}$$

where $\mathbf{k}$ is the wave vector. $\mathbf{V}$, $\mathbf{B}$, and ρ denote the velocity difference of two plasmas, magnetic field and mass density respectively. The indices "1" and "2" represent the corresponding values in the magnetosphere and magnetosheath respectively. Here, the velocity and magnetic field vectors contain the directions along the magnetopause towards dawn side ($\mathbf{M}$ direction), $\mathbf{Z}$ direction, and the normal of the magnetopause ($\mathbf{N}$ direction). Assuming that the field component in the $\mathbf{N}$ direction is negligible and that the angle between the wave propagation $\mathbf{k}$ and $\mathbf{M}$ direction is θ, the above inequality becomes

$$[(V_{m1} - V_{m2})cos\theta + (V_{z1} - V_{z2})sin\theta]^2$$
$$\geq \frac{\rho_1 + \rho_2}{\mu \rho_1 \rho_2}[(B_{m1}cos\theta + B_{z1}sin\theta)^2 + (B_{m2}cos\theta + B_{z2}sin\theta)^2]. \tag{6.8}$$

If the wave propagates vertically (i.e., in $\mathbf{Z}$ direction, $\theta = 90°$), it is suppressed quickly by the Z component of the magnetospheric field which is very large and provides an effective surface tension that has stabilizing effect on the wave along the same direction. If the wave propagates along the equatorial magnetopause (θ is zero), then

the above equation becomes:

$$(V_1 - V_2)^2 \geq \frac{B_1^2 + B_2^2}{\mu \rho_2}(1 + \frac{\rho_2}{\rho_1}) \tag{6.9}$$

where the magnetic field and velocity are both in the **M** direction.
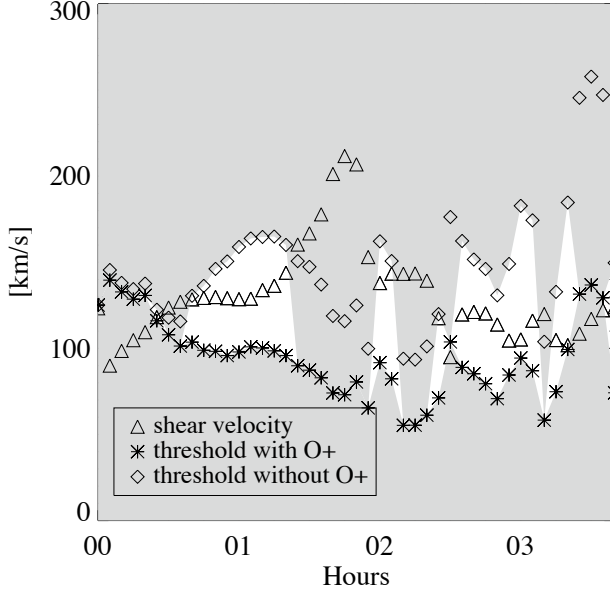
Figure 6.15: The shear velocity and the threshold of Kelvin-Helmholtz instability across the magnetopause boundary on the line of (7,6,0) to (10,10,0) R_e as a function of simulation time: the shear velocity ($\triangle$); the threshold computed from Equation 6.9 right hand side when O^+) is included in the mass density ($\star$) and when no O^+ is included. The unshaded region represents period when the instability is triggered only if the heavy ions are included.

Using this simplified formula, the theoretical prediction of the onset of the KHI near the dusk magnetopause is examined. The parameter values for Equation 6.9 are chosen from the same extracted line across the equatorial magnetopause, at locations 1 Re away from the magnetopause (where the shear velocities change signs) on both sides. The threshold (i.e., the right hand side of Equation 6.9) is computed with the density ρ either including O^+ or excluding O^+ and is then compared to the shear velocity as illustrated in Figure 6.15. The symbols "$\triangle$", "$\diamond$", and "$\star$" represent the shear velocity $|V_1 - V_2|$, the threshold with $\rho = \rho_{H^+}$ and threshold with $\rho = \rho_{H^+} + \rho_{O^+}$,

respectively. Initially when few O^+ ions arrive at the magnetopause, the thresholds with O^+ and without O^+ are almost the same, and the shear velocity is well below the threshold, resulting in a stable magnetosphere. When O^+ begins to arrive at the magnetopause, the threshold with both ion components is significantly decreased to be smaller than 100 km/s (see "⋆" line), while the threshold excluding O^+ ions is much greater, leaving the shear velocity ("△") in the middle of the two during most of the simulation. In other words, the shear velocity ("△") is larger than the threshold with O^+ ion ("⋆") (the unshaded region) and smaller than that without O^+ ("◇"), indicating that the presence of O^+ prominently increases the possibility of the KHI onset near the flank/magnetopause by lowering the threshold of the instability onset. This is consistent with observational study by *Bouhram et al.* (2005) who showed that with a sufficiently large amount of heavy ions in the magnetosphere, the KHI is more likely to occur.

Note that the theoretical prediction of the onset of the KHI takes place about 0.5 hour after the outflow initiates, different than the simulation results that do not show disturbances on the magnetopause until about 2 hours after the outflow. Such discrepancy may be associated with the way the parameters on both sides of the magnetopause are chosen to verify the stability of the boundary. In other words, taking parameters 1 R_e away from the magnetopause probably introduces some uncertainties, as the magnetopause boundary may frequently change in its thickness. Another possible factor for this discrepancy is that the numerical viscosity on the boundary inhibits or delays the onset of the KH instability in the simulation, while the theoretical criteror shown by Equation 6.9 is linear and does not take into account other factors in the fluids besides the magnetic field and mass density.

This discrepancy could also root in the criterion we have chosen. In other words, Equation 6.9 simply represents the circumstance when the waves propagate parallel to the equatorial plane; but in fact, the waves could travel in all directions on the

magnetopause surface. Therefore, adopting Equation 6.8 might reveal more details. As the criterion is wave direction (θ) dependent, Figure 6.16 illustrates the contour of the difference between the left and right hand sides of Equation 6.8 as a function of wave direction. When the wave propagates with a larger angle θ with respect to the equatorial plane, the magnetosphere is more stable (blue) because of the larger magnetic field Z component that plays an increasingly effective part of stabilizing the surface waves. With an angle closer to the equatorial plane, the Kelvin-Helmholtz instability can grow more easily (yellow) as the magnetic field component in the equatorial plane is too small to stabilize the waves. If the wave propagates with an angle of 10° with respect to the equatorial plane, the predicted growth of KH waves will not occur until 01:30, significantly later than the time predicted from Equation 6.9 or Figure 6.15. Again, the plots indicate that the growth of the instability is more efficient with the participation of the heavy ions O^+. For instance, the instability can be triggered even with a wave propagation angle as large as 35°, while only during occasional intervals can the instability occur when the heavy ions are absent and the largest possible angle for a surface wave to propagate is 15°, as indicated in the bottom panel.

The newly developed KH surface waves on the magnetopause, triggered by a large mass loading from the ionosphere, in turn place feedback onto the ionospheric electrodynamics. Although the dayside reconnection rate is suppressed by the increased amount of heavy ions in the magnetosphere, the Kelvin-Helmholtz instability, allows more solar wind energy to transport through the magnetopause boundary (*Pegoraro et al.* (2008); *Hasegawa et al.* (2004)), conversely increasing the reconnection rate through the rolled-up vortices (as shown in Figure 6.14, top panel). The consequence of this can be observed in the cross polar cap potential (CPCP) index as shown in Figure 6.17. The ionospheric heavy ions in the magnetosphere significantly reduce the CPCP index as soon as the outflow is initialized. After two hours, while the CPCP
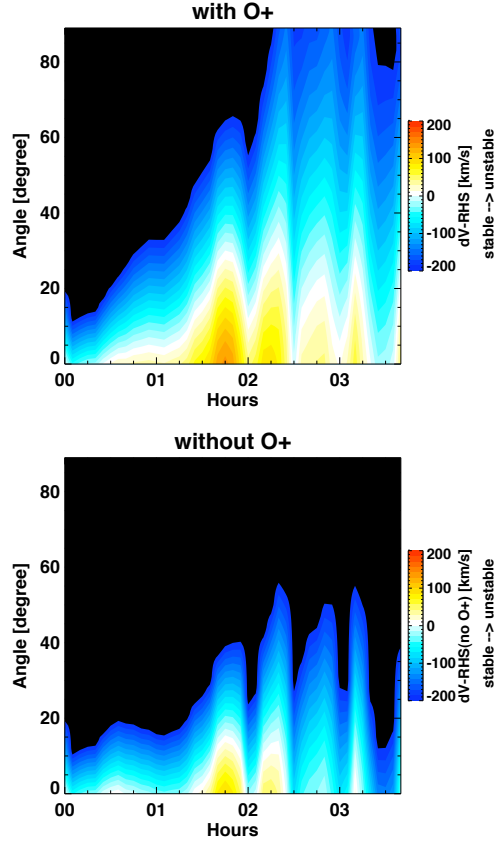
Figure 6.16: Contour of the difference between the left and right hand sides of Equation 6.8 with angles range from 0 to 90° (i.e., parallel to perpendicular propagation of the waves with respect to the equatorial magnetopause). Yellow indicates the magnetosphere is unstable while blue means the system is stable.

index in the simulation with 20 cm^{-3} outflow density maintains nearly a constant level, the CPCP index in the other simulation that develops the KH waves shows an increasing trend, indicating that more energy is transmitted down to the ionosphere. This is ascribed to the KH surface waves that allow more solar wind energy to enter the magnetosphere. The bulge between 01:00 and 02:00 in both simulations is probably associated with a reconfiguration of the tail, after a large amount of heavy mass source loading of the tail plasmasheet.

So far, this feedback ultimately completes the solar wind-magnetosphere-ionosphere coupling circulation: the ionospheric mass outflow into the magnetosphere alters the magnetospheric dynamics as well as solar wind-magnetosphere interaction

by triggering the KH surface waves, which allow more solar wind energy into the magnetosphere and further influence the ionospheric electrodynamics, thus changing the ionospheric mass outflow, the first driver in this circulation.
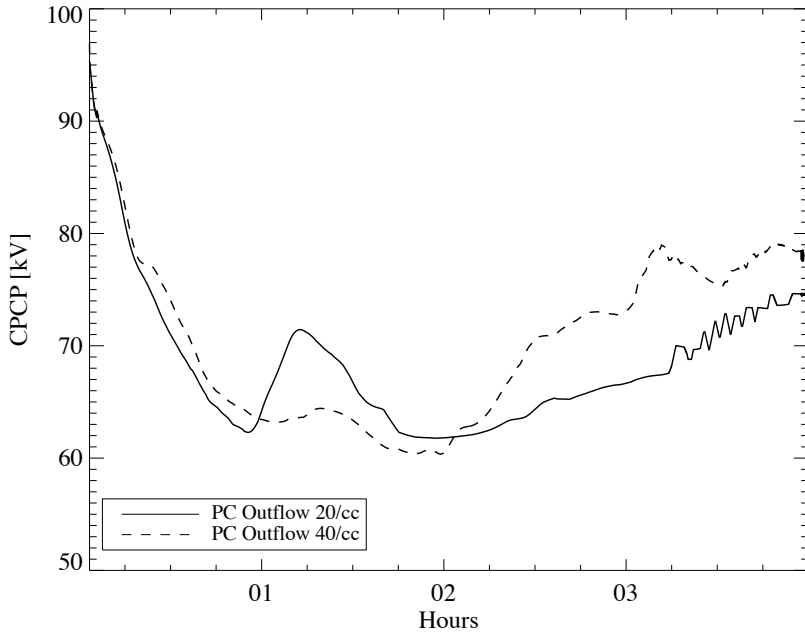
Figure 6.17: The cross polar cap potential index for two simulations with outflow density of 20 cm^{-3} (solid) and 40 cm^{-3} (dashed) respectively.

6.4   Conclusion

Ionospheric outflow into the magnetosphere contributes an inertial interaction to the geospace system. How the ionospheric heavy ions loading into the magnetosphere change the magnetospheric dynamics or even the solar wind-magnetosphere interaction is of great importance. In this study, three types of ionospheric outflow simulations have been carried out: dayside cusp O^+ outflow, night side auroral O^+ outflow, and O^+ outflow from the entire polar cap region. From the first two simulations that aim to examine the influence of the outflow origin on magnetospheric dynamics, we have found the following results:

1. Different from claims from many two-dimensional idealized multi-ions simulations regarding the role of heavy ions in reconnection, (i.e., the heavy ions increase the mass density near the reconnection site, reducing the Alfvén wave speed, and therefore decreasing the reconnection rate), the presence of heavy ions in the magnetosphere do not simply act in the same way. Instead, the heavy ions originating from the ionosphere can largely alter the global state and topology of the magnetosphere by changing the strength of magnetic fields, states of other ion species, and even the size of the magnetosphere. The combination of above complicated dynamics subsequently leads to a change of the reconnection rate.

2. Ionospheric heavy ions originating from the dayside cusp region can give rise to a dynamic magnetotail and help create energetic particles for the ring current. This is less true for the night side auroral outflow, since the heavy ions directly travel into the near-Earth plasmasheet along the magnetic field lines without flowing through the tail.

3. The subsolar reconnection rate is decreased more when ionospheric heavy ions travel out from the dayside cusp region compared to when the magnetospheric heavy ions travel out from the nightside aurora. The more profound depression is associated with two factors: the attenuation of the magnetospheric field and the increase in the mass density near the subsolar magnetopause.

4. The global reconnection rate is also depressed more in the cusp outflow case, as the magnetopause moves inward due to the attenuated magnetospheric field, which is caused by the growth of the ring current and stronger tail current. While no changes in the magnetospheric field or magnetopause position are observed in the nightside outflow simulation, the global reconnection rate undergoes a minor decrease.

5. The difference regarding the tail dynamics in these two simulations probably shed some light on the argument about the role of heavy ions playing in the tail stability. The role of heavy ions may have an origin dependence such that cusp-origin heavy ions may facilitate substorms while aurora-origin heavy ions probably hinder substorms, or may not play a role in their occurrence.

The outflow simulation from the entire polar cap region has been used to examine the influence of outflow intensity on the magnetospheric dynamics. By using different outflow densities, we have discovered the following results:

1. The outflow with larger intensity significantly disturbs the global magnetosphere by triggering Kelvin-Helmholtz waves along the magnetopause boundary, which in turn modifies the solar wind-magnetosphere interaction by increasing the reconnection rate through the roll-up of Kelvin-Helmholtz vortices.

2. The greater outflow density, as expected, results in a stronger ring current. However, the O^+ ions do not indicate large differences in terms of their own contribution to the intensity of ring current. In contrast, the H^+ ions in these two simulations show different energization: the larger the heavy ions outflow density is, the more energization the H^+ ions obtain. This may be associated with the magnetotail stretching that provides more adiabatic heating to the earthward moving plasma., as the tail is longer with a larger outflow rate that places more pressure on the neutral sheet.

CHAPTER VII

Summary and conclusion

To summarize, this dissertation studied the roles of external drivers (solar wind/IMF discontinuities) and internal processes (ionospheric heavy ions outflow) in regulating the terrestrial magnetosphere-ionosphere system. Using the near-Earth coupled modules in the Space Weather Modeling Framework (SWMF), various numerical simulations were performed, which improved the understanding of the solar wind-magnetosphere-ionosphere coupling. The study started from external driving (i.e., solar wind/IMF) impinging on the integrated magnetosphere-ionosphere system by examining time delay in the system with respect to the arrival of a disturbing source at the bow shock and by investigating the generation mechanisms of system responses, the influence of solar wind parameters on the responses, and the evolution of waves within the system. The dissertation then continued to study internal changes within the magnetosphere-ionosphere system: an enrichment of ionospheric heavy ions flowing into the magnetosphere, which is caused by the variations of external driving. The influences of the heavy ion outflow on magnetospheric dynamics and further on the solar wind-magnetosphere coupling were investigated.

7.1 IMF southward turning

One external driver of "space weather" in the terrestrial system is southward turning of the IMF, as southward IMF configurations are favored for large and efficient transport of solar wind energy into the terrestrial system through magnetic reconnection and account for geomagnetic storms as well as substorm. Utilizing the near-Earth modules in the SWMF, simulation results indicate that after the IMF orientation suddenly changes from northward to southward with the solar wind speed remaining at 400 km/s, the ionosphere and ground do not experience disturbances until about 10 minutes later. Such a time delay is attributed to the time needed for several processes in sequence: (1) The propagation of the IMF discontinuity through the bow shock and the magnetosheath; (2) A conversion from a cusp reconnection configuration to a dayside reconnection configuration; (3) The transmission of an Alfvén wave down to the ionosphere through the cusp region, which eventually brings about the turbulence in the ionosphere. Such a time delay demonstrates a solar wind speed dependence: generally, a shorter time delay for the ionosphere to react is associated with a faster solar wind.

7.2 Solar wind density increase

A sudden enhancement of the solar wind density is another external driver of geospace disturbances. A contact discontinuity with a step increase in the solar wind density is simulated by the near-Earth modules in the SWMF, from which a two-phase response is produced in the ionosphere and on the ground. A close investigation of the two-phase response reveals that the two phases are arisen by different generation mechanisms. (a) A dusk-to-dawn inductive electric field (E_y), generated by a fast mode wave launched by the sudden compression of the magnetosphere, is responsible for the first pair of field-aligned currents (FACs) that creates the first phase response

in the ionosphere, denoted as "E_y response". This mechanism is found to be the same under both southward and northward IMF conditions. (b) After the sudden compression, pressure gradients, involved in two high-pressure bulges near the equator propagating around the Earth towards the tail, creates vortices in the magnetosphere which generates the second pair of FACs for the second phase response. This pressure-gradient driven mechanism is only present under northward IMF conditions, as no pressure-gradient driven vortices are observed in the southward IMF case. In the latter case, however, the pre-existing two-cell convection pattern in the magnetosphere is destroyed by the sudden compression, but vortices are then re-built up by large shear flows along the flanks, therefore generating a second pair of FACs as well. Under either southward or northward IMF conditions, the second phase response is denoted as a "Vortex-response".

Statistical analysis of solar wind density increase events from actual observations shows that not all the events appear to possess a two-phase response; rather, some events simply display a single-phase response. While statistical attempt fails to find the parameter for the way the geo-space system responds, a simulation reveals that the two-phase response is always present, but its manifestation on the ground and in the ionosphere becomes too complex to be easily recognized under some circumstances such as when the solar wind Alfvén Mach number is very low.

After the impulsive solar wind dynamic pressure suddenly compresses the magnetosphere, a resultant fast mode wave propagating within the dayside magnetosphere experiences multiple reflections between the dayside magnetopause boundary and the Earth boundary, resulting in multiple Earthward propagations of the inductive dusk-to-dawn electric field and therefore creating two groups of the two-phase response. The multiple Earthward propagations of electric fields produced in the simulation are for the first time supported by THEMIS/EFI measurements.

7.3   Ionospheric heavy ions outflow

As the solar wind and magnetosphere are tightly coupled, any variation in the solar wind or IMF will give rise to changes within the magnetosphere-ionosphere system. The system then need to adjust to the new configuration through internal exchange processes, such as substorms, sawtooth events, etc. One process studied here is the ionospheric heavy ions outflow into the magnetosphere, which behaves as a self-modulating process within the magnetosphere-ionosphere system.

The ionospheric heavy ions originate from a variety of source regions. Two source regions are specified for the outflow for the purpose of exploring their different roles in influencing the magnetospheric dynamics. The dayside cusp-origin heavy ions outflow significantly disturbs the magnetotail by stretching down tail, provides important energized particles to the ring current, and causes inward motion of the dayside magnetopause. In contrast, the nightside aurora-origin heavy ions outflow barely changes the magnetospheric dynamics. Such discrepancy suggests that the geomagnetic feedbacks from the ionospheric heavy ions have certain source origin dependence.

Examinations of the impact of the outflow intensity on the inner magnetosphere and the global configuration indicate that a sufficiently large outflow density and hence large mass loading into the magnetosphere are capable of triggering the Kelvin-Helmholtz instability near the equatorial magnetopause, which not only changes the geometry of the magnetopause boundary but also allows more solar wind energy into the magnetosphere-ionosphere system, raising the cross polar cap potential.

CHAPTER VIII

Future work

The work presented in Chapters III, IV, V, and VI needs some further investigation, as described below.

8.1   A sudden increase in the solar wind velocity

In Chapter IV and V, the sudden increase in the solar wind density changes the solar wind dynamic pressure, leading to a two-phase response in the magnetosphere-ionosphere system. While the solar wind density was statistically found to have little influences on the ionospheric electrodynamics (*Boyle et al.* (1997)), the solar wind velocity has a linear relationship with the cross polar cap potential (CPCP) index, indicating that any changes in the solar wind velocity corresponds to changes in the electric field. Therefore, whether a sudden increase in the solar wind velocity also creates a two-phase response is questionable. Simulations with a solar wind velocity discontinuity are therefore required, in order to understand the controlling parameter in the solar wind dynamic pressure that actually plays the role in producing the two-phase response in the magnetosphere-ionosphere system. Whether a solar wind velocity change also gives rise to a two-phase response or simply increases ionospheric potentials is the key question in the future study.

8.2 Mass transport into the magnetosphere from the solar wind

In Chapter IV, enhancements of the plasma density and thermal pressure inside the magnetosphere and the propagation around the Earth towards the night side under northward IMF conditions indicate that the density in the solar wind enters into the magnetosphere across the dayside magnetopause. Such plasma entry suggests a different scenario from other studies, most of which suggest that the solar wind plasma enters the magnetosphere from the night side where tail reconnection captures plasma in the open magnetic field lines and ejects the plasma towards the Earth. Future work will investigate how and how much the solar wind mass enters to the magnetosphere system from the dayside magnetosphere, contributing to the plasma sheet, and verify the scenario by examining the actual observations from geosynchronous satellites.

8.3 Density dependence of the CPCP index

In Chapter IV, the CPCP index in the end of the simulation time (45 minutes) is slightly larger than the initial value when the solar wind density is smaller. Whether the CPCP index eventually relaxes at a higher value or re-settle down to the initial value is unknown. Therefore, a longer simulation is required, which will verify or challenge the statistical conclusion (*Boyle et al.* (1997)) that the solar wind density is not important to the magnetospheric-ionospheric electrodynamics.

8.4 Effects of the ionospheric outflow velocity

The ionospheric outflow velocity plays an important role in influencing the landing location with respect to the tail reconnection site. For example, a larger outflow velocity from the dayside cusp region will transport into the cusp magnetosphere at

a higher altitude, where the solar wind carries the ionospheric ions to a further tail position. The landing position with respect to the tail reconnection site potentially affects the tail instability, such that an earthward (with respect to the tail reconnection site) landing of the outflow ions may not stretch the tail while a nearby (to the tail reconnection site) landing may disturb the tail significantly, and a tailward (with respect to the tail reconnection site) landing probably again provides little perturbations to the tail stability. Therefore, investigations of the velocity dependence of the magnetotail stability is important and probably shed some lights on the conclusions in Chapter VI, which suggested that there is an outflow-origin dependence of the role of heavy ion on the tail stability. The exploration on the outflow velocity may challenge or further solidify the above conclusion.

8.5 Simulations of the real event

In Chapter V, there is some doubt about the cause of the THEMIS-observed enhancements of electric fields within the dayside magnetosphere around 6:00, June 2, 2007, since WIND spacecraft measured two upstream density increases for this event, while the OMNI2 data reveals a single density increase at the bow shock after propagating the solar wind conditions from those satellites. While it is difficult to determine whether the two enhancements of electric fields are caused by the wave reflections or the two density increases in the solar wind, uncertainties exist when the solar wind conditions propagate from the WIND locations to the bow shock, as indicated by OMNI2 data. To be sure of the cause, further investigations are needed, such as simulations of real events, and analysis of the propagation of the solar wind. More events are also needed in order to clarify the possible cause of the enhancements in the electric field.

BIBLIOGRAPHY

BIBLIOGRAPHY

Akasofu, S. (1964), The development of the auroral substorm, *Planet. Space Sci.*, *12*, 273, doi:10.1016/0032-0633(64)90151-5.

Akasofu, S. (1976), Recent progress in studies of DMSP auroral photographs, *ssr*, *19*, 169–215, doi:10.1007/BF00215692.

Alfvén, H. (1942), Existence of Electromagnetic-Hydrodynamic Waves, *nature*, *150*, 405–406, doi:10.1038/150405d0.

Amm, O. (1996), Comment on "A three-dimensional, iterative mapping procedure for the implementation of an ionosphere-magnetosphere anisotropic Ohm's law boundary condition in global magnetohydrodynamic simulations", *Annales Geophysicae*, *14*, 773.

Andre, M., and A. Yau (1997), Theories and Observations of Ion Energization and Outflow in the High Latitude Magnetosphere, *Space Science Reviews*, *80*, 27–48, doi:10.1023/A:1004921619885.

Andréeová, K., and L. Přech (2007), Propagation of interplanetary shocks into the Earth magnetosphere, *Advances in Space Research*, *40*, 1871–1880, doi:10.1016/j.asr.2007.04.079.

Araki, T. (1994), A Physical Model of the Geomagnetic Sudden Commencement, in *Solar Wind Sources of Magnetospheric Ultra-Low-Frequency Waves*, edited by M. J. Engebretson, K. Takahashi, and M. Scholer, p. 183.

Ashour-Abdalla, M., J. Bosqued, M. El-Alaoui, V. Peroomian, M. Zhou, R. Richard, R. Walker, A. Runov, and V. Angelopoulos (2009), A simulation study of particle energization observed by THEMIS spacecraft during a substorm, *J. Geophys. Res.*, *114*, 9204, doi:10.1029/2009JA014126.

Axford, W. I., and C. O. Hines (1961), A unifying theory of high-latitude geophysical phenomena and gemagnetic storms, *Can. J. Phys.*, *39*, 1433.

Axford, W. I., H. E. Petschek, and G. L. Siscoe (1965), Tail of the Magnetosphere, *J. Geophys. Res.*, *70*, 1231–1236, doi:10.1029/JZ070i005p01231.

Baker, D. N., and R. D. Belian (1986), Impulsive Ion Acceleration in Earth's Outer Magnetosphere, in *Ion Acceleration in the Magnetosphere and Ionosphere*, edited

by T. Chang, M. K. Hudson, J. R. Jasperse, R. G. Johnson, P. M. Kintner, & M. Schulz, p. 375.

Baker, D. N., E. W. Hones, Jr., D. T. Young, and J. Birn (1982), The possible role of ionospheric oxygen in the initiation and development of plasma sheet instabilities, *Geophys. Res. Lett.*, *9*, 1337–1340, doi:10.1029/GL009i012p01337.

Bame, S. J., J. R. Asbridge, W. C. Feldman, E. E. Fenimore, and J. T. Gosling (1979), Solar wind heavy ions from flare-heated coronal plasma, *Solar Phys.*, *62*, 179–201, doi:10.1007/BF00150143.

Birn, J., et al. (2005), Forced magnetic reconnection, *Geophys. Res. Lett.*, *32*, 6105, doi:10.1029/2004GL022058.

Bonnell, J. W., F. S. Mozer, G. T. Delory, A. J. Hull, R. E. Ergun, C. M. Cully, V. Angelopoulos, and P. R. Harvey (2008), The Electric Field Instrument (EFI) for THEMIS, *ssr*, *141*, 303–341, doi:10.1007/s11214-008-9469-2.

Borovsky, J. E., M. Hesse, J. Birn, and M. M. Kuznetsova (2008), What determines the reconnection rate at the dayside magnetosphere?, *J. Geophys. Res.*, *113*, 7210, doi:10.1029/2007JA012645.

Boteler, D. H., R. J. Pirjola, and H. Nevanlinna (1998), The effects of geomagnetic disturbances on electrical systems at the earth's surface, *Advances in Space Research*, *22*, 17–27, doi:10.1016/S0273-1177(97)01096-X.

Boudouridis, A., E. Zesta, R. Lyons, P.-C. Anderson, and D. Lummerzheim (2003), Effect of solar wind pressure pulses on the size and strength of the auroral oval, *J. Geophys. Res.*, *108*.

Boudouridis, A., E. Zesta, L. Lyons, and P. Anderson (2004), Evaluation of the Hill-Siscoe transpolar potential saturation model during a solar wind dynamic pressure pulse, *Geophys. Res. Lett.*, *31*, L23,802, doi:10.1029/2004GL021252.

Boudouridis, A., E. Zesta, L. R. Lyons, P. C. Anderson, and A. J. Ridley (2008), Temporal evolution of the transpolar potential after a sharp enhancement in solar wind dynamic pressure, *Geophys. Res. Lett.*, *35*, 2101, doi:10.1029/2007GL031766.

Bouhram, M., et al. (2005), Survey of energetic O^+ ions near the dayside mid-latitude magnetopause with Cluster, *Annales Geophysicae*, *23*, 1281–1294.

Boyle, C., P. Reiff, and M. Hairston (1997), Empirical polar cap potentials, *J. Geophys. Res.*, *102*, 111.

Brambles, O. J., W. Lotko, P. A. Damiano, B. Zhang, M. Wiltberger, and J. Lyon (2010), Effects of causally driven cusp O^+ outflow on the storm time magnetosphere-ionosphere system using a multifluid global simulation, *J. Geophys. Res.*, *115*, 0, doi:10.1029/2010JA015469.

Carlson, H., and A. Ggeland (1995), The auroral and the auroral ionosphere, in *Introduction to Space Physics*, edited by M. Kivelson and C. Russell, p. 459, Cambridge Press, Cambridge.

Cassak, P. A., and M. A. Shay (2007), Scaling of asymmetric magnetic reconnection: General theory and collisional simulations, *Physics of Plasmas*, *14*(10), 102,114, doi:10.1063/1.2795630.

Chapman, S., and J. Bartels (1940), *Geomagnetism*, Clarendon, Oxford.

Chapman, S., and V. C. A. Ferraro (1930), A New Theory of Magnetic Storms., *nature*, *126*, 129–130, doi:10.1038/126129a0.

Chapman, S., and V. C. A. Ferraro (1931), a New Theory of Magnetic Storms, *J. Geophys. Res.*, *36*, 171–186, doi:10.1029/TE036i003p00171.

Chapman, S., and V. C. A. Ferraro (1932), a New Theory of Magnetic Storms, *J. Geophys. Res.*, *37*, 147–156, doi:10.1029/TE037i002p00147.

Chappell, C. R. (1972), Recent satellite measurements of the morphology and dynamics of the plasmasphere., *Reviews of Geophysics and Space Physics*, *10*, 951–979.

Chi, P. J., et al. (2001), Propagation of the preliminary reverse impulse of sudden commencements to low latitudes, *J. Geophys. Res.*, *106*, 18,857–18,864, doi:10.1029/2001JA900071.

Claudepierre, S. G., M. Wiltberger, S. R. Elkington, W. Lotko, and M. K. Hudson (2009), Magnetospheric cavity modes driven by solar wind dynamic pressure fluctuations, *Geophys. Res. Lett.*, *36*, 13,101, doi:10.1029/2009GL039045.

Cowley, S. (2000), Magnetosphere-ionosphere interactions: A tutorial review, *Geophys. Monogr. Ser.*, *118*, 91–106.

Cowley, S. W. H., and M. Lockwood (1992), Excitation and decay of solar wind-driven flows in the magnetosphere-ionosphere system, *Annales Geophysicae*, *10*, 103–115.

Crooker, N. U. (1979), Dayside merging and cusp geometry, *J. Geophys. Res.*, *84*, 951.

Daglis, I. A., and W. I. Axford (1996), Fast ionospheric response to enhanced activity in geospace: Ion feeding of the inner magnetotail, *J. Geophys. Res.*, *101*, 5047–5066, doi:10.1029/95JA02592.

Daglis, I. A., and E. T. Sarris (1998), Comment on "Experimental investigation of possible geomagnetic feedback from energetic (0.1 to 16 keV) terrestrial O^+ ions in the magnetotail current sheet" by O. W. Lennartsson, D. M. Klumpar, E. G. Shelley and J. M. Quinn, *J. Geophys. Res.*, *103*, 29,545–29,548, doi:10.1029/98JA02268.

Delcourt, D. C. (2002), Particle acceleration by inductive electric fields in the inner magnetosphere, *Journal of Atmospheric and Solar-Terrestrial Physics*, *64*, 551–559, doi:10.1016/S1364-6826(02)00012-3.

Delcourt, D. C., C. R. Chappell, T. E. Moore, and J. H. Waite, Jr. (1989), A three-dimensional numerical model of ionospheric plasma in the magnetosphere, *J. Geophys. Res.*, *94*, 11,893–11,920, doi:10.1029/JA094iA09p11893.

Dessler, A. J. (1968), Magnetic Merging in the Magnetospheric Tail, *J. Geophys. Res.*, *73*, 209, doi:10.1029/JA073i001p00209.

Dessler, A. J., and R. D. Juday (1965), Configuration of auroral radiation in space, *Planet. Space Sci.*, *13*, 63, doi:10.1016/0032-0633(65)90133-9.

Dessler, A. J., and F. C. Michel (1966), Plasma in the Geomagnetic Tail, *J. Geophys. Res.*, *71*, 1421.

Dessler, A. J., and E. N. Parker (1959), Hydromagnetic Theory of Geomagnetic Storms, *J. Geophys. Res.*, *64*, 2239–2252, doi:10.1029/JZ064i012p02239.

DeZeeuw, D. L., T. I. Gombosi, C. P. Groth, K. Powell, and Q. Stout (2000), An adaptive mhd method for global space weather simulations, *IEEEPlasma*, *28*, 1956–1965.

DeZeeuw, D. L., S. Sazykin, R. A. Wolf, T. I. Gombosi, A. J. Ridley, and G. Tóth (2004), Coupling of a global mhd code and an inner magnetospheric model: Initial results, *J. Geophys. Res.*, *109*, doi:10.1029/2003JA010,366.

Dungey, J. W. (1953), The motion of magnetic fields, *Monthly Notices of the Royal Astronomical Society*, *113*, 679–682.

Dungey, J. W. (1961), Interplanetary Magnetic Field and the Auroral Zones, *Physical Review Letters*, *6*, 47–48, doi:10.1103/PhysRevLett.6.47.

Eather, R. H., and S. B. Mende (1971), Airborne observations of auroral precipitation patterns., *J. Geophys. Res.*, *76*, 1746–1755, doi:10.1029/JA076i007p01746.

Ebihara, Y., M. Yamada, S. Watanabe, and M. Ejiri (2006), Fate of outflowing suprathermal oxygen ions that originate in the polar ionosphere, *J. Geophys. Res.*, *111*, 4219, doi:10.1029/2005JA011403.

Elliott, H. A., J. Jahn, C. J. Pollock, T. E. Moore, and J. L. Horwitz (2007), O^+ transport across the polar cap, *Journal of Atmospheric and Solar-Terrestrial Physics*, *69*, 1541–1555, doi:10.1016/j.jastp.2007.06.003.

Engebretson, M. J., et al. (1999), A multipoint determination of the propagation velocity of a sudden commencement across the polar ionosphere, *J. Geophys. Res.*, *104*, 22,433–22,452, doi:10.1029/1999JA900237.

Farrugia, C. J., M. P. Freeman, S. W. H. Cowley, D. J. Southwood, M. Lockwood, and A. Etemadi (1989), Pressure-driven magnetopause motions and attendant response on the ground, *Planet. Spacr Sci.*, *37*, 589–607, doi:10.1016/0032-0633(89)90099-8.

Fok, M., R. A. Wolf, R. W. Spiro, and T. E. Moore (2001), Comprehensive computational model of Earth's ring current, *J. Geophys. Res.*, *106*, 8417–8424, doi:10.1029/2000JA000235.

Fok, M., T. E. Moore, P. C. Brandt, D. C. Delcourt, S. P. Slinker, and J. A. Fedcder (2006), Impulsive enhancements of oxygen ions during substorms, *J. Geophys. Res.*, *111*, 10,222, doi:10.1029/2006JA011839.

Friis-Christensen, E., M. A. McHenry, C. R. Clauer, and S. Vennerstrom (1988), Ionospheric travelling convection voriciies observed near the polar cleft: A triggered response to sudden changes in the solar wind, *Geophys. Res. Lett.*, *15*, 253.

Friis-Christensen, E., S. Vennerstrom, M. A. McHenry, and C. R. Clauer (1988), Ionospheric traveling convection vortices observed near the polar cleft - A triggered response to sudden changes in the solar wind, *Geophys. Res. Lett.*, *15*, 253–256, doi:10.1029/GL015i003p00253.

Fujita, S., T. Tanaka, T. Kikuchi, K. Fujimoto, K. Hosokawa, and M. Itonaga (2003a), A numerical simulation of the geomagnetic sudden commencement: 1. Generation of the field-aligned current associated with the preliminary impulse, *J. Geophys. Res.*, *108*, 1416, doi:10.1029/2002JA009407.

Fujita, S., T. Tanaka, T. Kikuchi, K. Fujimoto, and M. Itonaga (2003b), A numerical simulation of the geomagnetic sudden commencement: 2. Plasma processes in the main impulse, *J. Geophys. Res.*, *108*, 1417, doi:10.1029/2002JA009763.

Fujita, S., T. Tanaka, and T. Motoba (2005), A numerical simulation of the geomagnetic sudden commencement: 3. A sudden commencement in the magnetosphere-ionosphere compound system, *J. Geophys. Res.*, *110*, 11,203, doi:10.1029/2005JA011055.

Gagne, J. (2005), Implementation of ionospheric outow in the lfm global mhd magneto-spheric simulation, m.S. thesis, Dartmouth College.

Ganguli, S. B. (1996), The polar wind, *Reviews of Geophysics*, *34*, 311–348, doi:10.1029/96RG00497.

Garcia, K. S., V. G. Merkin, and W. J. Hughes (2010), Effects of nightside O+ outflow on magnetospheric dynamics: results of multi-fluid MHD modeling, *J. Geophys. Res.*, doi:10.1029/2010JA015730, in press.

Glassmeier, K. (1992), Traveling magnetospheric convection twin-vortices - Observations and theory, *Annales Geophysicae*, *10*, 547–565.

Glassmeier, K. H., and C. Heppner (1992), Traveling magnetospheric convection twin vortices: Another case study, global characteristics, and a model, *J. Geophys. Res.*, *97*, 3977.

Glocer, A., G. Tóth, T. Gombosi, and D. Welling (2009a), Modeling ionospheric outflows and their impact on the magnetosphere, initial results, *J. Geophys. Res.*, *114*, 5216, doi:10.1029/2009JA014053.

Glocer, A., G. Tóth, Y. Ma, T. Gombosi, J. Zhang, and L. M. Kistler (2009b), Multifluid Block-Adaptive-Tree Solar wind Roe-type Upwind Scheme: Magnetospheric composition and dynamics during geomagnetic storms:Initial results, *J. Geophys. Res.*, *114*, 12,203, doi:10.1029/2009JA014418.

Gombosi, T. I. (1998), *Physics of the Space Environment*, Cambridge Press, Cambridge University.

Gonzalez, W.-D. (1990), A unified view of solar wind-magnetosphere coupling function, *Planetary and Space Sciences*, *38*.

Goodman, M. L. (1995), A three-dimensional, iterative mapping procedure for the implementation of an ionosphere-magnetosphere anisotropic Ohm's law boundary condition in global magnetohydrodynamic simulations, *Annales Geophysicae*, *13*, 843–853, doi:10.1007/s005850050223.

Gosling, J. T. (1971), Variations in the Solar Wind Speed along the Earth's Orbit, *Solar Phys.*, *17*, 499–508, doi:10.1007/BF00150051.

Gratton, F. T., L. Bender, C. J. Farrugia, and G. Gnavi (2004), Concerning a problem on the Kelvin-Helmholtz stability of the thin magnetopause, *J. Geophys. Res.*, *109*, 4211, doi:10.1029/2003JA010146.

Haaland, S. E., G. Paschmann, M. Förster, J. M. Quinn, R. B. Torbert, C. E. McIlwain, H. Vaith, P. A. Puhl-Quinn, and C. A. Kletzing (2007), High-latitude plasma convection from Cluster EDI measurements: method and IMF-dependence, *Annales Geophysicae*, *25*, 239–253, doi:10.5194/angeo-25-239-2007.

Harnett, E. M., R. M. Winglee, A. Stickle, and G. Lu (2008), Prompt ionospheric/magnetospheric responses 29 October 2003 Halloween storm: Outflow and energization, *J. Geophys. Res.*, *113*, 6209, doi:10.1029/2007JA012810.

Hasegawa, A. (1975), Plasma instabilities and nonlinear effects, *Springer Verlag Springer Series on Physics Chemistry Space*, *8*.

Hasegawa, H., M. Fujimoto, T. Phan, H. Rème, A. Balogh, M. W. Dunlop, C. Hashimoto, and R. TanDokoro (2004), Transport of solar wind into Earth's magnetosphere through rolled-up Kelvin-Helmholtz vortices, *nature*, *430*, 755–758, doi:10.1038/nature02799.

Hu, Y. Q., Z. Peng, C. Wang, and J. R. Kan (2009), Magnetic merging line and reconnection voltage versus IMF clock angle: Results from global MHD simulations, *J. Geophys. Res.*, *114*, 8220, doi:10.1029/2009JA014118.

Hughes, J. (1995), The magnetopause, magnetotail, and magnetic reconnection, in *Introduction to Space Physics*, edited by M. Kivelson and C. Russell, p. 227, Cambridge Press, Cambridge.

Hundhausen, A. (1995), The Solar Wind, in *Introduction to Space Physics*, edited by M. Kivelson and C. Russell, p. 91, Cambridge Press, Cambridge.

Hundhausen, A. J. (1977), An interplanetary view of coronal holes., in *Coronal Holes and High Speed Wind Streams*, edited by J. B. Zirker, pp. 225–329.

Iijima, T., and T. A. Potemra (1976a), The amplitude distribution of field-aligned currents at northern high latitudes observed by Triad, *J. Geophys. Res.*, *81*, 2165–2174, doi:10.1029/JA081i013p02165.

Iijima, T., and T. A. Potemra (1976b), Field-aligned currents in the dayside cusp observed by Triad, *J. Geophys. Res.*, *81*, 5971–5979, doi:10.1029/JA081i034p05971.

Iijima, T., and T. A. Potemra (1978), Large-scale characteristics of field-aligned currents associated with substorms, *J. Geophys. Res.*, *83*, 599–615, doi:10.1029/JA083iA02p00599.

Iijima, T., L. J. Zanetti, and P. F. Bythrow (1984), Large-scale Birkeland currents in the dayside polar region during strongly northward IMF: A new birkeland current system, *J. Geophys. Res.*, *89*, 7441.

Ilie, R., M. W. Liemohn, and A. Ridley (2010), The effect of smoothed solar wind inputs on global modeling results, *J. Geophys. Res.*, *115*, 1213, doi:10.1029/2009JA014443.

J.M.Ruohoniemi, S. G. Shepherd, and R. A. Greenwald (2002), The response of the high-latitude ionosphere to IMF variations, *J. Atoms. and Terr. Phys.*, *64*, 159,171.

Johnson, C. Y. (1969), Ion and neutral composition of the ionosphere., *Ann. IQSY, Vol. 5, p. 197 - 213*, *5*, 197–213.

Jordanova, V. K., L. M. Kistler, J. U. Kozyra, G. V. Khazanov, and A. F. Nagy (1996), Collisional losses of ring current ions, *J. Geophys. Res.*, *101*, 111–126, doi:10.1029/95JA02000.

Jordanova, V. K., J. U. Kozyra, A. F. Nagy, and G. V. Khazanov (1997), Kinetic model of the ring current-atmosphere interactions, *J. Geophys. Res.*, *102*, 14,279–14,292, doi:10.1029/96JA03699.

Kappenman, J. (2004), The evolving vulnerability of electric power grids, *Space Weather*, *2*, 1004, doi:10.1029/2003SW000028.

Kataoka, R., H. Fukunishi, S. Fujita, T. Tanaka, and M. Itonaga (2004), Transient response of the Earth's magnetosphere to a localized density pulse in the solar wind: Simulation of traveling convection vortices, *J. Geophys. Res.*, *109*, 3204.

Keller, K. A., M. Hesse, M. Kuznetsova, L. Rastätter, T. Moretto, T. I. Gombosi, and D. L. DeZeeuw (2002), Global MHD modeling of the impact of a solar wind pressure change, *J. Geophys. Res.*, *107*, 21–1, doi:10.1029/2001JA000060.

Khan, H., and S. W. H. Cowley (1999), Observations of the repsonse time of high-latitude convection to variations in the interplanetary magnetic field using eiscat and imp-8 data, *Ann. Geopohys*, *17*, 1306–1335.

Kistler, L. M., C. G. Mouikis, B. Klecker, and I. Dandouras (2010), Cusp as a source for oxygen in the plasma sheet during geomagnetic storms, *J. Geophys. Res.*, *115*, 3209, doi:10.1029/2009JA014838.

Kistler, L. M., et al. (2005), Contribution of nonadiabatic ions to the cross-tail current in an O^+ dominated thin current sheet, *J. Geophys. Res.*, *110*, 6213, doi:10.1029/2004JA010653.

Kistler, L. M., et al. (2006), Ion composition and pressure changes in storm time and nonstorm substorms in the vicinity of the near-Earth neutral line, *J. Geophys. Res.*, *111*, 11,222, doi:10.1029/2006JA011939.

Kivelson, M., and C. Russell (1995), Physics of Space Plasma, in *Introduction to Space Physics*, edited by M. Kivelson and C. Russell, p. 27, Cambridge Press, Cambridge.

Kivelson, M. G., and A. J. Ridley (2008), Saturation of the polar cap potential: Inference from Alfvén wing arguments, *J. Geophys. Res.*, *113*, 5214, doi:10.1029/2007JA012302.

Kivelson, M. G., and D. J. Southwood (1985), Resonant ULF waves - A new interpretation, *Geophys. Res. Lett.*, *12*, 49–52, doi:10.1029/GL012i001p00049.

Kivelson, M. G., and D. J. Southwood (1991), Ionospheric traveling vortex generation by solar wind buffeting of the magnetosphere, *J. Geophys. Res.*, *96*, 1661–1667.

Koval, A., J. Šafránková, Z. Němeček, and L. Přech (2006), Propagation of interplanetary shocks through the solar wind and magnetosheath, *Advances in Space Research*, *38*, 552–558, doi:10.1016/j.asr.2006.05.023.

Kozyra, J. U., and M. W. Liemohn (2003), Ring Current Energy Input and Decay, *Space Sci. Rev.*, *109*, 105–131, doi:10.1023/B:SPAC.0000007516.10433.ad.

Lennartsson, O. W., D. M. Klumpar, E. G. Shelley, and J. M. Quinn (1993), Experimental investigation of possible geomagnetic feedback from energetic (0.1 to 16 keV) terrestrial O(+) ions in the magnetotail current sheet, *J. Geophys. Res.*, *98*, 19,443, doi:10.1029/93JA01991.

Lockwood, M., J. H. Waite, Jr., T. E. Moore, C. R. Chappell, and M. O. Chandler (1985), The cleft ion fountain, *J. Geophys. Res.*, *90*, 9736–9748, doi: 10.1029/JA090iA10p09736.

Lockwood, M., A. P. van Eyken, B. J. I. Bromage, D. M. Willis, and S. W. H. Cowley (1986), Eastward propagation of a plasma convection enhancment following a southward turning of the interplanetary magnetic field, *Geophys. Res. Lett.*, *13*, 72.

Lopez, R. E., M. Wiltberger, J. G. Lyon, C. C. Goodrich, and K. Papadopoulos (1999), MHD simulations of the response of high-latitude potential patterns and polar cap boundaries to sudden southward turnings of the interplanetary magnetic field, *Geophys. Res. Lett.*, *26*, 967–970, doi:10.1029/1999GL900113.

Lopez, R. E., M. Wiltberger, S. Hernandez, and J. G. Lyon (2004), Solar wind density control of energy transfer to the magnetosphere, *Geophys. Res. Lett.*, *31*, 8804, doi: 10.1029/2003GL018780.

Lu, G., A. D. Richmond, B. A. Emery, and R. G. Roble (1995), Magnetosphere-ionosphere-thermosphere coupling: Effect of neutral winds on energy transfer and field-aligned current, *J. Geophys. Res.*, *100*, 19,643–19,660, doi:10.1029/95JA00766.

Lu, G., T. E. Holzer, D. Lummerzheim, J. M. Ruohoniemi, P. Stauning, O. Troshichev, P. T. Newell, M. Brittnacher, and G. Parks (2002), Ionospheric response to the interplanetary magnetic field southward turning: Fast onset and slow reconfiguration, *J. Geophys. Res.*, *107*, 10.1029/2001JA000,324.

Luhmann, J. (1995), Ionosphere, in *Introduction to Space Physics*, edited by M. Kivelson and C. Russell, p. 183, Cambridge Press, Cambridge.

Lühr, H., M. Lockwood, P. E. Sandholt, T. L. Hansen, and T. Moretto (1996), Multi-instrument ground-based observations of a travelling convection vortices event, *Ann. Geophysicae*, *14*, 162.

Lukianova, R. (2003), Magnetospheric response to sudden changes in solar wind dynamic pressure inferred from polar cap index, *J. Geophys. Res.*, *108*, 1428, doi: 10.1029/2002JA009790.

Lysak, R. L., and D.-H. Lee (1992), Response of the dipole magnetosphere to pressure pulses, *Geophys. Res. Lett.*, *19*, 937–940.

McPherron, R. L. (1979), Magnetospheric substorms, *Reviews of Geophysics and Space Physics*, *17*, 657–681.

Moldwin, M. B., S. Mayerberger, H. K. Rassoul, M. R. Collier, R. P. Lepping, J. A. Slavin, and A. Szabo (2001), Evidence of different magnetotail responses to small solar wind pressure pulses depending on IMF Bz polarity, *Geophys. Res. Lett.*, *28*, 4163–4166, doi:10.1029/2001GL013045.

Moore, T. E., M. Fok, S. P. Christon, S. Chen, M. O. Chandler, D. C. Delcourt, J. Fedder, S. Slinker, and M. Liemohn (2005), Solar and Ionospheric Plasmas in the Ring Current Region, *Washington DC American Geophysical Union Geophysical Monograph Series*, *159*, 179.

Moore, T. E., M.-C. Fok, D. C. Delcourt, S. P. Slinker, and J. A. Fedder (2010), Global Response to Local Ionospheric Mass Ejection, *J. Geophys. Res.*, in press.

Moretto, T., A. J. Ridley, M. J. Engebretson, and O. Rasmussen (2000), High-latitude ionospheric response to a sudden impulse event during northward IMF conditions, *J. Geophys. Res.*, *105*, 2521–2532, doi:10.1029/1999JA900475.

Moretto, T., M. Hesse, A. Yahnin, A. Ieda, D. Murr, and J. F. Watermann (2002), Magnetospheric signature of an ionospheric traveling convection vortex event, *J. Geophys. Res.*, *107*, 5–1, doi:10.1029/2001JA000049.

Motoba, T., S. Fujita, T. Kikuchi, and T. Tanaka (2007), Solar wind dynamic pressure forced oscillation of the magnetosphere-ionosphere coupling system: A numerical simulation of directly pressure-forced geomagnetic pulsations, *J. Geophys. Res.*, *112*, 11,204, doi:10.1029/2006JA012193.

Murr, D. L., and W. J. Hughes (2001), Reconfiguration timescales of ionospheric convection, *Geophys. Res. Lett.*, *28*, 2145.

Ness, N. F. (1987), Magnetotail research - The early years, in *Magnetotail Physics*, edited by Lui, A. T. Y. & Akasofu, S.-I., pp. 11–16.

Newell, P. T. (2003), Atmospheric physicsA new dawn for aurora, *nature*, *424*, 734–735.

Newell, P. T., C. Meng, and R. E. Huffman (1992), Determining the source region of auroral emissions in the prenoon oval using coordinated Polar BEAR UV-imaging and DMSP particle measurements, *J. Geophys. Res.*, *97*, 12,245, doi: 10.1029/92JA00871.

Newell, P. T., C. Meng, and K. M. Lyons (1996), Suppression of discrete aurorae by sunlight, *nature*, *381*, 766–767, doi:10.1038/381766a0.

Nishitani, N., T. Ogawa, N. Sato, H. Yamagishi, M. Pinnock, J.-P. Villain, G. Sofko, and O. Troshichev (2002), A study of the dusk convection cell's response to an IMF southward turning, *J. Geophys. Res.*, *107*, 1036, doi:10.1029/2001JA900095.

Nosé, M., A. T. Y. Lui, S. Ohtani, B. H. Mauk, R. W. McEntire, D. J. Williams, T. Mukai, and K. Yumoto (2000a), Acceleration of oxygen ions of ionospheric origin in the near-Earth magnetotail during substorms, *J. Geophys. Res.*, *105*, 7669–7678, doi:10.1029/1999JA000318.

Nosé, M., S. Ohtani, A. T. Y. Lui, S. P. Christon, R. W. McEntire, D. J. Williams, T. Mukai, Y. Saito, and K. Yumoto (2000b), Change of energetic ion composition in the plasma sheet during substorms, *J. Geophys. Res.*, *105*, 23,277–23,286, doi: 10.1029/2000JA000129.

Nosé, M., S. Taguchi, K. Hosokawa, S. P. Christon, R. W. McEntire, T. E. Moore, and M. R. Collier (2005), Overwhelming O^+ contribution to the plasma sheet energy density during the October 2003 superstorm: Geotail/EPIC and IMAGE/LENA observations, *J. Geophys. Res.*, *110*, 9, doi:10.1029/2004JA010930.

Nosé, M., A. Ieda, and S. P. Christon (2009a), Geotail observations of plasma sheet ion composition over 16 years: On variations of average plasma ion mass and O^+ triggering substorm model, *J. Geophys. Res.*, *114*, 7223, doi:10.1029/2009JA014203.

Nosé, M., S. Taguchi, S. P. Christon, M. R. Collier, T. E. Moore, C. W. Carlson, and J. P. McFadden (2009b), Response of ions of ionospheric origin to storm time substorms: Coordinated observations over the ionosphere and in the plasma sheet, *J. Geophys. Res.*, *114*, 5207, doi:10.1029/2009JA014048.

Nosé, M., H. Koshiishi, H. Matsumoto, P. C:son Brandt, K. Keika, K. Koga, T. Goka, and T. Obara (2010), Magnetic field dipolarization in the deep inner magnetosphere and its role in development of O^+-rich ring current, *J. Geophys. Res.*, *115*, 0, doi: 10.1029/2010JA015321.

Němeček, Z., and J. Šafránková (2008), IMF control of the high-altitude cusp dynamics, *Advances in Space Research*, *41*, 92–102, doi:10.1016/j.asr.2007.07.038.

Ogino, T. (1986), A three-dimensional MHD simulation of the interaction of the solar wind with the earth's magnetosphere - The generation of field-aligned currents, *J. Geophys. Res.*, *91*, 6791–6806.

Pallocchia, G., A. A. Samsonov, M. B. Bavassano Cattaneo, M. F. Marcucci, H. Rème, C. M. Carr, and J. B. Cao (2010), Interplanetary shock transmitted into the Earth's magnetosheath: Cluster and Double Star observations, *Annales Geophysicae*, *28*, 1141–1156.

Parker, E. N. (1957), Sweet's Mechanism for Merging Magnetic Fields in Conducting Fluids, *J. Geophys. Res.*, *62*, 509–520, doi:10.1029/JZ062i004p00509.

Parker, E. N. (1958), Dynamics of the Interplanetary Gas and Magnetic Fields., *Astrophys. J.*, *128*, 664, doi:10.1086/146579.

Pegoraro, F., M. Faganello, and F. Califano (2008), Collisionless Kelvin-Helmholtz instability and vortex-induced reconnection in the external region of the Earth magnetotail, *Journal of Physics Conference Series*, *133*(1), 012,024, doi:10.1088/1742-6596/133/1/012024.

Peroomian, V., M. El-Alaoui, M. A. Abdalla, and L. M. Zelenyi (2006), Dynamics of ionospheric O^+ ions in the magnetosphere during the 24-25 September 1998 magnetic storm, *J. Geophys. Res.*, *111*, 12,203, doi:10.1029/2006JA011790.

Peterson, W. K., H. L. Collin, O. W. Lennartsson, and A. W. Yau (2006), Quiet time solar illumination effects on the fluxes and characteristic energies of ionospheric outflow, *J. Geophys. Res.*, *111*, 11, doi:10.1029/2005JA011596.

Peterson, W. K., L. Andersson, B. Callahan, S. R. Elkington, R. W. Winglee, J. D. Scudder, and H. L. Collin (2009), Geomagnetic activity dependence of O^+ in transit from the ionosphere, *Journal of Atmospheric and Solar-Terrestrial Physics*, *71*, 1623–1629, doi:10.1016/j.jastp.2008.11.003.

Peymirat, C., A. D. Richmond, B. A. Emery, and R. G. Roble (1998), A magnetosphere-thermosphere-ionosphere electrodynamics general circulation model, *J. Geophys. Res.*, *103*, 17,467.

Peymirat, C., A. D. Richmond, and R. G. Roble (2002), Neutral wind influence on the electrodynamic coupling between the ionosphere and the magnetosphere, *J. Geophys. Res.*, *107*, 10.1029/2001JA900,106.

Pilipp, W. G., and G. Morfill (1978), The formation of the plasma sheet resulting from plasma mantle dynamics, *J. Geophys. Res.*, *83*, 5670–5678, doi: 10.1029/JA083iA12p05670.

Powell, K. G., P. L. Roe, T. J. Linde, T. I. Gombosi, and D. L. D. Zeeuw (1999), A solution-adaptive upwind scheme for ideal magnetohydrodynamics, *J. Comp. Phys.*, *154*, 284.

Richmond, A. D. (1995), *The ionospheric wind dynamo: effects of its coupling with different atmospheric regions,*The Upper Mesosphere and Lower Thermosphere, R.M. Johnson and T.L. Killeen, eds., p. 49, Am. Geophys. Union.

Richmond, A. D., and Y. Kamide (1988), Mapping electrodynamic features of the high-latitude ionosphere from localized observations: Technique, *J. Geophys. Res.*, *93*, 5741.

Ridley, A. (2005), A new formulation for the ionospheric cross polar cap potential including saturation effects, *Ann. Geophys.*, *23*, 3522.

Ridley, A. J. (2000), Estimation of the uncertainty in timing the relationship between magnetospheric and solar wind processes, *J. Atmos. Sol-Terr. Phys.*, *62*, 757.

Ridley, A. J., and E. A. Kihn (2004), Polar cap index comparisons with AMIE cross polar cap potential, electric field, and polar cap area, *Geophys. Res. Lett.*, *31*, doi:10.1029/2003GL019,113.

Ridley, A. J., C. R. Clauer, G. Lu, and V. O. Papitashvili (1998), A statistical study of the ionospheric convection response to changing interplanetary magnetic field conditions using the assimilative mapping of ionospheric electrodynamics technique, *J. Geophys. Res.*, *103*, 4023.

Ridley, A. J., A. D. Richmond, T. I. Gombosi, D. L. D. Zeeuw, and C. R. Clauer (2003), Ionospheric control of the magnetospheric configuration: Thermospheric neutral winds, *J. Geophys. Res.*, *108*, doi: 10.1029/2002JA009,464.

Ridley, A. J., T. I. Gombosi, and D. L. D. Zeeuw (2004), Ionospheric control of the magnetospheric configuration: Conductance, *Ann. Geophys.*, *22*, 567.

Ruohoniemi, J. M., and R. A. Greenwald (1998), The response of high latitude convection to a sudden southward IMF turning, *Geophys. Res. Lett.*, *25*, 2913.

Russell, C. T., and M. Ginskey (1995), Sudden impulses at subauroral latitudes: Response for northward interplanetary magnetic field, *J. Geophys. Res.*, *100*, 23,695.

Russell, C. T., X. W. Zhou, P. J. Chi, H. Kawano, T. E. Moore, W. K. Peterson, J. B. Cladis, and H. J. Singer (1999), Sudden compression of the outer magnetosphere associated with an ionospheric mass ejection, *Geophys. Res. Lett.*, *26*, 2343–2346, doi:10.1029/1999GL900455.

Samsonov, A. A., D. G. Sibeck, and J. Imber (2007), MHD simulation for the interaction of an interplanetary shock with the Earth's magnetosphere, *J. Geophys. Res.*, *112*, 12,220, doi:10.1029/2007JA012627.

Samsonov, A. A., D. G. Sibeck, and Y.-Q. Yu (2010), Transient changes in magnetospheric-ionospheric currents caused by the passage of an interplanetary shock: Northward interplanetary magnetic field case, *J. Geophys. Res.*, *115*, 5207, doi:10.1029/2009JA014751.

Saunders, M. A., M. P. Freeman, D. J. Southwood, S. W. H. Cowley, M. Lockwood, J. C. Samson, C. J. Farrugia, and T. J. Hughes (1992), Dayside ionospheric convection changes in response to long-period interplanetary magnetic field oscillations: Determination of the ionospheric phase velocity, *J. Geophys. Res.*, *97*, 19,373.

Sazykin, S. (2000), Theoretical studies of penetration of magnetospheric electric fields to the ionosphere, ph.D. thesis, Utah State University, Logan, Utah.

Schunk, R. W. (2000), Theoretical developments on the causes of ionospheric outflow, *Journal of Atmospheric and Solar-Terrestrial Physics*, *62*, 399–420, doi: 10.1016/S1364-6826(00)00017-1.

Schunk, R. W., and J. J. Sojka (1997), Global ionosphere-polar wind system during changing magnetic activity, *J. Geophys. Res.*, *102*, 11,625–11,652, doi: 10.1029/97JA00292.

Schunk, R. W., P. M. Banks, and W. J. Raitt (1976), Effects of electric fields and other processes upon the nighttime high-latitude F layer, *J. Geophys. Res.*, *81*, 3271–3282, doi:10.1029/JA081i019p03271.

Sckopke, N. (1966), A General Relation between the Energ of Trapped Particles and the Disturbance Field near the Earth, *J. Geophys. Res.*, *71*, 3125–3130, doi: 10.1029/JZ071i013p03125.

Shay, M. A., and M. Swisdak (2004), Three-Species Collisionless Reconnection: Effect of O^+ on Magnetotail Reconnection, *Physical Review Letters*, *93*(17), 175,001, doi: 10.1103/PhysRevLett.93.175001.

Sheldon, R. B., H. E. Spence, and J. F. Fennell (1998), Observation of the 40 keV field-aligned ion beams, *Geophys. Res. Lett.*, *25*, 1617–1620, doi:10.1029/98GL01054.

Shepherd, S. G., R. A. Greenwald, and J. M. Ruohoniemi (1999), A possible explanation for rapid, large-scale ionospheric responses to southward turnings of the IMF, *Geophys. Res. Lett.*, *26*, 3197.

Sibeck, D. G., R. E. Lopez, and W. Baumjohann (1989), Solar wind dynamic pressure variations and transient magnetospheric signatures, *Geophys. Res. Lett.*, *16*, 13–16, doi:10.1029/GL016i001p00013.

Sibeck, D. G., N. B. Trivedi, E. Zesta, R. B. Decker, H. J. Singer, A. Szabo, H. Tachihara, and J. Watermann (2003), Pressure-pulse interaction with the magnetosphere and ionosphere, *J. Geophys. Res.*, *108*, 1095, doi:10.1029/2002JA009675.

Siscoe, G. L., G. Erickson, B. Sonnerup, N. Maynard, J. Schoendorf, K. Siebert, D. Weimer, W. White, and G. Wilson (2002), Hill model of transpolar potential saturation: Comparisons with MHD simulations, *J. Geophys. Res.*, *107*, 1321, doi:10.1029/2001JA009176.

Slinker, S. P., J. A. Fedder, W. J. Hughes, and J. G. Lyon (1999), Response of the ionosphere to a density pulse in the solar wind: simulation of traveling convection vortices, *Geophys. Res. Lett.*, *26*, 3549–3552, doi:10.1029/1999GL010688.

Slinker, S. P., J. A. Fedder, J. M. Ruohoniemi, and J. G. Lyon (2001), Global MHD simulation of the magnetosphere for November 24, 1996, *J. Geophys. Res.*, *106*, 361–380, doi:10.1029/2000JA000603.

Sonnerup, B., and K. Siebert (2003), Theory of the low-latitude boundary layer and its coupling to the ionosphere: A tutorial review, *Geophysical Monograph*, *133*, 13–32.

Southwood, D. J., and M. G. Kivelson (1990), The magnetohydrodynamic response of the magnetospheric cavity to changes in solar wind pressure, *J. Geophys. Res.*, *95*, 2301–2309.

Stauning, P., and O. A. Troshichev (2008), Polar cap convection and PC index during sudden changes in solar wind dynamic pressure, *J. Geophys. Res.*, *113*, 8227, doi: 10.1029/2007JA012783.

Strangeway, R. J., R. E. Ergun, Y. Su, C. W. Carlson, and R. C. Elphic (2005), Factors controlling ionospheric outflows as observed at intermediate altitudes, *J. Geophys. Res.*, *110*, 3221, doi:10.1029/2004JA010829.

Sweet, P. A. (1958), The Neutral Point Theory of Solar Flares, in *Electromagnetic Phenomena in Cosmical Physics*, *IAU Symposium*, vol. 6, edited by B. Lehnert, p. 123.

Takahashi, K., and R. L. McPherron (1982), Harmonic structure of Pc 3-4 pulsations, *J. Geophys. Res.*, *87*, 1504–1516, doi:10.1029/JA087iA03p01504.

Tamao, T. (1964a), Hydromagnetic interpretation of geomagnetic SSC, *Rep. Ionos. Space Res. Janpan*, *18*, 16–31.

Tamao, T. (1964b), The structure of three-dimensional hydromagnetic waves in a uniform cold plasma, *J. Geomag. Geoelect.*, *18*, 89–114.

Tascione, T. F. (1994), *Introduction to The Space Environment*, Krieger Publishing, 2nd Edition.

Todd, H., S. W. H. Cowley, M. Lockwood, D. M. Willis, and H. Lühr (1988), Response time of the high-latitude dayside ionospheric convection to sudden changes in the north-south component of the IMF, *Planet. Space Sci.*, *36*, 1415.

Toffoletto, F., S. Sazykin, R. Spiro, and R. Wolf (2003), Inner magnetospheric modeling with the Rice Convection Model, *Space Science Reviews*, *107*, 175–196, doi: 10.1023/A:1025532008047.

Tóth, G., et al. (2005), Space Weather Modeling Framework: A new tool for the space science community, *J. Geophys. Res.*, *110*, 12,226, doi:10.1029/2005JA011126.

Tsyganenko, N. A., D. P. Stern, and Z. Kaymaz (1993), Birkeland currents in the plasma sheet, *J. Geophys. Res.*, *98*, 19,455, doi:10.1029/93JA01922.

Tung, Y., C. W. Carlson, J. P. McFadden, D. M. Klumpar, G. K. Parks, W. J. Peria, and K. Liou (2001), Auroral polar cap boundary ion conic outflow observed on FAST, *J. Geophys. Res.*, *106*, 3603–3614, doi:10.1029/2000JA900115.

Vasyliunas, V. M. (1970), Mathematical Models of Magnetospheric Convection and Its Coupling to the Ionosphere, in *Particles and Field in the Magnetosphere*, *Astrophysics and Space Science Library*, vol. 17, edited by B. M. McCormack & A. Renzini, p. 60.

Vasyliunas, V. M. (1979), Interaction between the magnetospheric boundary layers and the ionosphere, in *Magnetospheric Boundary Layers*, *ESA Special Publication*, vol. 148, edited by B. Battrick, J. Mort, G. Haerendel, & J. Ortner, pp. 387–393.

Walén, C. (1947), On the Distribution of the Solar General Magnetic Field and Remarks Concerning the Geomagnetism and the Solar Rotation, *Arkiv for Astronomi*, *33*, 1–63.

Wang, H., A. J. Ridley, and H. Lühr (2008), Validation of the Space Weather Modeling Framework using observations from CHAMP and DMSP, *Space Weather*, *6*, 3001, doi:10.1029/2007SW000355.

Watanabe, M., N. Sato, R. A. Greenwald, M. Pinnock, M. R. Hairston, R. L. Rairden, and D. J. McEwen (2000), The ionospheric response to interplanetary magnetic field variations: Evidence for rapid global change and the role of preconditioning in the magnetosphere, *J. Geophys. Res.*, *105*, 22,955–22,978, doi:10.1029/1999JA000433.

Waters, C. L., K. Takahashi, D. Lee, and B. J. Anderson (2002), Detection of ultralow-frequency cavity modes using spacecraft data, *J. Geophys. Res.*, *107*, 1284, doi:10.1029/2001JA000224.

Weimer, D. R. (1995), Models of high-latitude electric potentials derived with a least error fit of spherical harmonic coefficients, *J. Geophys. Res.*, *100*, 19,595.

Weimer, D. R. (1996), A flexible, IMF dependent model of high-latitude electric potential having "space weather" applications, *Geophys. Res. Lett.*, *23*, 2549.

Weimer, D. R., and J. H. King (2008), Improved calculations of interplanetary magnetic field phase front angles and propagation time delays, *J. Geophys. Res.*, *113*, 1105, doi:10.1029/2007JA012452.

Weimer, D. R., D. M. Ober, N. C. Maynard, W. J. Burke, M. R. Collier, D. J. McComas, N. F. Ness, and C. W. Smith (2002), Variable time delays in the propagation of the interplanetary magnetic field, *J. Geophys. Res.*, *107*, 1210, doi:10.1029/2001JA009102.

Weimer, D. R., D. M. Ober, N. C. Maynard, M. R. Collier, D. J. McComas, N. F. Ness, C. W. Smith, and J. Watermann (2003), Predicting interplanetary magnetic field (IMF) propagation delay times using the minimum variance technique, *J. Geophys. Res.*, *108*, 1026, doi:10.1029/2002JA009405.

Welling, D. T., and A. J. Ridley (2010), Validation of SWMF magnetic field and plasma, *Space Weather*, *8*, 3002, doi:10.1029/2009SW000494.

Whitehead, J. D. (1989), Recent work on mid-latitude and equatorial sporadic-E, *Journal of Atmospheric and Terrestrial Physics*, *51*, 401–424.

Wiltberger, M., W. Lotko, J. G. Lyon, P. Damiano, and V. Merkin (2010), Influence of cusp O^+ outflow on magnetotail dynamics in a multifluid MHD model of the magnetosphere, *J. Geophys. Res.*, *115*, 0, doi:10.1029/2010JA015579.

Winglee, R. M. (2003), Circulation of ionospheric and solar wind particle populations during extended southward interplanetary magnetic field, *J. Geophys. Res.*, *108*, 1385, doi:10.1029/2002JA009819.

Winglee, R. M., D. Chua, M. Brittnacher, G. K. Parks, and G. Lu (2002), Global impact of ionospheric outflows on the dynamics of the magnetosphere and cross-polar cap potential, *J. Geophys. Res.*, *107*, 1237, doi:10.1029/2001JA000214.

Wolf, R. A. (1983), The quasi-static (slow-flow) region of the magnetosphere, in *Solar Terrestrial Physics*, edited by R. L. Carovillano and J. M. Forbes, pp. 303–368, D. Reidel Publishing, Hingham, MA.

Yau, A. W., and M. Andre (1997), Sources of Ion Outflow in the High Latitude Ionosphere, *Space Science Reviews*, *80*, 1–25, doi:10.1023/A:1004947203046.

Yu, Y.-Q., and A. J. Ridley (2008), Validation of the space weather modeling framework using ground-based magnetometers, *Space Weather*, *6*, 5002, doi:10.1029/2007SW000345.

Yu, Y.-Q., and A. J. Ridley (2009), The response of the magnetosphere-ionosphere system to a sudden dynamic pressure enhancement under southward imf conditions, *Annales Geophysicae*, *27*(12), 4391–4407.

Yu, Y.-Q., A. J. Ridley, D. T. Welling, and G. Toth (2010), Including gap-region field-aligned and magnetospheric currents in MHD calculation of ground-based magnetic field perturbations, *J. Geophys. Res.*, *115*, 8207, doi:10.1029/2009JA014869.

Zhang, H., Q.-G. Zong, D. G. Sibeck, T. A. Fritz, J. P. McFadden, K. Glassmeier, and D. Larson (2009), Dynamic motion of the bow shock and the magnetopause observed by THEMIS spacecraft, *J. Geophys. Res.*, *114*, 0, doi:10.1029/2008JA013488.

Zhang, J., et al. (2007), Solar and interplanetary sources of major geomagnetic storms (Dst<= -100 nT) during 1996-2005, *J. Geophys. Res.*, *112*, 10,102, doi:10.1029/2007JA012321.

Zhang, X. Y., et al. (2010), ULF waves excited by negative/positive solar wind dynamic pressure impulses at geosynchronous orbit, *J. Geophys. Res.*, *115*, 10,221, doi:10.1029/2009JA015016.

Zong, Q., H. Zhang, S. Y. Fu, Y. F. Wang, Z. Y. Pu, A. Korth, P. W. Daly, and T. A. Fritz (2008), Ionospheric oxygen ions dominant bursty bulk flows: Cluster and Double Star observations, *J. Geophys. Res.*, *113*, 7, doi:10.1029/2007JA012764.